Ministère de l'Enseignement Supérieur et de la Recherche Scientifique

جامعة أكلي محند أولحاج - البويرة

Université Akli Mohand Oulhadj Bouira

كلية العلـــــوم التطبيقية

Faculté des Sciences Appliquées

Département de Génie électrique

Laboratoire des matériaux et développement durable (LMDD)

THESE DE DOCTORAT

Présentée en vue de l'obtention du grade de Docteur

En : ÉLECTROTECHNIQUE

Spécialité : Énergies renouvelables

Par :

DILMI Ali

Intitulée :

Contribution à la modélisation et au diagnostic des systèmes de production d'énergie électrique à base d'énergies renouvelables

Soutenue publiquement devant le Jury composé de :

BENSAFIA Yacine	Prof	Président	Université de Bouira
BOUZIDA Ahcene	Prof	Rapporteur	Université de Bouira
YASSA Nacera	MCA	Co- encadrant	Université de Bouira
ROUABHI Riyadh	Prof	Examinateur	Université de M'sila
YAHIOU Abdelghani	MCA	Examinateur	Université de Setif 1
MELLAH Hacene	MCA	Examinateur	Université de Bouira

2025/2026

Ministry of Higher Education and Scientific Research

جامعة أكلي محند أولحاج - البويرة

University of Akli Mohand Oulhadj Bouira

كلية العلـــــوم التطبيقية

Applied Science Faculty

Department of Electrical Engineering

Laboratory of Materials, and Sustainable Development Laboratory (LMDD)

DOCTORAL THESIS

Presented to obtain the degree of Doctor

In: Electrotechnics

Specialty: Renewable Energies

By:

DILMI Ali

Entitled:

Contribution to the Modeling and Diagnosis of Electrical Power Generation Systems Based on Renewable Energies

Publicly defended in front of the Jury composed of:

BENSAFIA Yacine	Associate Professor A	President	Bouira University
BOUZIDA Ahcene	Professor	Reporter	Bouira University
YASSA Nacera	Associate Professor A	Co-supervisor	Bouira University
ROUABHI Riyadh	Professor	Examiner	M'sila University
YAHIOU Abdelghani	Associate Professor A	Examiner	Setif 1 University
MELLAH Hacene	Associate Professor A	Examiner	Bouira University

2025/2026

Acknowledgement

First and foremost, I express my deepest gratitude and appreciation to Allah, the Most Gracious, the Most Merciful, who granted me the courage, willpower, patience, and health to continue my academic journey through long and challenging years. Without His grace and mercy, this achievement would never have seen the light.

I would also like to express my deepest gratitude and infinite appreciation to my parents and siblings, who have been the cornerstone of my success. Their unconditional love, continuous encouragement, and endless sacrifices—both emotional and financial—have been the true driving force behind every step of this journey. They stood by me in moments of difficulty, shared my struggles, and never ceased to believe in my abilities. This achievement is as much theirs as it is mine.

I sincerely express my gratitude to all my teachers and professors at the University of Bouira and the University of M'sila, and in particular to my esteemed supervisor, Professor Ahcene Bouzida, for his invaluable guidance, continuous support, and dedication throughout this work. His mentorship was essential in shaping this research, and his influence will remain deeply embedded in my academic journey.

I also extend my sincere thanks to Professors YASSA Nacera, MELLAH Hacene, and BOUDDOU Ryad, who were a strong pillar of support and provided valuable assistance throughout this doctoral project. Their presence was a source of reassurance and strength throughout this journey.

I am also deeply grateful to the members of the examination committee: Professor BENSAFIA Yacine, President of the jury, University of Bouira, for his role as chair of the committee and for his valuable time and academic consideration; Professor ROUABHI Riyadh, University of M'sila, for agreeing to serve as examiner and for his valuable time and academic consideration; and Dr. YAHIOU Abdelghani, University of Sétif 1, for serving as examiner and for his insightful review of this thesis.

My heartfelt appreciation also goes to Dr. Zoubida Chibane for her crucial support and assistance during the most stressful moments of writing this thesis. I would also like to sincerely thank Dr. Belynda Fares for her valuable knowledge and guidance. I further extend my gratitude to Professor Hamlaoui Ameur from the University of M'sila, whose support and encouragement were invaluable throughout this endeavor.

Finally, this page would be incomplete without expressing my profound appreciation to my dearest friends, who stood by me through both joy and hardship. Their smiles, words, and loyal companionship were rays of hope that illuminated my path. Having them in my life has been a blessing beyond measure, and this achievement belongs to them as much as it does to me.

Abstract:

This thesis Addresses diagnostic approaches for wind energy conversion systems (WECSs) under both normal operating conditions and fault scenarios. The main objective is to develop an accurate modeling approach that integrates the mechanical and physical characteristics with the electromagnetic phenomena of the generator, while analyzing its performance during both intact and faulty scenarios. Furthermore, it aims to design effective diagnostic strategies capable of detecting and classifying faults with high accuracy. The study is based on a 4.087 MW Self-Excited Induction Generator (SEIG) and employs the Finite Element Method (FEM) to achieve advanced modeling. In addition, the thesis investigates the application of machine learning and deep learning techniques as modern tools for intelligent fault diagnosis. Overall, this research contributes to the advancement of renewable energy technologies and the enhancement of their efficiency by combining advanced mechanical–physical modeling with state-of-the-art artificial intelligence algorithms.

Keywords: Wind Turbines, Self-Excited Induction Generator (SEIG), Neural Networks (NN), Machine Learning and Deep Learning, Finite Element Method (FEM), Fault Diagnosis, Efficiency Improvement, Artificial Intelligence.

Résumer :

Cette thèse se concentre sur le diagnostic des systèmes de conversion d'énergie éolienne (WECS) dans des conditions de fonctionnement normales ainsi qu'en présence de défauts. L'objectif principal est de développer une approche de modélisation précise qui intègre les caractéristiques mécaniques et physiques avec les phénomènes électromagnétiques du générateur, tout en analysant ses performances dans les états sain et défectueux. De plus, elle vise à concevoir des stratégies de diagnostic efficaces, capables de détecter et de classifier les défauts avec une grande précision. L'étude repose sur l'utilisation d'un générateur asynchrone auto-excité (SEIG) de 4.087 MW et emploie la méthode des éléments finis (FEM) pour réaliser une modélisation avancée. En outre, la thèse explore l'application des stratégies combinant le machine learning et le deep learning comme outils modernes pour le diagnostic intelligent des défauts. Dans l'ensemble, cette recherche contribue à l'avancement des technologies d'énergie renouvelable et à l'amélioration de leur efficacité, en combinant une modélisation mécano-physique avancée avec des algorithmes d'intelligence artificielle de pointe.

Mots-clés : Éoliennes, Générateur Asynchrone Auto-Excité (SEIG), Réseaux de Neurones (NN), Apprentissage Automatique et Apprentissage Profond, Méthode des Éléments Finis (FEM), Diagnostic des Défauts, Amélioration de l'Efficacité, Intelligence Artificielle.

ملخص:

تركّز هذه الأطروحة على تشخيص أنظمة تحويل طاقة الرياح في ظروف التشغيل السليمة وحالات الأعطال. ويتمثل الهدف الرئيسي في تطوير نمذجة دقيقة تدمج الخصائص الميكانيكية والفيزيائية مع الظواهر الكهرومغناطيسية للمولد، مع تحليل أدائه في كلا الحالتين. كما تهدف إلى ابتكار استراتيجيات تشخيص فعّالة للكشف عن الأعطال وتصنيفها بدقة عالية. تعتمد الدراسة على استخدام مولد حثي ذاتي الإثارة بقدرة 4.087 ميغاواط، مع توظيف طريقة العناصر المحدودة لإنجاز النمذجة المتقدمة. بالإضافة إلى ذلك، تستكشف الأطروحة تقنيات التعلم الآلي والتعلم العميق كأدوات حديثة للتشخيص الذكي للأعطال. بشكل عام، تسهم هذه الأطروحة في تطوير تقنيات الطاقة المتجددة وتعزيز كفاءتها من خلال الجمع بين النمذجة الميكانيكية–الفيزيائية المتقدمة وخوارزميات الذكاء الاصطناعي الحديثة.

الكلمات المفتاحية: توربينات الرياح، مولد حثي ذاتي الإثارة، الشبكات العصبية، التعلم الآلي والتعلم العميق، طريقة العناصر المحددة، تشخيص الأعطال، تحسين الكفاءة، الذكاء الاصطناعي.

Table of component

List of figures

List of tables

List of Symbols

I_m : Magnetizing current

V_C : Capacitor voltage

C : Capacitance

w : Angular frequency

$[L_{rr}]$: Rotor inductance matrix.

$[L_{ss}]$: Stator inductance matrix.

$[M_{sr}]$: Mutual inductance matrix between stator and rotor.

Δ_d, Δ_q: Target terms in d-q axis

T_g: Torque of generator.

Ω_{mec}: Rotational speed of the generator shaft [rad/s]

Ω_{mec}: Mechanical rotational speed.

Ω_t: Rotational speed of the turbine rotor (rad/s).

$\vec{C}$, $\vec{A}$: Coefficient vectors

C_p: Power coefficient

F_{dq}, k_{dq}: Adaptation gains

I_L: Current flowing through the inductor

I_{Load}: The load current.

I_{ar} , I_{br} , I_{cr} : Rotor currents of the machine.

I_{as} , I_{bs} , I_{cs}: Stator currents of the machine.

I_{in_opt}: Optimal reference current.

J_g: generator inertia

J_t: wind turbine inertia

K_p, K_i: PI regulator gains

l_s : Stator leakage inductance.

l_s : Rotor leakage inductance.

L_m : Magnetizing inductance

I_{dm} and I_{qm} represent the magnetizing current components along the dq-axes

M: Mutual inductance.

I_m : The global magnetizing current amplitude

I_{Chd}, I_{Chq} : load currents

L_s, L_r: stator and rotor inductance.

$\vec{E}$: The electric field intensity

$\vec{B}$: The magnetic flux density

∇ : Curl operator denoting the rotational derivative of a vector field

∂: partial derivative.

$\vec{H}$: Magnetic field intensity

$\overrightarrow{J_e}$: Conduction current density

$\vec{D}$: Electric flux density

ρ_e: Free electric charge density

ε_0 : Permittivity of free space

ε_r : Relative permittivity

μ : Permeability

μ_0 : Permeability of free space

L_δ : Axial length

Ω_b: Conductive parts consist of the rotor bars

Ω_{core} : Ferromagnetic core

Ω_{air} : Air-gap region

a_{0j}, a_{rj}, b_{rj}, λ_r : The Fourier series expansion coefficients that depend on the coordinates of the air-gap nodes.

mnt : Total number of air-gap nodes

B_r, B_θ : The magnetic components of the flux density

H_{min} : The minimum time step

H_{max} : The maximum time step

C_Δ : Capacitance for delta connection

V_L : Line-to-line voltage

V_{ph} : Phase voltage

PF : Power factor

A : Activity

M : Mobility

C : Complexity

x, x', x'' : Represent the signal

α_i : The learned coefficients of the support vectors

$\mathcal{Y}_i$: The class labels associated with each support vector

X_i : The support vectors themselves

γ: kernel parameter

X : Input feature vector

b: Bias term

mode (.): the function mode

$P(\mathcal{Y})$: Likelihood attributed to class $\mathcal{Y}$ before considering evidence

$P(x_i|\mathcal{Y})$: Chance of obtaining the feature value

$P(X)$: Evidence (normalization factor)

ψ: The Morlet wavelet

$Z(l)$: The output feature map

$W(l)$: The weight matrix of the convolutional filters

$F(l)$: Output of the FC layer

$W_f(l)$; $b_f(l)$: Weights and biases

C_Y : Capacitance for star connection

P_T: Power extracted

P_{aerr}: Aerodynamic power extracted from the wind by the turbine (in watts, W).

P_g: grid active power

Q_g: grid reactive power

R_T: radial length of the turbine blades (meters, m).

R_r: rotor winding resistance.

R_s: stator winding resistance.

S_1, S_2, S_3: Logic switches in the converter.

T_{aerr}: Aerodynamic torque generated by the turbine (in newton-meters, Nm).

T_{em}: Electromagnetic torque

T_m: Mechanical torque

$\hat{V}$: Estimate matrix for V

V_0: Primary value of V

V_{ar} , V_{br} , V_{cr}: Three-phase rotor voltages of the machine.

V_{as} , V_{bs} , V_{cs}: Three-phase stator voltages of the machine.

V_{in}: Input voltage

V_{out}: Output voltage

V_w: Wind velocity (in m/s).

W_0: Primary value of W

f_g: generator friction

f_t: wind turbine friction

i_{ds}, i_{qs}, i_{dr} and i_{qr}: stator and rotor currents in the dq frame.

i_g : Current flowing in the grid-side converter.

i_m: Current flowing through machine-side converter.

P: Number of poles of the generator

V_{DC}: DC-Bus voltage.

v_{ds}, v_{qs}, v_{dr}, v_{qr}: stator and rotor voltages in the dq frame.

v_w: Wind velocity [m/s]

λ_{opt}: Optimal tip speed ratio.

τ_r: Response time

φ_{ar} , φ_{br} , φ_{cr}: Self-inductance fluxes circulating in the rotor of the machine.

φ_{as} , φ_{bs} , φ_{cs}: Self-inductance fluxes circulating in the stator of the machine.

φ_{ds}, φ_{qs}, φ_{dr}, φ_{qr}: stator and rotor flux vectors in the dq frame.

ω_s, ω_r: Stator and rotor angular velocity.

G: gain of the gearbox between the wind turbine and its generator unit.

G: Gearbox gain

J: Total inertia and the wind turbine

$Levy(\lambda)$: a step size sampled from a Lévy distribution

S: Swept area of the turbine blades (in m²).

f: Frequency

t: time

β: Pitch angle, the angle of turbine blades relative to the wind.

λ: Tip speed ratio.

ρ: air density (1.225 kg/m³ at standard conditions).

List of Abbreviations

SEIG: Self-Excited Induction Generator

ANN: artificial neural network

DFIG: doubly fed induction generator

PMSM: permanent magnet synchronous machine

NN: neural networks

ML: machine learning

DL: deep learning

FEM: finite element method

TSFEM: time-stepping finite element method

WECSs: wind energy conversion systems

LCOE: levelized cost of electricity

ESR: Equivalent series resistance

CCGT: combined cycle gas turbines

HAWT**:** Horizontal axis Wind Turbine

BDFIM: brushless doubly-fed induction machine

WTG: wind turbine generator

UMP: Unbalanced magnetic pull

RMS: Root Mean Square

MMF: Magnetomotive force

Emf: Electromotive force

PID: proportional–Integral–Derivative

PLL: phase-Locked Loop

ZCR: Zero-Crossing Rate

STD: Standard Deviation

PTP: Peak-to-Peak

FFT: fast fourier transform

CNN: convolutional neural network

SVM: Support Vector Machine

KNN: k-nearest neighbors

RF: random forest

NB: Naive Bayes

RBF: Radial Basis Function

CWT: Continuous Wavelet Transform

RGB: Red, Green, Blue

FC: Fully connected

THD: Total harmonic distortion

AUC: area under curve

ROC: receiver operating characteristic

HHT: Hilbert–Huang Transform

MPPT: Maximum Power Point Tracking

PI: Proportional-Integral

PMSG: Permanent Magnet Synchronous Generator

PWM: Pulse Width Modulation

RBF: Radial Basis Function

SCIG: squirrel Cage Induction Generator

WT: wind Turbine

WE: wind Energy

WES: Wind Energy System

General Introduction

The transition toward a sustainable energy future has become one of the most critical challenges of the twenty-first century, driven by the urgent need to mitigate climate change, reduce dependence on fossil fuels, and ensure long-term energy security [1]. Among renewable energy sources, wind energy has emerged as one of the most mature and rapidly expanding technologies due to its scalability, wide availability, and continuously decreasing cost [2]. Over the past decade, wind power has consistently ranked among the fastest-growing sources of electricity generation worldwide, supported by continuous advancements in turbine design and power conversion systems, making it a key pillar of modern energy systems [3].

Despite these advantages, the reliability of wind energy conversion systems (WECS) remains a major concern, particularly in isolated and off-grid applications. In this context, the SEIG is widely adopted due to its simple structure, low cost, and ability to operate independently from the grid [4]. However, SEIG-based systems are highly sensitive to electrical and mechanical faults, such as excitation capacitor degradation and broken rotor bars. These faults can significantly deteriorate power quality, reduce system stability, and increase maintenance requirements, especially in remote installations where downtime is costly and difficult to manage. Therefore, the development of accurate and early fault diagnosis techniques is essential to ensure reliable and continuous operation [5].

The literature confirms that SEIGs remain a practical and efficient solution for small-scale and isolated renewable energy systems when compared to alternatives such as permanent magnet synchronous generators (PMSGs) [6]. Numerous studies have investigated their performance under different operating conditions, including stability enhancement, voltage regulation, and power quality improvement [4]. For instance, the authors of [7], proposed series compensation techniques to support SEIG operation at high variable speeds, which led to improved stability, better power quality, and enhanced reliability of these generators. Similarly, Singh [8] focused on employing the Dragonfly algorithm to analyze both transient and steady-state performance of SEIGs, highlighting the role of computational intelligence in modeling rather than direct operational improvement. Other experimental studies have also provided comparative evaluations of SEIGs and PMSGs in small hydropower-based applications, emphasizing the simplicity and economic feasibility of SEIGs in such contexts.

In addition, several studies have investigated parameter identification, voltage regulation, and performance enhancement under different operating conditions, including steady-state, transient, and dynamic regimes [9]. For example, Özer et al. [10] proposed an advanced DSTATCOM control scheme based on an Enhanced Phase-Locked Loop (PLL), which improved terminal voltage regulation and power quality. Meanwhile, Dalei et al. [11] analyzed open-capacitor faults in SEIGs and demonstrated that such faults could reduce torque to zero, causing system instability. They used the Hilbert–Huang Transform (HHT) for fault detection. However, their study did not address capacitor aging and its gradual impact on performance. In contrast, other works, such as those of Derbal and Toubakh [12], focused on gradual degradation by modeling the drift in equivalent series resistance (ESR), yet their linear approach remained oversimplified compared to the true physical complexity of capacitor deterioration.

Traditional modeling approaches, including small-signal models and d–q axis representations, often fail to accurately represent nonlinear behavior under varying operating conditions, such as load changes, rotor speed fluctuations, or capacitor variations.

For instance, Demirtas et al. [13] employed small-signal models for output voltage regulation. However, these models are constrained by linear assumptions around fixed operating points, making them less effective in capturing nonlinear phenomena such as magnetic saturation or fault-related responses. Similarly, Badrudeen et al. [14] relied on linear models for voltage and frequency control under balanced conditions, without addressing fault dynamics or the actual distribution of magnetic flux. While these simplifications reduce computational cost, they risk masking fault signatures and lowering diagnostic accuracy.

These limitations highlight a clear research gap, namely the need for more accurate and physically representative modeling approaches capable of capturing the nonlinear electromagnetic behavior of SEIGs under both healthy and faulty conditions. In this regard, the FEM provides a powerful alternative, as it enables detailed electromagnetic field analysis while accounting for saturation effects and geometrical complexities. When combined with intelligent data-driven techniques, FEM-based models can significantly enhance fault detection capabilities.

Motivated by this gap, this work develops a FEM-based modeling framework for SEIG systems under both normal and faulty operating conditions, with a particular focus on

excitation capacitor degradation and rotor bar faults. The generated data are then analyzed using advanced signal processing techniques and machine learning algorithms, as well as deep learning models based on Continuous Wavelet Transform (CWT) scalogram representations. The results demonstrate that the proposed FEM-driven diagnostic framework achieves high classification accuracy, with ensemble learning methods such as Random Forest providing superior performance, while CNN-based models also show strong capability in feature extraction and fault classification.

Overall, the combination of FEM-based electromagnetic modeling and intelligent diagnostic techniques provides a robust and effective framework for improving the reliability, monitoring, and fault diagnosis of SEIG-based wind energy systems.

This thesis is structured into four main chapters that cover the fundamental aspects of the present study. Chapter I provides a comprehensive overview of WECS, with emphasis on wind turbine designs, technologies, and applications.

Chapter II presents the modeling of the wind energy conversion chain, focusing on SEIG, supported by FEM-based electromagnetic analysis.

Chapter III presents and analyzes simulation results under both healthy and faulty conditions using FFT-based signal processing.

Chapter IV addresses fault diagnosis of excitation capacitors and broken rotor bars using advanced signal processing, machine learning, and deep learning techniques.

I. Chapter 01: Generalities on wind systems and typical induction machine faults

I.1 Introduction

This chapter begins by examining the main components of a typical wind energy conversion system (WECS), including wind turbines (WT), their mechanical structures, and electrical systems. It reviews different turbine types, such as horizontal-axis and vertical-axis designs, and highlights key components like the rotor, nacelle, tower, gearbox, generator, and control systems. The chapter also presents various electromechanical conversion technologies, focusing on induction machines such as Squirrel-Cage, Doubly-Fed, and Brushless Induction Generators, as well as synchronous and permanent-magnet machines. Moreover, it addresses common faults in wind turbine generators, covering mechanical, electrical, and control system failures, with special attention to the faults encountered by SEIGs. The discussion provides an overview of fault mechanisms, detection methods, and strategies to ensure reliable and efficient WECS operation.

I.2 General overview of wind energy

I.2.1 The increasing significance of WECS

WECS has established itself as a fundamental pillar of the global energy transition, demonstrating remarkable expansion over the past decade. As illustrated in Fig (I.1), the cumulative installed capacity increased steadily from 436 GW in 2015 to 840 GW by the end of 2022, and it is expected to reach approximately 2110 GW by 2030 [15]. This consistent growth reflects the increasing global commitment to sustainable power generation and the gradual shift away from fossil-based sources. The expansion of WEs is primarily driven by its environmental advantages such as the reduction of greenhouse gas emissions and its economic benefits, including job creation in turbine manufacturing, installation, and maintenance. Furthermore, advances in turbine design and power electronics have enhanced efficiency and grid integration, consolidating wind power's role as a mainstream component of modern energy systems. Several countries, particularly in Europe, have achieved high penetration levels, demonstrating wind energy's strategic importance in achieving carbon-neutral objectives worldwide.

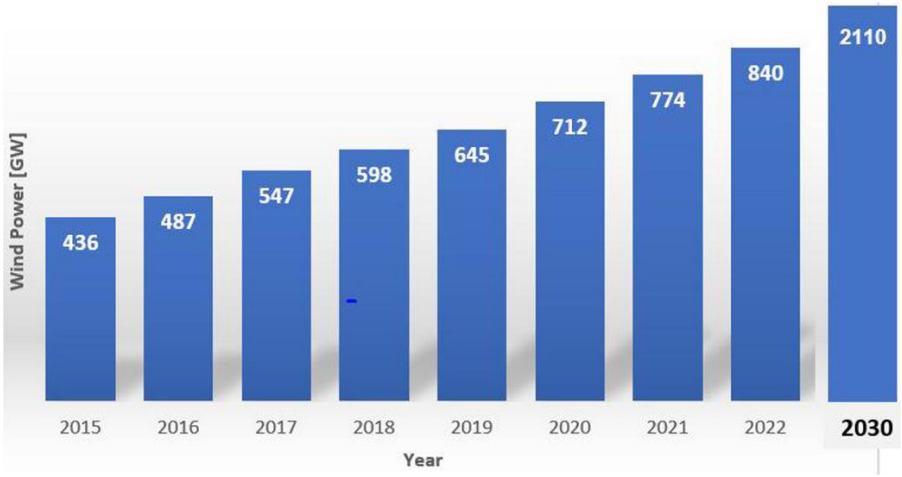

Fig I.1 Projected total generated capacity by 2030 (in GW).

In addition to its rapid capacity growth, the economic competitiveness of wind energy has significantly improved over the past decade [16]. Fig (I.2) illustrates the evolution of the LCOE for different power generation technologies between 2000 and 2030.

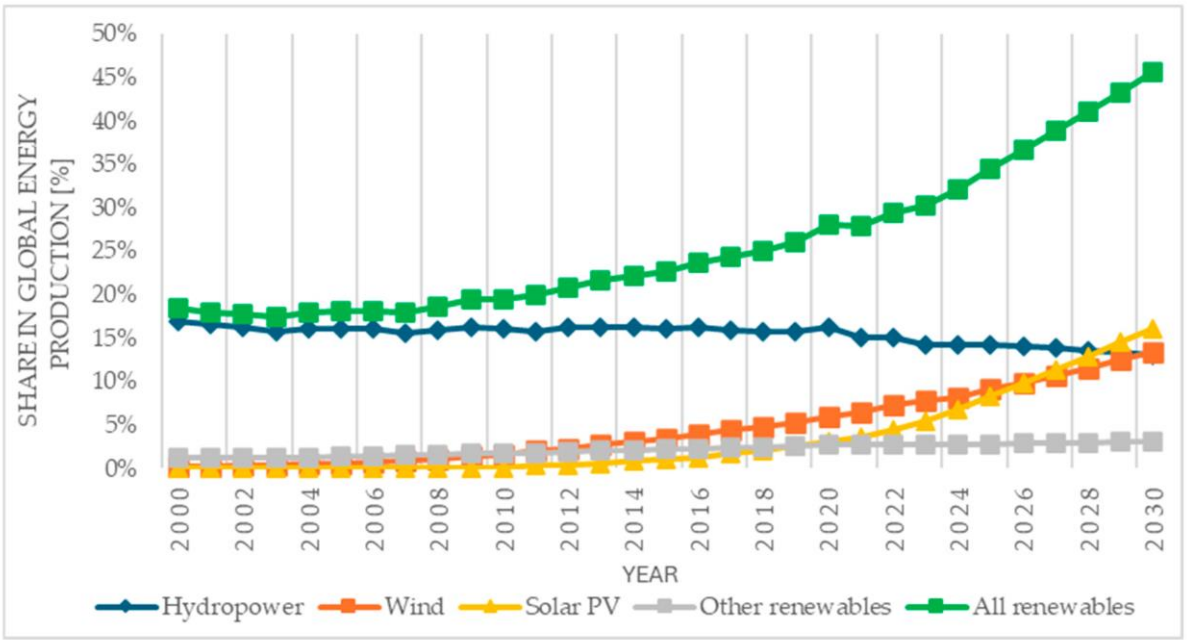

Fig I.2 Cost of wind-generated electricity compared to other energy sources.

During this period, the cost of wind power decreased substantially, positioning it among the most affordable energy sources worldwide. Similarly, solar energy experienced an even steeper decline, mainly due to technological advancements and large-scale deployment. In contrast, the costs of conventional sources such as coal and nuclear remained relatively stable

or even increased slightly. This remarkable reduction in renewable energy costs underscores the growing economic viability of wind and solar power, reinforcing their crucial role in the global shift toward cleaner and more sustainable energy systems [17].

I.2.2 Principles of WECS

WECS involves converting the kinetic energy of moving air into usable electrical power, mainly through a wind turbine. The turbine's blades, designed for aerodynamic efficiency, extract energy from the wind and transform it into rotational mechanical motion. This motion is transferred via the shaft to a generator, where it is converted into electrical energy according to the principle of Electromagnetic induction. The overall performance of this conversion process is influenced by several factors, such as wind velocity, air density, blade design, pitch angle, and the applied control strategy.

Modern WT rely on advanced control techniques such as Maximum Power Point Tracking (MPPT) and pitch regulation to optimize energy extraction under varying wind conditions. Continuous developments in generator technologies have also enhanced efficiency, reliability, and grid integration, particularly with Permanent Magnet Synchronous Generators (PMSGs), Doubly-Fed Induction Generators (DFIGs), and SEIGs the latter being especially suitable for small- and medium-scale applications in isolated areas. Furthermore, the integration of power electronic interfaces including converters and inverters has improved power quality, enabled variable-speed operation, and reduced mechanical stress on turbine components. As a result of these advancements, WE has become one of the most efficient and sustainable sources of renewable electricity in modern power systems [18].

I.3 Wind turbine classification

I.3.1 Classification according to rotor axis

The aerodynamic design of a WT is highly sophisticated, with blade geometry and pitch angle playing a decisive role in its energy capture efficiency [19]. WTs are generally classified into two main configurations: horizontal-axis and vertical-axis designs.

A. WT of the Vertical-Axis Type:

Vertical-axis WTs are among the earliest designs of WECS, with rotors positioned vertically to the ground. Although many prototypes were developed, only a few reached industrial applications. Notable examples include the Savonius rotor, composed of two semi-

cylindrical blades in an S-shape, which operates based on drag forces, achieving a maximum power coefficient of about 0.3 but requiring high starting torque. In contrast, the Darrieus rotor relies on aerodynamic lift and employs two or three symmetric bi-convex blades that may follow cylindrical, conical, or parabolic paths, resulting in variable aerodynamic forces during rotation. An enhanced version is the Helical H-rotor, where the blades are twisted along the vertical axis to reduce pulsating torque, improve self-starting capability, and increase structural stability, making it more suitable for modern applications [20].

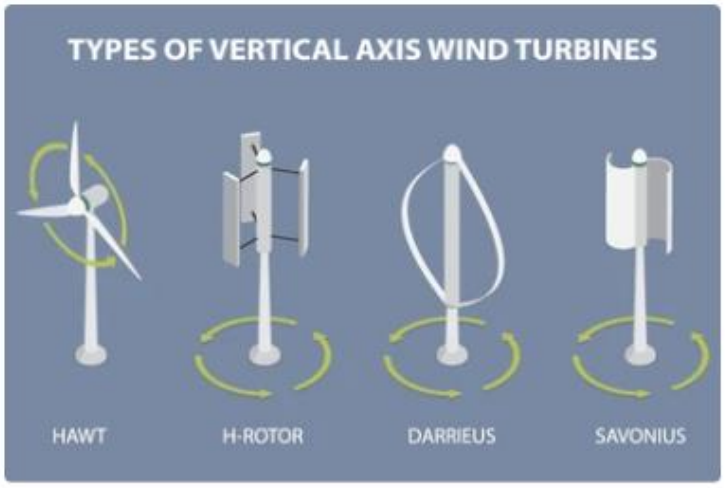

Fig I.3 Vertical axis WT.

B. Horizontal axis WT (HAWT):

HAWTs are the most prevalent WT design, favored for their efficiency in energy conversion. Based on wind orientation, they can operate in upwind or downwind modes (Figure I.4) [21].

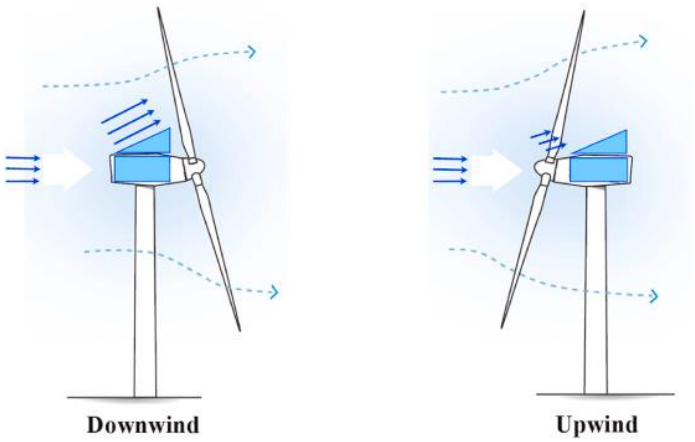

Fig I.4 Horizontal axis WT.

I.3.2 Classification according to size

WTs can be categorized based on their rated capacity and rotor dimensions.

A. Micro WTs:

With outputs below 2.5 kW (rotor diameter < 1.25 m), typically generate 0.4–1.5 kW at 12.5 m/s and are suitable for off-grid applications such as street lighting, water pumping, and rural households in developing regions [22].

B. Small WTs:

producing less than 100 kW, are commonly deployed in residential areas, farms, and remote facilities. They are increasingly integrated into buildings for decentralized power generation; however, challenges such as turbulence, low wind speeds, and noise limit their efficiency in urban and suburban environments [23].

C. Medium-sized WTs (100 kW–1 MW):

Are widely used for grid-connected or stand-alone systems, serving villages, hybrid plants, and wind farms.

D. Large or megawatt-scale WTs:

With capacities up to 10 MW, dominate modern wind farms, particularly offshore installations [24].

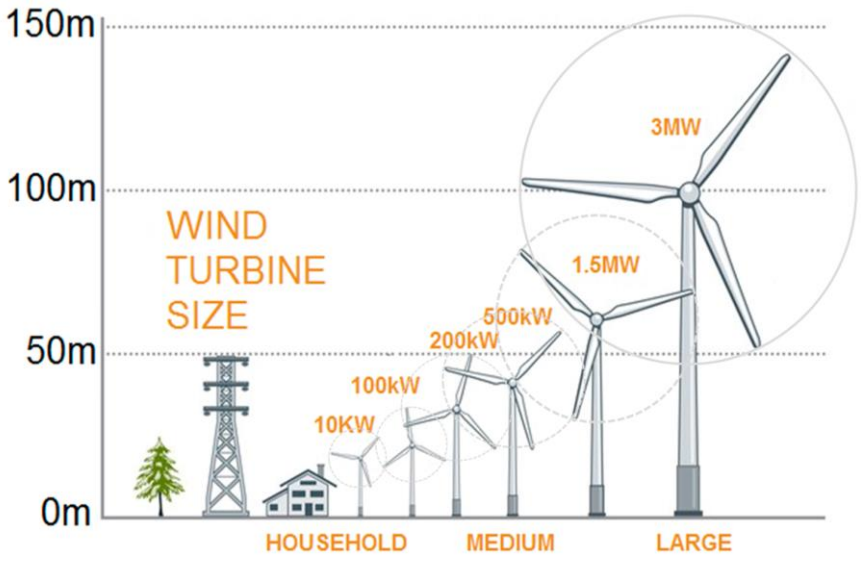

Fig I.5 Various sizes of WTs.

E. Ultra-large WTS (>10 MW)

Remain under development, with ongoing research addressing the technical and economic challenges associated with scaling up, including design, manufacturing, transportation, and installation complexities [25].

I.4 Main Components of HAWT

HAWT integrate several components to transform wind into electricity. A typical WT includes the foundation, tower, blades, nacelle, and generator. Electricity is produced through electromagnetic induction as rotor blades turn, driving the generator. Tower height (50–150 m) is critical since wind speed increases with altitude, enhancing energy capture. The rotor blade pitch angle regulates mechanical power output; by increasing the angle, output decreases, protecting the generator from damage during strong winds [26].

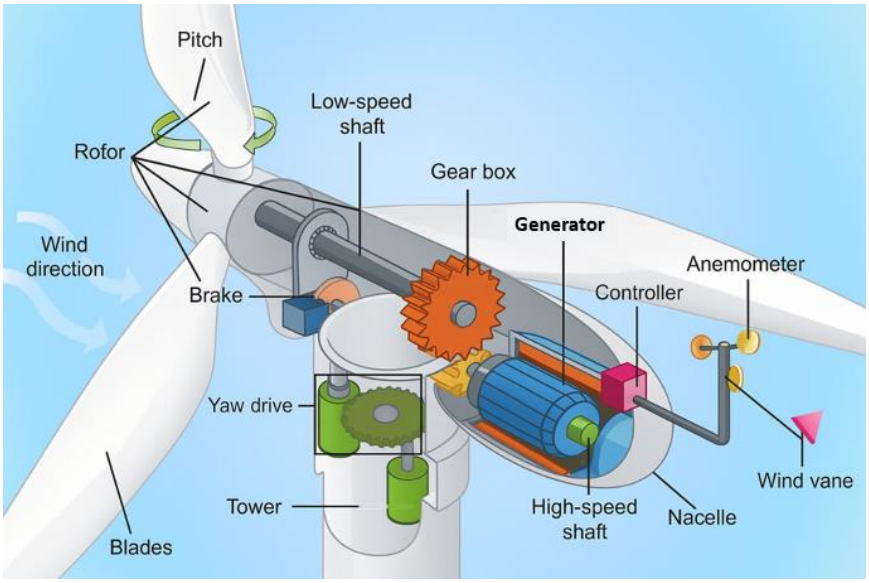

Figure I.6 Main components of a WT.

I.5 Systems based on the induction machine (IM)

I.5.1 Systems Employing Synchronous Machines

Among the different technologies, the IM is the most widely used in WE generation. Its popularity lies in the ability to operate under variable speed conditions while still complying with the essential constraints of voltage and frequency. Several configurations of IM exist,

including the squirrel-cage IM, the double-stator IM, the wound-rotor DFIG, and the brushless DEIG.

I.5.1.1 Squirrel-cage IM

It is the most commonly employed generator in WECS. Its widespread adoption is attributed to key advantages such as reversibility, mechanical robustness, low manufacturing cost due to the absence of sliding contact systems, reduced maintenance requirements, and ease of grid integration. These features have supported its mass production and deployment across a wide power range [27].

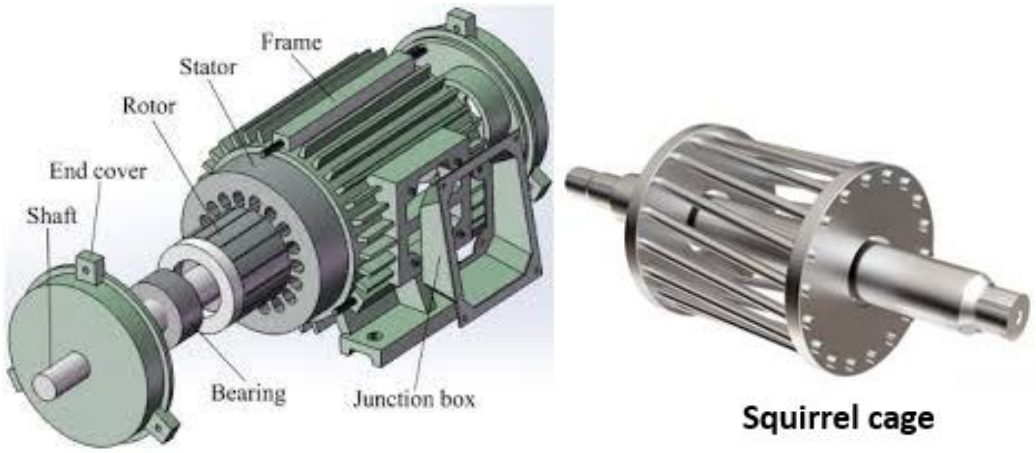

Figure I.7 Main components of an asynchronous generator with a squirrel-cage rotor.

In WTs, squirrel-cage machines are typically built with a fixed number of pole pairs. Consequently, their slip range is limited between 0 and 0.08, which prevents efficient operation under variable-speed conditions. Additionally, since WT rotors generally rotate at low speeds, a mechanical gearbox must be installed between the turbine and the machine to achieve the necessary rotational speed. Another drawback lies in the uncontrolled consumption of reactive power needed to magnetize the rotor, which leads to a reduction in the overall power factor of the grid. To mitigate this issue, capacitor banks are connected in parallel with the stator winding to supply the required reactive power [28].

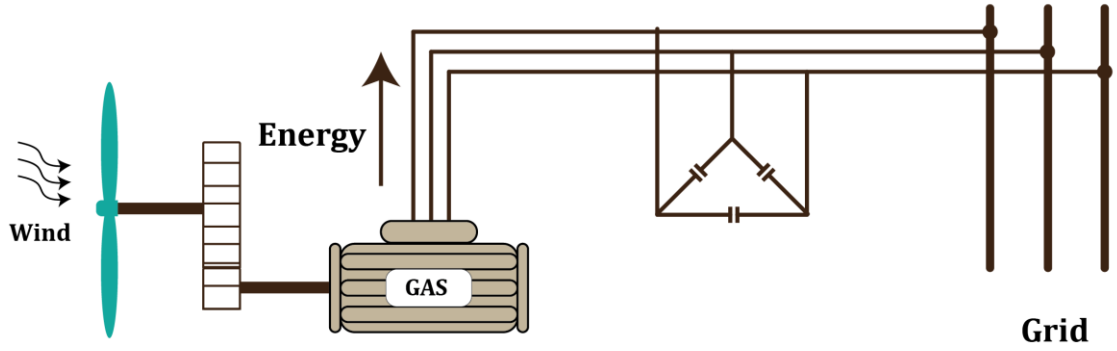

Fig I.8 A semi-variable speed (±10%) WECS using a wound IM.

I.5.1.2 Double-Stator induction machine

A. With DFIG:

The DFIG has become a well-established solution in the field of WE generation, as it exhibits characteristics that make it highly suitable for reliable WECS.

In its most basic arrangement, the stator and rotor of the DFIG are both connected to the electrical grid. The stator is linked through a protection system, while the rotor is interfaced with a static converter, which enables slip control. This configuration allows the machine to operate at variable speeds over a wide range, unlike the squirrel-cage IM. The difference between mechanical and electrical frequencies is compensated by injecting a variable-frequency current into the rotor [29].

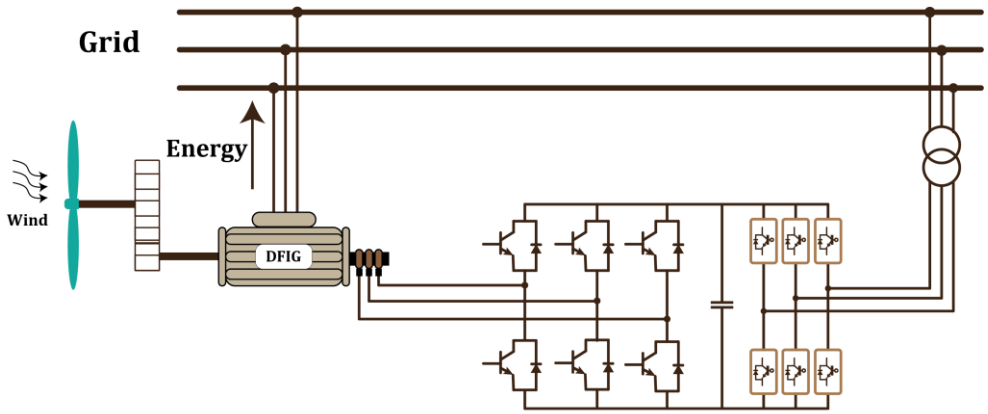

Figure I.9 DFIM with a wound rotor used in a WECS.

A major advantage of this configuration lies in the reduced size of the power converter, since the power exchanged between the rotor and the grid is relatively small compared to the stator power [30].

I.5.1.3 Brushless Doubly-Fed IM (BDFIM)

To overcome the main drawback of the conventional DFIM namely the maintenance requirements of the slip-ring system some manufacturers employ a BDFIM. This configuration maintains the advantage of variable-speed operation and is characterized by the presence of two stator windings with different pole-pair numbers, both accommodated within the same stator core.

The first winding is directly connected to the grid and is designed to handle high power levels, while the second winding, built with smaller conductor sections, is used to regulate the excitation current through a controlled bidirectional converter [31]. The rotor structure differs from that of the classical squirrel-cage machine, yet remains equally robust.

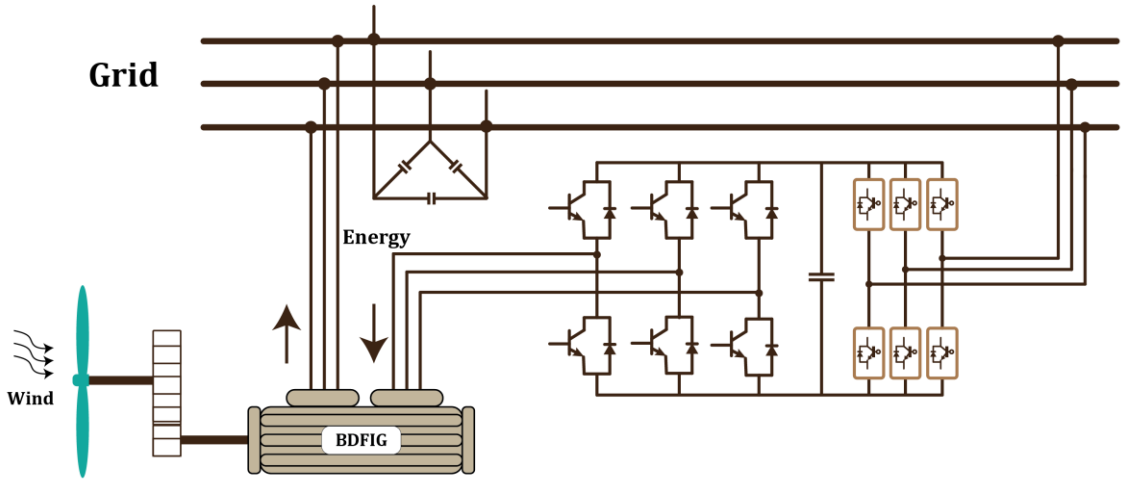

Figure I.10 A brushless DFIG used in a WECS.

I.5.2 Systems Employing Synchronous Machines

Large WT that does not require a gearbox are typically based on synchronous generators. These machines present several advantages, including high efficiency, a favorable torque-to-mass ratio for reasonable dimensions, and the absence of reactive power demand for rotor magnetization, as this is directly provided either by permanent magnets or by a dedicated excitation winding. However, their torque speed characteristic in generating mode requires

strict synchronism between the rotor and stator electromotive forces, which becomes a limitation when applied to wind energy systems characterized by variable wind speeds.

To address this issue, an electronic interface is introduced between the stator and the grid, consisting of a rectifier and an inverter. This interface enables power transfer despite the frequency mismatch between the stator output and the grid, thus allowing the synchronous machine to operate at variable speed and ensuring maximum power extraction. Nevertheless, in such systems the converter must be rated to handle the full generated power, which necessitates high-capacity components and consequently increases the overall cost [32].

I.5.2.1 Wound-Rotor Synchronous Machine

Significant fluctuations in the electromagnetic torque of WES may lead to partial demagnetization of permanent magnets and a reduction in their service life. This drawback is further amplified by the fact that such magnets are often manufactured from rare materials, whose extraction is both costly and technically challenging.

To overcome this limitation, some manufacturers have developed WT based on wound-rotor synchronous machines. In this configuration, the rotating magnetic field in the rotor is generated by a direct current supplied to a field winding (field wheel) through a rectifier connected to the grid. This excitation method requires either a slip-ring assembly on the rotor or a brushless excitation system employing a rotating rectifier [33].

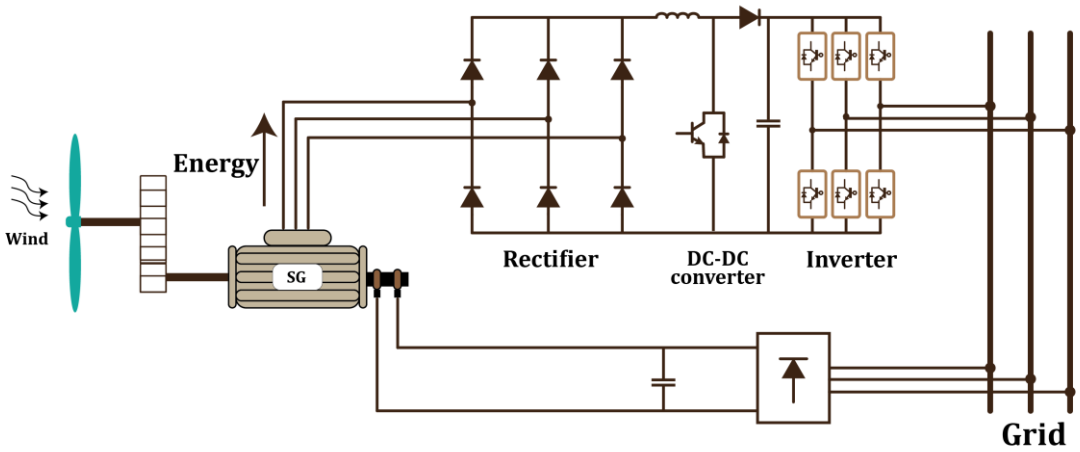

Figure I.11 Wound-rotor synchronous machine used in a WECS.

I.5.2.2 Permanent Magnet Synchronous Machine (PMSM)

Advances in magnetic materials have enabled the development of PMSMs at increasingly competitive costs. These machines employ a multipole permanent magnet rotor, which provides the advantage of a high torque-to-mass ratio.

By eliminating the brush slip ring system and the gearbox typically used in wind turbines, PMSMs significantly reduce maintenance requirements. Furthermore, since the rotor does not require reactive power for magnetization, the machine operates with a high-power factor and excellent efficiency. Several designs of PMSMs are applied in WES, including conventional radial-flux machines, axial-flux disc-type generators, and outer-rotor configurations [34].

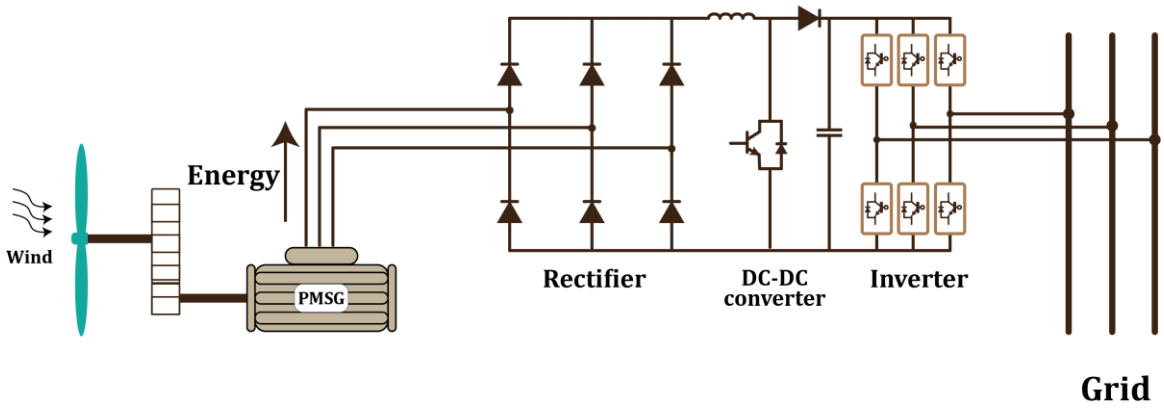

Fig I.12 PMSM used in a WECS.

I.5.3 Systems Employing Special-Structure Machines

Variable reluctance machines, often grouped under the category of special-structure machines, are valued for their robustness and structural simplicity, which result in reduced manufacturing and supply costs. Although their control was once considered complex compared to synchronous and induction machines, modern developments have largely eliminated this drawback, opening new perspectives for their use across a wide range of operating speeds.

Among these machines, the pure variable reluctance type is particularly noted for its simple and low-cost design, consisting of a solid salient rotor and a stator with a basic winding, which together provide high robustness and a favorable torque-to-mass ratio. Instead of generating a rotating field, it operates with a pulsating magnetic field and requires a rectangular

supply current, giving rise to specific power supply needs. These characteristics have led to industrial applications such as starter alternator systems in hybrid vehicles, aerospace systems, and wind turbine generators.

A variant known as the vernier variable reluctance machine differs in that it is supplied with a sinusoidal current. Its operating principle resembles that of a smooth-rotor synchronous machine, and it benefits from compatibility with conventional converters.

To further enhance performance, hybrid versions of variable reluctance machines have been developed by incorporating permanent magnets. Their rotational speed depends on both the pulsation of rotor currents and the number of rotor teeth, similar to the pure type. Thanks to their hybrid configuration and high tooth count, these machines are capable of producing high torque and are widely applicable in industrial systems. The magnets, typically manufactured from rare-earth materials, are specifically chosen to minimize the risk of demagnetization [35].

I.6 Common Defects in WT Generator

Although SEIG and DFIG technologies offer several benefits, wind turbines are still prone to faults because of their intricate electromechanical design and the challenging conditions in which they operate. Fig (I.13) shows the typical faults found in wind turbine generators [36].

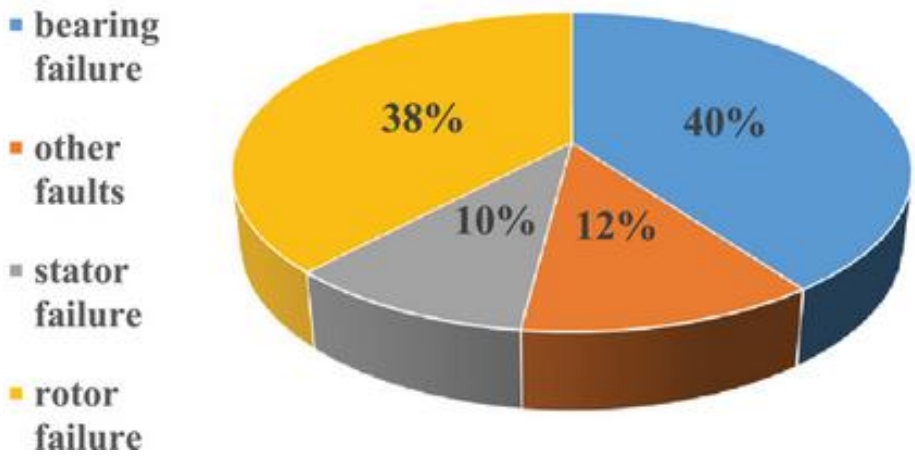

Fig I.13 Typical faults occurring in WT generators.

I.6.1 Electrical failure

Electrical faults can, in some cases, lead to the complete shutdown of the machine, similar to mechanical failures. These faults are generally divided into two distinct categories. For instance, they may occur in the stator electrical circuits or within the rotor electrical circuits.

I.6.1.1 Faults in stator electrical circuits

The most common indicators of stator faults in generators include excessive heating of the stator windings. Stator winding faults are generally classified into four categories: inter-phase short circuits, turn-to-turn short circuits, single-phase-to-ground faults, and three-phase-to-ground faults. Such failures often originate from short circuits caused by imperfections in the mechanical laminations or errors during the installation process. Insulation degradation, on the other hand, is mainly linked to factors such as aging, contamination, cracks, and corrosion. Fig (I.14) illustrates the schematic representation of a turn-to-turn short circuit occurring in one phase of the stator [37].

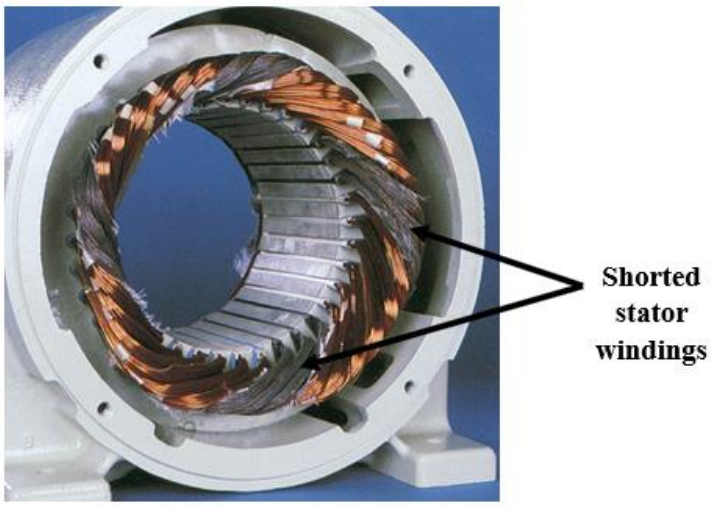

Fig I.14 Shorted stator windings.

I.6.1.2 Rotor failure

It's can generally be classified into winding-related faults and structural faults. Rotor winding failures are often associated with insulation degradation, which may lead to single- or double-point grounding, inter-turn short circuits, or even a reduction or complete loss of excitation current. Among these, inter-turn short circuits are the most common and constitute a major form of electrical faults in rotor windings. Their occurrence is strongly influenced by

harsh operating conditions, such as intense magnetic fields, high mechanical stresses, and strong electric fields. While a limited number of short-circuited turns may have only a minor impact on machine performance, a larger number can result in severe overheating, damage to the journal and bearing bush, or grounding faults that compromise generator operation and may cause significant economic losses [38].

Rotor body faults vary depending on the machine structure. In synchronous generators, they mainly result from eddy current losses caused by negative-sequence voltages, leading to local overheating and fatigue cracks. In squirrel-cage induction machines, faults often originate from partial or complete breakage of rotor bars or end rings typically made of aluminum or copper due to excessive loading, vibration, or thermal stress. These breakages commonly occur at the welded joints between bars and end rings, which represent mechanical weak points. The fragility of these joints thus constitutes a major vulnerability in squirrel-cage rotors.

Fig I.15 Broken rotor bars.

I.6.2 Mechanical failure

Mechanical faults occur when parts of the mechanical structure are damaged or malfunction, preventing the system from functioning properly and sometimes causing total failure. In WT generator systems, these faults often involve the rotor body, supporting structure, generator frame, or connecting parts, and usually appear as structural failures. Bearings, which

link the rotor and stator, are especially prone to damage. Misalignment of bearings with the stator's axis or excessive wear due to prolonged use can create unwanted excitation forces, resulting in abnormal friction between moving and stationary components.

I.6.2.1 Air gap eccentric

Is a common fault in electrical machines that occurs when the clearance between the stator and rotor deviates from its nominal value. This deviation distorts the magnetic field distribution, producing uneven radial forces and an unbalanced magnetic pull (UMP), a primary cause of abnormal vibration. It also leads to non-uniform rotor currents, stator current imbalance, and torque fluctuations. With greater severity, these effects may result in rotor–stator contact, bearing wear, or insulation failure.

Eccentricity usually stems from rotor geometry imperfections or operational stresses and appears in three main forms: static, dynamic, and mixed. Static eccentricity involves misalignment between the rotor and stator axes, while dynamic eccentricity refers to displacement of the rotor's rotation axis. Studies indicate that over 50% of machine faults are related to uneven air-gap distribution, highlighting its critical impact on machine reliability [39]. Figure (I.16) illustrates air-gap eccentricity in both healthy and faulty conditions [40].

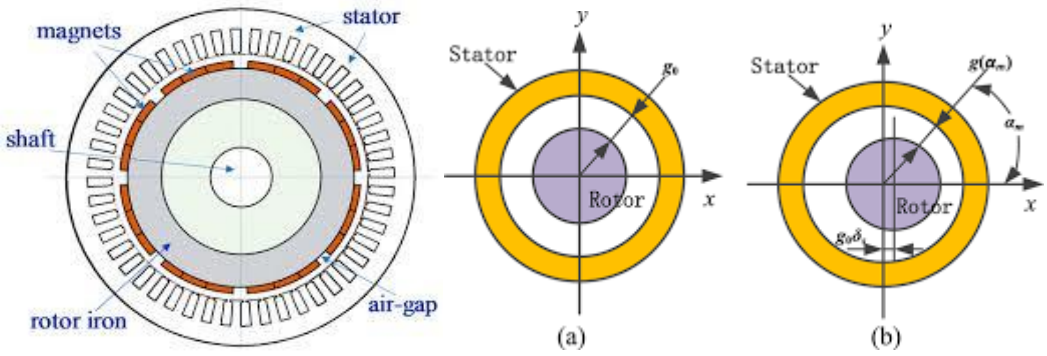

Fig I.16 air-gap eccentricity under healthy and faulty conditions.

I.6.2.2 Bearing Faults

Ball bearings are essential components that ensure the dependable and efficient operation of electrical machines, and their deterioration is among the most frequent mechanical faults. Such failures may originate from inappropriate material selection during manufacturing, surface defects such as cracks, pitting, or spalling on the rolling elements, or from poor lubrication. In fact, the grease that ensures smooth rotation may harden over time, leading to increased friction and resistance. Additionally, circulating currents in the bearings of

asynchronous machines, especially at high rotational speeds, can accelerate wear and degradation. These issues may result in abnormal vibrations and disturbances within the machine. To identify such faults, vibration-based analysis or harmonic monitoring of stator currents is commonly employed [41].

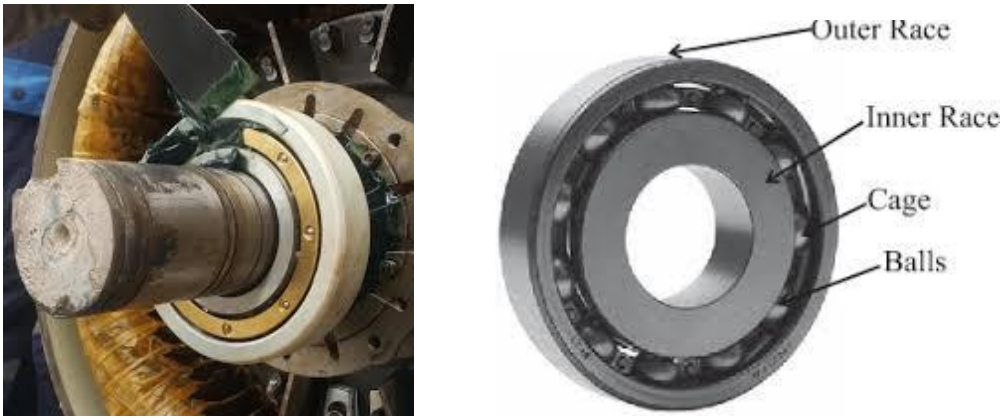

Fig I.17 Bearing components.

I.6.3 Other Faults in WECS

In addition to the major faults previously discussed, WECS may also encounter several other mechanical, electrical, and control-related failures that affect their reliability and performance. Mechanical issues include bearing corrosion, plastic deformation, gluing, cage damage, misaligned end-shields, and shaft cracks or fractures, often triggered by poor lubrication, excessive loading, or unsuitable materials. Electrical faults commonly arise in transformers, where insulation degradation, thermal stress, or mechanical deformation can lead to severe failures, and in cables, which are vulnerable to insulation breakdown, partial discharges, and accelerated aging under harsh environmental conditions. On the control side, malfunctions in pitch and yaw systems, sensor inaccuracies, or PI/PID controller faults may compromise stability, reduce energy capture, and even lead to unsafe operating conditions. Altogether, these additional faults emphasize the necessity of effective diagnostic and monitoring strategies to maintain efficient and secure operation of wind turbine systems [42].

I.6.4 Common failures in SEIGs

In addition to the previously mentioned faults, the SEIG is subject to specific types of failures resulting from its operating principle and its reliance on excitation capacitors for voltage generation. Among these, capacitor-related faults are of particular importance, such as

capacitor disconnecting, as illustrated in Fig (I.18). Capacitors may also deteriorate over time due to aging caused by prolonged operation, repeated electrical stresses, or manufacturing defects, which ultimately lead to a decrease in their effectiveness. Any malfunction in the capacitors directly affects the voltage stability and the generator's ability to maintain self-excitation [43].

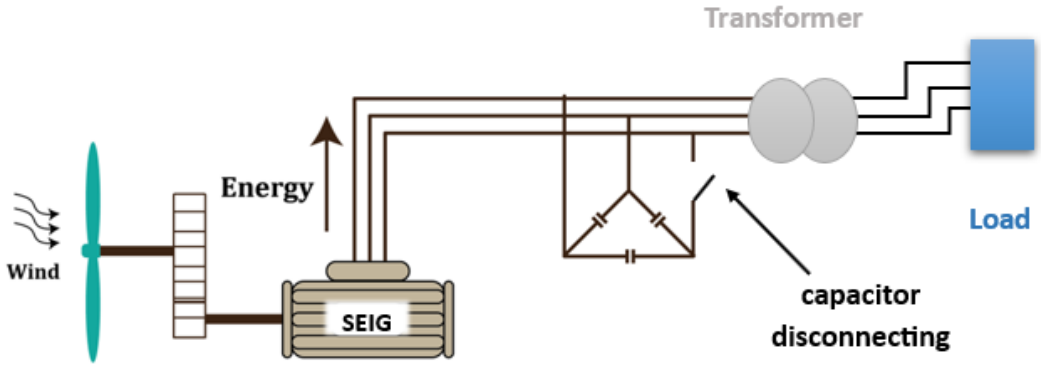

Fig I.18 Disconnection of excitation capacitor fault in SEIG.

Moreover, the SEIG may experience phase-open faults or phase-to-ground faults, in addition to other types of faults illustrated in Fig (I.19) [44]. These faults are considered critical because they cause disturbances in current flow and imbalance in the electrical circuit, which may result in mechanical vibrations and increased power losses. Furthermore, the SEIG is highly sensitive to load unbalance, which can lead to waveform distortion and increased copper and core losses, thereby negatively affecting the operating efficiency and lifespan of the generator [44].

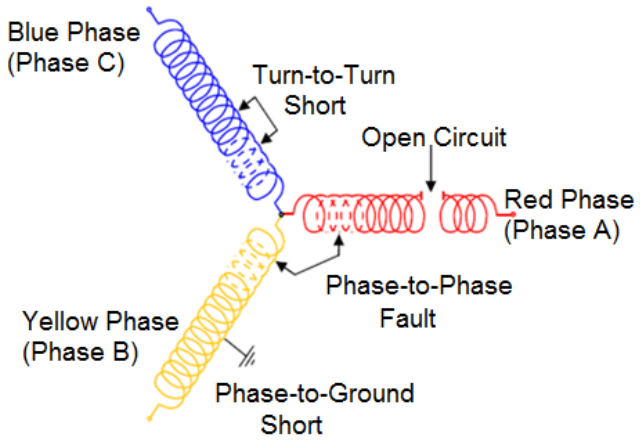

Fig I.19 Common types of stator winding faults.

I.7 conclusion

This chapter presents a detailed overview of WICSs, highlighting their main components, as well as reviewing the different types of WTs and the generators typically employed in these systems. In addition, it emphasizes the growing importance of fault diagnosis by presenting the most common failures that generators may encounter, whether mechanical or electrical, which underscores the urgent need for reliable techniques to detect and accurately diagnose such faults. The diversity and complexity of these failures call for the development of intelligent diagnostic approaches that can adapt to a wide range of applications, from small-scale systems to large offshore installations, thereby contributing to improved energy capture efficiency and enhanced overall system performance.

The subsequent chapter will focus on modeling the wind system, which represents a fundamental stage prior to implementing fault diagnosis strategies within the system.

II. Chapter 02: Dynamic modeling of WECS

II.1 Introduction

Understanding how the kinetic energy of moving air is converted into electricity forms the foundation for analyzing WECS. Modeling the WECS is therefore a crucial step toward enhancing their performance and efficiency. In this context, the SEIG stands out as an effective solution due to its ability to operate independently from the grid using excitation capacitors.

This chapter begins by explaining the operating principle of the SEIG, highlighting the physical mechanisms responsible for voltage self-excitation. It then presents the aerodynamic model of the wind turbine, illustrating how wind kinetic energy is transformed into mechanical torque. Subsequently, the chapter introduces a control strategy to regulate the output voltage and ensure stable operation of the SEIG under varying wind speed conditions. Finally, to achieve a more accurate representation of the electromagnetic phenomena, a detailed model based on the FEM is constructed Operating Principle of the SEIG

II.2 Operating Principle of the SEIG

SEIG is one of the most widely used types of generators in standalone power generation systems, thanks to its ability to operate without the need for an external reactive power source. Its operating principle relies on a simple yet fundamental concept the conversion of mechanical energy into electrical energy through electromagnetic induction. This process represents the core mechanism behind the generator's self-excitation and voltage buildup.

For an IM to function as a generator, the rotor must rotate in the same direction as the rotating magnetic field but at a speed slightly greater than the synchronous one. This condition enables the rotor to establish its own magnetic field and induce an electromotive force in the stator windings. When the machine is connected to the electrical system, it normally operates at a speed slightly below the synchronous speed, which corresponds to motor operation. At the exact synchronous speed, no relative motion exists between the rotor conductors and the magnetic field, resulting in the absence of electromagnetic induction and, consequently, no energy exchange with the stator. When the rotor speed exceeds the synchronous value, an induced current appears in the rotor, generating an EMF similar to that of a synchronous generator. The speed difference between the rotor and the magnetic field, known as slip, usually

remains within a few percent. Within this small range, an increase in rotor speed leads to a proportional rise in electromagnetic torque and, therefore, in the output power. Fig (II.1) depicts the various operating modes of the induction machine [45].

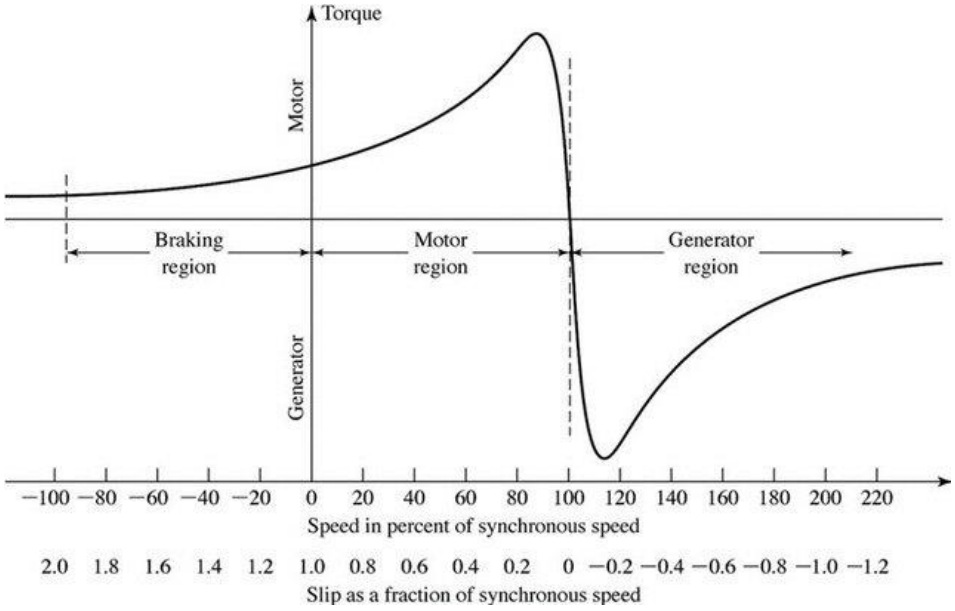

Fig II.1. Operating range of the asynchronous machine.

The capacitor bank provides the excitation current, while the generator progressively recharges it, resulting in a gradual voltage build-up until the system reaches equilibrium within the magnetic saturation region. Fig (II.2) illustrates this phenomenon by showing the evolution of the stator electromotive force along with the external characteristic of the capacitor V_C as a function of the magnetizing current ($V_C = \frac{I_m}{Cw}$) under no-load conditions. The interaction between these two curves defines the self-excitation process and drives the system toward its steady-state operating point [46].

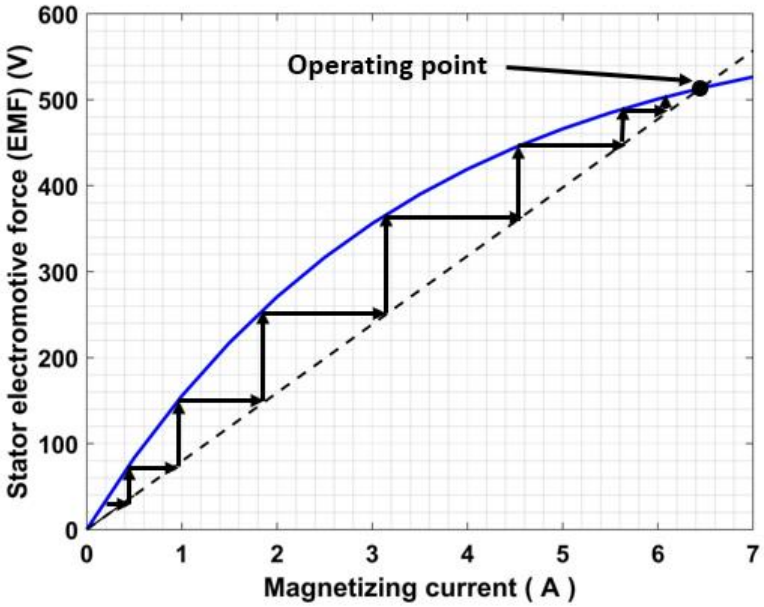

Fig II.2. self-excitation phenomenon of the generator.

A closer examination of these characteristics reveals that the position of the operating point on the magnetization curve is primarily influenced by two factors: the capacitance of the excitation bank, which determines the slope of the capacitor load line, and the applied load, which modifies the slip.

Once the operating point is established, the generator produces a nearly constant RMS stator voltage. However, if the magnetizing inductance were assumed constant and equal to its unsaturated value, the magnetization curve would lack the characteristic saturation knee and would not intersect the capacitor's external characteristic. In such a case, self-excitation would remain theoretically possible, but the stator voltage would rise indefinitely, making stable operation impossible [47].

Fig (II.3) illustrates a schematic representation of the system under study, providing a clearer view of the SEIG's operating structure and its internal energy conversion process.

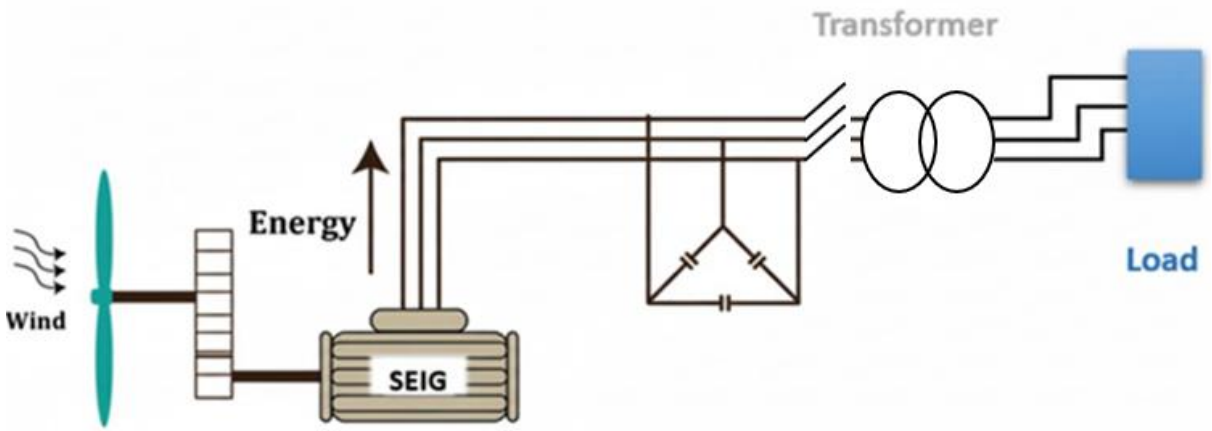

Fig II.3. Schematic Diagram of the proposed system

II.3 WT modeling

The wind acts on the turbine blades through the kinetic energy extracted from the moving air, causing them to rotate. This rotation converts WE into mechanical power that drives the generator rotor. The aerodynamic power $Paer$ and the corresponding aerodynamic torque $Taer$ are given by the following mathematical relations [48]:

$$P_{aer} = \frac{1}{2} C_p(\lambda, \beta) \rho S v_w^3 \quad \text{(II.1)}$$

$$T_{aer} = \frac{P_{aer}}{\Omega_t} = \left(\frac{1}{2} C_p(\lambda, \beta) \rho S v_w^3\right) \frac{1}{\Omega_t} \quad \text{(II.2)}$$

Where:

v_w: denotes the wind velocity.

ρ : refers to the air density, is 1.225 kg/m³ at sea level.

S : is the swept area of the turbine blades, $S = \pi R^2$.

Ω_t: represents the angular speed of the turbine rotor.

The tip-speed ratio λ is an essential parameter that characterizes the rotational behavior of a wind turbine. When λ exceeds 3, the turbine is classified as a high-speed type, typically having fewer blades and operating at higher rotational speeds. Conversely, when λ is below 3, the turbine is considered a low-speed type, usually featuring more blades and rotating more slowly. The tip-speed ratio can be expressed as follows [49]:

$$\lambda = \frac{\Omega_t R}{v_w} \tag{II.3}$$

R: denotes the radius of the area swept by the rotating blades.

The power coefficient $C_p(\lambda, \beta)$ represents the ability of the wind turbine to convert the kinetic energy of the wind into mechanical energy. This coefficient is influenced by several factors, including the number of rotor blades, their aerodynamic shape, and the variation of blade profiles along their length. It also depends on the desired rated power, the applied control strategy (pitch or stall regulation), and whether the WT operates at a fixed or variable speed.

The $C_p(\lambda, \beta)$ characteristic can be determined experimentally through wind tunnel testing. It is described as a nonlinear function of the tip-speed ratio λ and the blade pitch angle β [50]. The theoretical upper limit of the power coefficient, known as the Betz limit, is given by $C_{p\,max} = 16/27 \approx 0.5926$.

The gearbox connects the turbine to the generator, serving to match the turbine's low rotational speed with the generator's higher required speed. This synchronization enables efficient energy conversion between the two components and ensures optimal system performance. The relationship between the turbine's and the generator's rotational speeds is given as [51]:

$$\Omega_t = \frac{\Omega_{mec}}{G} \tag{II.4}$$

And the corresponding torque is given by:

$$T_g = \frac{T_{aer}}{G} \tag{II.5}$$

Where, G is the gearbox ratio between the WT and the generator, T_g is the generator torque, and Ω_{mec} refers to the mechanical angular velocity.

The fundamental dynamic equation describing the relationship between torque and speed is formulated as follows [49]:

$$J\frac{d\Omega_{mec}}{dt} + f\Omega_{mec} = T_g - T_{em} \tag{II.6}$$

$$J = \frac{J_t}{G^2} + J_g \tag{II.7}$$

$$f = \frac{f_t}{G^2} + f_g \tag{II.8}$$

Where:

J, J_t and J_g denote the total inertia, the WT inertia, and the generator inertia, respectively.

f, f_t and f_g represent the total friction, the WT friction, and the generator friction, respectively.

Fig (II.4) illustrates the schematic representation comprising the WT block, the gearbox block, and the generator shaft block [51].

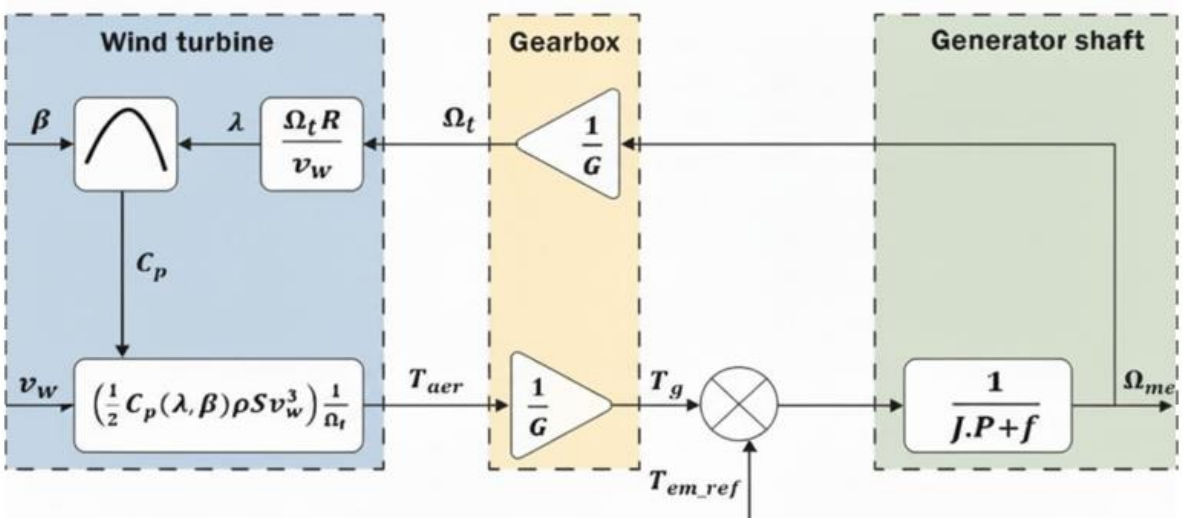

Fig II.4. The WT schematic.

II.3.1 Control Approaches for the WT

Within WICSs, achieving efficient and reliable power control is vital not only to maximize energy extraction but also to prevent the generator from exceeding its mechanical speed limits. This session introduces a classical power control strategy applied to a WT coupled with a SEIGa configuration favored for its low cost and ability to function efficiently across a wide range of wind speeds.

Two main control strategies are applied to the wind turbine:

- The first aims to maximize the extracted power when the wind speed is below the level corresponding to the rated power of the turbine.
- The second seeks to limit the generated power to the rated value when the wind speed becomes higher than the nominal threshold.

In WE generation, the performance of a turbine is commonly represented by a power wind speed characteristic curve, which defines its operating behavior under varying wind

conditions. This curve is divided into four distinct operational zones, each governed by specific control objectives, as illustrated in Figure (II.5) [52].

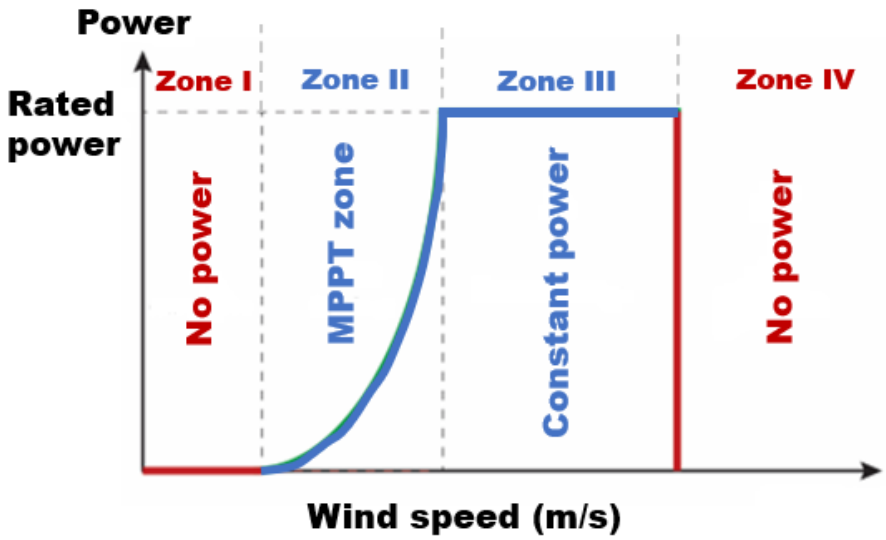

Fig II.5. Different operating zones in variable-speed WT.

At very low wind velocities, corresponding to Zone I, the turbine remains non-operational because the wind speed is below the cut-in threshold. In this state, the available WE is insufficient to initiate rotor motion, and consequently, no electrical power is produced [53].

When the wind velocity surpasses the cut-in value, the turbine transitions into Zone II, also known as the MPPT region. Within this range, the turbine speed varies dynamically to extract the highest possible power from the wind. The control system continuously regulates the rotor speed to maintain an optimal tip-speed ratio, thereby maximizing aerodynamic efficiency [53].

As the wind speed further increases and reaches the rated value, the turbine operates in Zone III, the power regulation region. Here, the output power is intentionally limited to the rated capacity to safeguard the generator and associated mechanical components. This is typically achieved by adjusting the blade pitch angle or employing alternative regulation techniques to prevent mechanical or electrical overload [52] [53].

Finally, when wind velocity exceeds the cut-out speed, the turbine enters Zone IV, where it is shut down for safety reasons. In this condition, no energy conversion occurs, and the system remains inactive until the wind intensity drops back to a secure operational range [52].

In variable-speed WECS based on a SEIG, the aerodynamic control plays a key role in maintaining efficient power extraction and protecting the turbine from mechanical overload. The WT operates with a constant blade pitch angle (β) under normal conditions, particularly in the power maximization region where the MPPT algorithm is applied to ensure optimal use of WE [54]. However, when the wind speed exceeds the nominal value, it becomes necessary to regulate the mechanical power by adjusting the pitch angle to prevent excessive torque and protect the system components.

The blade pitch control system consists of a pitch actuator driven by a proportional controller, which regulates the blade position according to the reference angle β_ref. This configuration is illustrated in Fig (II.6), which shows the orientation system responsible for adjusting the pitch angle as a function of the control input [55].

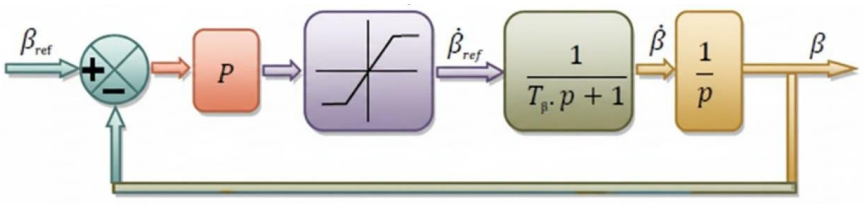

Fig II.6. Blade orientation system.

Furthermore, as shown in Fig (II.7), the overall pitch control loop compares the measured mechanical power P_{meas} with the nominal reference power P_{nom} . The resulting error is processed through a PI controller to generate the appropriate β_ref. This reference angle is then applied to the actuator system in order to reduce the aerodynamic efficiency and limit the captured power. Such a control strategy ensures that the turbine operates safely while maintaining the desired output power level under high wind conditions [55].

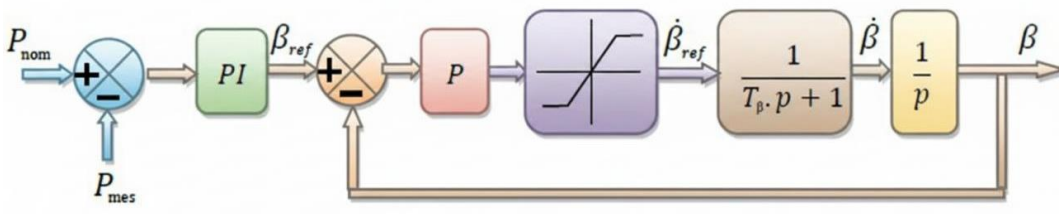

Fig II.7. Pitch angle control for power regulation.

II.3.1.1 MPPT Strategies

The main objective of MPPT control is to continuously adapt the operating point of the WT so that it extracts the maximum available power from the wind under varying conditions. Two main strategies are generally used depending on whether the turbine speed is directly controlled or not [56].

II.3.1.2 MPPT Based on Speed Control

In this control mode, the turbine speed is regulated to maintain operation at the optimal tip-speed ratio λ_{opt} [57].

$$V = \frac{\Omega_T R_T}{\lambda_{opt}} \tag{II.9}$$

λ_{opt}: optimal speed ratio

Accordingly, the optimal torque is written as:

$$T_{Topt} = \frac{1}{2}.\rho.\pi.R_T^3.V^2.\frac{C_p(\lambda_{opt})}{\lambda_{opt}} \tag{II.10}$$

Substituting the wind velocity into this equation yields:

$$T_{Topt} = \frac{1}{2}\rho.\pi.R_T^5.\frac{C_p(\lambda_{opt})}{\lambda_{opt}^3}.\Omega_T^2 \tag{II.11}$$

Thus, the optimal aerodynamic torque is proportional to the square of the turbine speed:

$$T_{Topt} = k_{opt} \cdot \Omega_T^2 \tag{II.12}$$

Where:

$$k_{opt} = \frac{1}{2} \cdot \rho \cdot \pi \cdot R_T^5 \cdot \frac{C_p(\lambda_{opt})}{\lambda_{opt}^3} \tag{II.13}$$

Under steady-state conditions, the mechanical balance can be expressed as [58]:

$$\frac{T_T}{G} - T_m - f.\Omega_m = 0 \tag{II.14}$$

Substituting the above relations gives:

$$\frac{k_{opt}}{G} \cdot \Omega_T^2 - f.\Omega_m - T_m = 0 \tag{II.15}$$

With: $\Omega_m = G.\Omega_T$

If the electromagnetic torque T_g is controlled to follow the optimal torque, the turbine operates along its maximum efficiency curve. The optimal electromagnetic torque is therefore expressed as:

$$T_{emopt} = \frac{k_{opt}}{G^3} \cdot \Omega_g^2 - f \cdot \Omega_m \quad \text{(II.16)}$$

This expression represents the reference torque to be applied to the generator in order to achieve optimal WEC [58]. The block diagram of this control structure is given in the figure below.

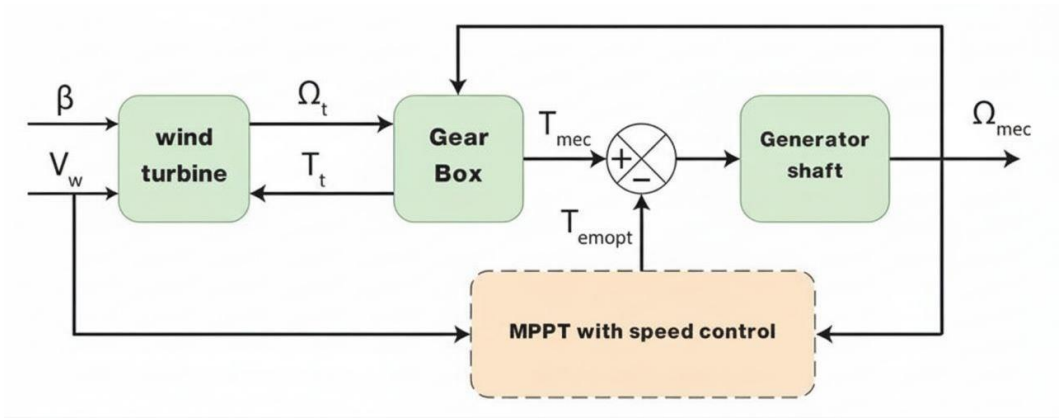

Fig II.8. Block diagram of the WT using MPPT with speed control.

II.3.1.3 MPPT without speed control

When turbine speed control is not implemented, it is assumed that wind variations are slow enough for the system to operate under quasi-steady-state conditions. Consequently, the dynamic term $J\frac{d\Omega_t}{dt} \approx 0$, and the aerodynamic and electromagnetic torques can be considered equal, neglecting the viscous friction torque [59]:

$$T_{em\_opt} = \frac{T_{aer\_estime}}{G} \quad \text{(II.17)}$$

The aerodynamic torque can be estimated using the mechanical speed and wind velocity as [59]:

$$T_{aer\_estime} = \frac{1}{2}\rho.S.C_p \frac{1}{\Omega_{t\_estime}} {v_w}^3 \quad \text{(II.18)}$$

Since direct measurement of the wind speed is often difficult, it can be estimated from [59]:

$$v_{w\_estime} = \frac{R\Omega_{t\_estime}}{\lambda_{opt}} \quad \text{(II.19)}$$

The reference aerodynamic power is then given by [59]:

$$P_{aero\_ref} = \frac{1}{2} C_{p\_opt}.\rho.S.{v_{w\_estime}}^3 \quad \text{(II.20)}$$

Where $S = \pi.R^2$

The corresponding reference electromagnetic torque can be written as:

$$T_{em\_ref} = \frac{P_{aero\_ref}}{\Omega_t} = \frac{1}{2} C_{p\_opt}.\rho.\pi.\frac{R^5{\Omega_t}^2}{{\lambda_{opt}}^3} \quad \text{(II.21)}$$

The turbine speed is estimated from the mechanical speed measurement as:

$$\Omega_{t\_estime} = \frac{\Omega_{m\_estime}}{G} \quad \text{(II.22)}$$

Therefore, the reference torque can be simplified as [59]:

$$T_{em\_ref} = \mathrm{A}.{\Omega_{m\_estime}}^2 \quad \text{(II.23)}$$

With: $T_{em\_ref} = \frac{1}{2} C_{p\_max}.\rho.\pi.\frac{R^5}{{\lambda_{opt}}^3}\frac{1}{G^3}$

The power coefficient $\mathrm{C_p}$ depends on the characteristics of the WT and is typically expressed using empirical relationships. An approximate expression for it is given as follows [51] [59]:

$$Cp\ (\lambda, \beta)\ =\ A1\ ((\frac{A2}{\lambda i})\ - A3 \times \beta - A4)\ exp\ (\frac{A5}{\lambda i})\ +\ A6 \times \lambda \quad \text{(II.24)}$$

Where:

$$A1 = 0.5,\ A2 = 166,\ A3 = 0.4,\ A4 = 5,\ A5 = -21, A6 = 0.0068$$

Figure (II.11) presents the simulated evolution of the power coefficient. C_p as a function of λ and β, showing the maximum value $C_{p_{max}}$ corresponding to the optimal tip-speed ratio λ_{opt}.

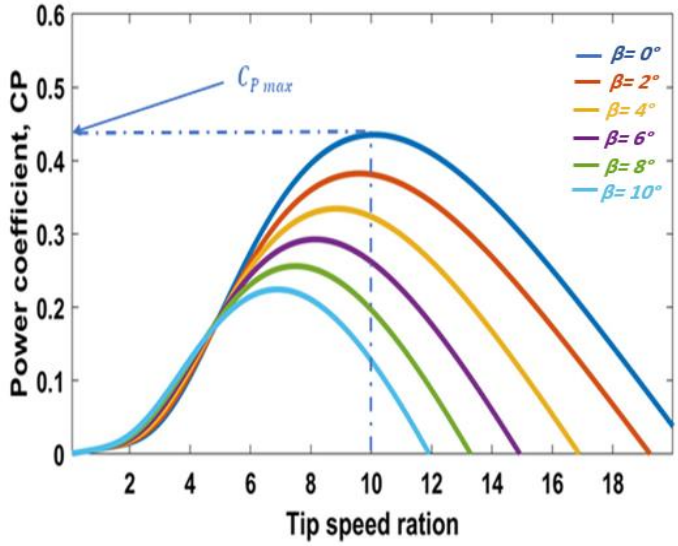

Fig II.9. Power coefficient characteristics.

The block diagram of this control structure is given in the figure below:

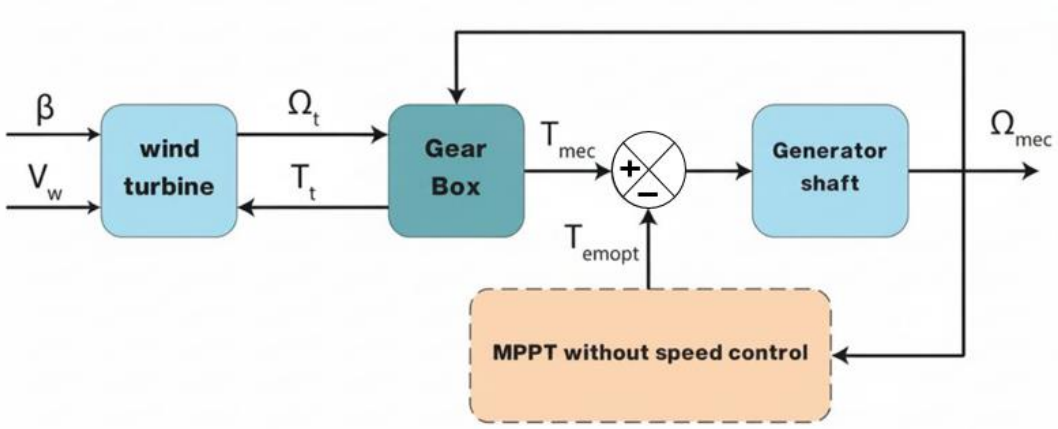

Fig II.10. Block diagram of the WT using MPPT without speed control.

II.3.2 Regulation strategy for the single-input control system

In WES, control loops often exhibit certain imperfections such as insufficient accuracy, limited stability (or even instability), slow dynamic response, and excessive overshoot relative to the desired performance specifications. To overcome these limitations, it becomes essential to integrate a compensator or controller within the feedback loop. The main objective of this compensator is to enhance one or more of these performance parameters such as precision, stability, and speed without compromising the others.

To achieve such optimization, it is necessary to rely on the fundamental principles governing feedback system tuning, typically modeled through linear system representations.

As illustrated in Fig (II.11), the overall structure of the control system can be described using a standard block diagram.

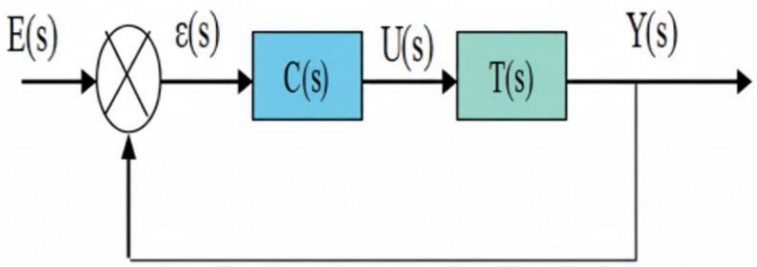

Fig II.11. Block Diagram of a Closed-Loop Controlled System.

When improvement in system characteristics such as precision, stability, or response speed is required, a compensator denoted by $C(s)$ must be introduced into the control loop. The resulting closed-loop configuration enables a more balanced performance, achieving a trade-off between the main dynamic criteria. Ultimately, the design and configuration of the controller depend on the desired system objectives and the control architecture being corrected. Once these are clearly defined, the controller parameters can be properly tuned to ensure optimal behavior and reliable operation of the wind energy conversion system [60].

II.3.2.1 P controller

The P controller represents the simplest form of feedback regulation, primarily influencing the system by adjusting its gain. By doing so, it plays a crucial role in enhancing the system's overall accuracy. In a proportional control scheme, the controller output $U(t)$ is directly linked to the instantaneous error $\varepsilon(t)$ according to [61]:

$$U(t) = K_p.\varepsilon(t) \tag{II.25}$$

Here K_p is the proportional gain coefficient.

In the frequency domain, this relationship is captured by the transfer function:

$$K_p = C(s) = \frac{U(t)}{\varepsilon(t)} \tag{II.26}$$

Modifying the proportional gain produces two significant effects: it reduces the residual steady-state error, improving accuracy, and accelerates the system's dynamic response,

enhancing speed. However, a higher gain can also amplify oscillations and push the system closer to instability, requiring careful tuning to achieve a balanced performance.

II.3.2.2 PI controller

The PI controller combines immediate proportional correction with cumulative integral action to enhance system performance. The control law is expressed as [62]:

$$u(t) = K_i \int_0^t \varepsilon(\tau)d\tau + K_p\varepsilon(t) \quad \text{(II.27)}$$

Where:

$u(t)$: controller output.

$\varepsilon(t)$: instantaneous error, defined as the difference between reference and measured output.

K_p : proportional gain, which amplifies the current error.

K_i : integral gain, representing the effect of accumulated past errors.

τ: dummy variable for integration.

The transfer function in the Laplace domain becomes:

$$C(s) = \frac{K_i}{s} + K_p \quad \text{(II.28)}$$

Key effects of the PI controller:

- Steady-state performance: The integral term eliminates residual error for constant reference inputs.
- Transient response: While improving accuracy, the integral action introduces a phase lag (~-90°), slightly slowing the system and potentially increasing oscillatory behavior.

Proper tuning of K_p and K_i ensures the system remains stable, keeping the phase margin sufficient and the response within acceptable speed and accuracy limits.

II.3.2.3 PD Controller

The PD controller primarily acts on the proportional and derivative terms of the error to enhance system stability and transient response. In a practical PID framework, the integral gain K_i can be added to eliminate steady-state errors [63]:

$$u(t) = K_p\varepsilon(t) + K_d \frac{d\varepsilon(t)}{dt} \quad \text{(II.29)}$$

It enhances the transient response by providing a damping effect, which reduces oscillations and overshoot. However, it does not eliminate the steady-state error for constant reference inputs.

In practical applications, the derivative term is often filtered to reduce noise sensitivity, leading to a modified transfer function:

$$C(s) = K_p(1 + \frac{T_d s}{\tau s+1}) \quad \text{(II.30)}$$

Where T_d is the derivative time constant, which determines the amount of phase lead introduced by the derivative action.

The derivative gain K_d enhances the transient response and stability of the system by predicting future error trends based on the rate of change of the error signal.

II.3.2.4 PID Controller

The PID controller represents the most comprehensive and widely used control strategy, combining the advantages of proportional, integral, and derivative actions to achieve high performance in both steady-state and dynamic conditions. The control law in the time domain is expressed as [64]:

$$u(t) = K_p\varepsilon(t) + K_i \int_0^t \varepsilon(\tau)d\tau + K_d \frac{d\varepsilon(t)}{dt} \quad \text{(II.31)}$$

However, improper tuning of the three gains (K_p, K_i , K_d) can lead to poor system behavior such as oscillations or instability. Therefore, careful parameter adjustment—using tuning methods such as Ziegler–Nichols or other optimization techniques is necessary to achieve an optimal balance between accuracy, speed, and stability.

II.3.2.5 Controller employed for regulating the output voltage of SEIG

The stability of the voltage generated by the SEIG is a key factor in ensuring a reliable and high-quality electrical energy conversion. To ensure a stable DC voltage across the DC bus, it is essential to interface the SEIG configuration with a controlled rectifier, thereby maintaining voltage regulation despite variations in rotor speed and inherent internal fluctuations of the generator.

Control strategies based on a PI regulator rely on adjusting the reference current component I_d^* based on the error between the measured DC voltage and the desired reference voltage, and can be expressed as follows [10]:

$$e(t) = V_{dc}(t) - V_{dc}^{ref} \tag{II.32}$$

The PI controller generates the excitation current command according to:

$$I_d^*(t) = K_p e(t) + K_i \int_0^t e(\tau) d\tau \tag{II.33}$$

And, in the Laplace domain:

$$I_d^*(s) = E(s)\left(K_p + \frac{K_i}{s}\right) \tag{II.34}$$

The signal I_d^* represents the reference current applied to the rectifier to regulate the DC bus voltage, while the quadrature component is set to zero ($I_q^* = 0$) since no inverter or reactive power control is implemented [10].

Any variation in I_d^* directly affects the charging and discharging process of the DC bus capacitor, thereby stabilizing V_{dc} around its desired value [65].

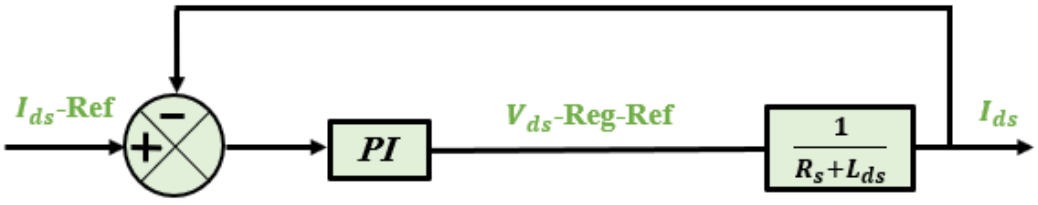

Fig II.12. Control loop of the I_d current.

The block diagram below illustrates the control loop of the I_q current.

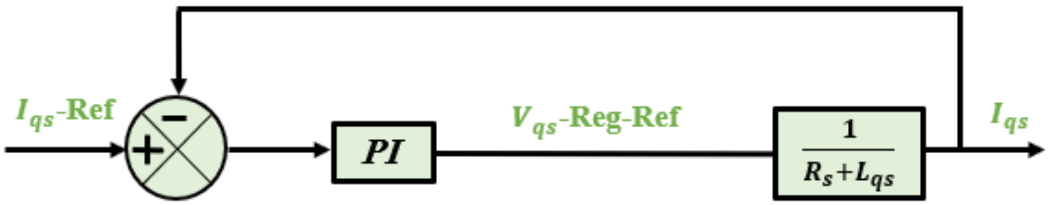

Fig II.13. Control loop of the I_q current.

with: $Iq{-}ref{=}0$

The dynamic behavior of the DC bus voltage is described by:

$$I_{conv}(t) = C\frac{dV_{dc}(t)}{dt} \tag{II.35}$$

Where C is the DC bus capacitance, and I_{Conv} is the current supplied by the rectifier. This relationship highlights the essential role of the capacitor as an energy reservoir that compensates for instantaneous current fluctuations.

In practice, the reference current I_d^* is sent to an inner current control loop, usually implemented using Pulse Width Modulation (PWM), to drive the IGBT switches of the rectifier [10]. To avoid integrator windup during fast voltage transients, an anti-windup mechanism is incorporated in the PI controller. The proportional and integral gains K_p and K_i can be tuned using analytical or empirical techniques such as Ziegler–Nichols, pole placement, or numerical optimization based on the system's transient response. Their optimal values depend on the DC bus characteristics, including its time constant and the rectifier dynamics [10].

Hence, this control approach ensures a stable and well-regulated DC voltage V_{dc}, guaranteeing reliable operation of the SEIG–rectifier system, even in the presence of rotor speed variations, and maintaining high output power quality. With the continuous progress in power electronics technology, converters have become increasingly efficient, compact, and cost-effective, enabling their widespread use in wind energy conversion systems [66].

These devices not only provide the desired electrical waveform and voltage level but also enhance the efficiency of power extraction from the turbine [66].

This architecture is widely used due to its ease of implementation, the maturity and reliability of IGBT-based devices, and its capability to stabilize the DC bus voltage through current regulation using a PI controller.

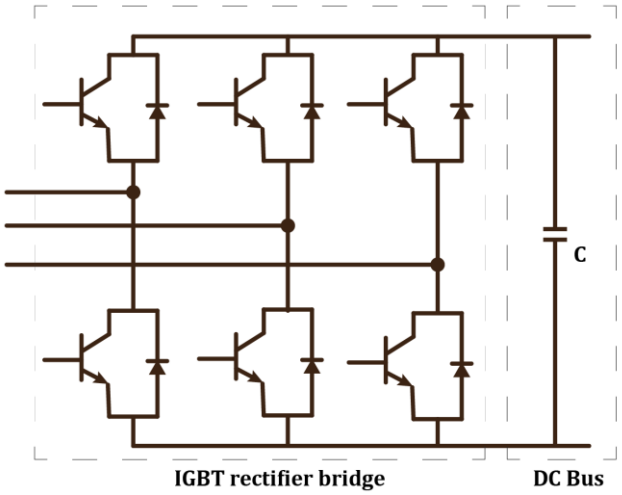

Fig II.14. Converter Diagram.

The PLL configuration shown in Fig (II.15) extracts the instantaneous phase and frequency of the system from the stator three-phase voltages Vas, Vbs,Vcs of the SEIG. The extracted phase angle is then used to transform electrical quantities from the abc reference frame to the rotating dq frame.

This configuration ensures accurate tracking of the stator voltage vector's angular position maintaining synchronization between the rotating reference frame and the SEIG voltages, even under rotor speed variations [67].

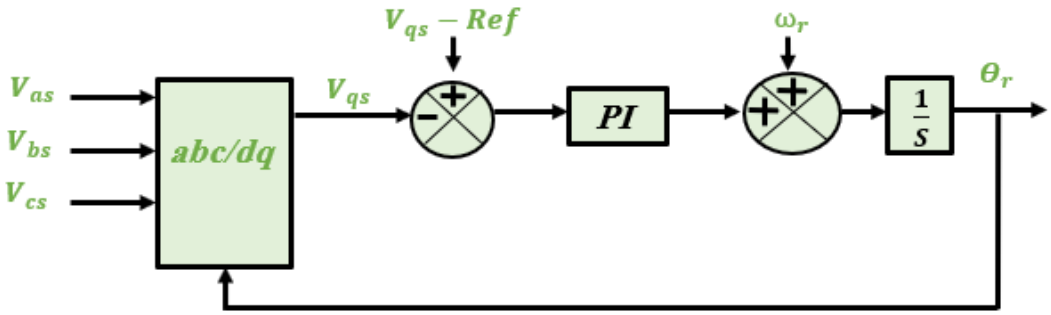

Fig II.15. The Phase-Locked Loop.

With $V_{qs} - Ref = 0$

Fig (II.16) illustrates the electrical model of the DC bus. The relationship between the currents and the bus voltage is expressed by equation (II.36) [68].

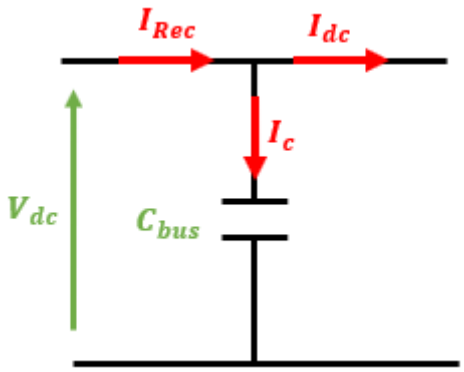

Fig II.16. Electrical diagram of the DC bus.

Where:

$$\begin{cases} I_{dc} = I_{rec} - I_C \\ I_C = C_{bus}.\frac{d}{dt}(V_{dc}) \end{cases} \quad \text{(II.36)}$$

Using both expressions, the DC voltage regulation loop is defined as a function of the current I_{ds}, as shown in Fig (II.17) [68].

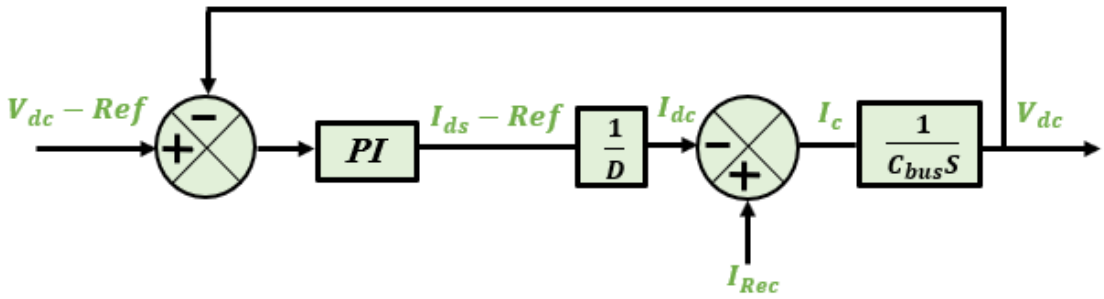

Fig II.17. Principle of DC bus voltage regulation.

The parameters K_{p-dc} and K_{i-dc} of the Proportional–Integral (PI) controller are determined from equation (II.38). For the DC bus voltage regulator, $a = 0$ and $b = D.C_{bus}$. Since the control loops are arranged in cascade, the time constant of the voltage regulator is given by [69]:

$$\tau_{n-dc} = 100\left(\frac{\frac{L_S}{R_S}}{10}\right) \quad \text{(II.37)}$$

$$\begin{cases} K_{i-dc} = D.C_{bus}.\omega_{n-dc}^2 \\ K_{p-dc} = 2.\xi.D.C_{bus}.\omega_{n-dc} \end{cases} \quad \text{(II.38)}$$

With:

$D = \frac{2V_{dc}}{3V_{ds}}$; $\omega_{n-dc} = \frac{1}{\tau_{n-dc}}$

Where:

ξ : The damping coefficient.

C_{bus} : The capacitance of the DC bus.

The time constant of the DC bus is calculated based on the active power flowing through the bus, its capacitance, and its voltage [70], as shown in equation (II.59).

$$\tau = \frac{CV_{dc}^2}{2P_n} \quad \text{(II.39)}$$

Where: P_n is the active power [W], V_{dc} is the DC bus voltage [V], and C is the DC bus capacitance [F].

The capacitance of the DC bus is determined using equation (II.60), taken from reference [70].

$$C = \frac{S}{V_{dc}\Delta V_{dc}.2\omega} \quad \text{(II.40)}$$

Where: S is the apparent power [VA], V_{dc} is the DC bus voltage [V], ΔV_{dc} is the voltage drop across the DC bus [V], and ω is the electrical angular frequency of the grid [rad/s].

II.3.3 FEM based SEIG Modeling

The FEM is one of the most powerful and widely used numerical techniques for analyzing electrical machines and generators, including SEIGs [71] [5] [72]. This method allows the transformation of complex partial differential equations governing electromagnetic, electrical, and mechanical behavior into algebraic equations that can be solved numerically. By doing so, FEM provides an accurate assessment of voltage, current, and torque distributions,

while also accounting for nonlinear effects such as magnetic saturation and the impact of connected loads. FEM has become an indispensable tool in modern machine design and performance analysis, enabling engineers to predict machine behavior under a wide range of operating conditions before physical prototyping [5].

The working principle of FEM is based on subdividing the geometry of the machine into small discrete elements, typically triangles in two-dimensional (2D) models or tetrahedra in three-dimensional (3D) models [73]. Within each element, the variables are approximated using shape functions, and the contributions from all elements are assembled to form a complete numerical mesh representing the entire machine [71]. The accuracy of the solution strongly depends on the size of the elements: smaller elements provide more precise results but at the cost of increased computational effort.

The general two-dimensional formulation of Maxwell's equations is expressed as [73]:

$$\nabla \times \vec{E} = \frac{\partial \vec{B}}{\partial t} \tag{II.41}$$

This equation describes how a time-varying magnetic field induces a circulating electric field, where $\vec{E}$ is the electric field intensity, $\vec{B}$ is the magnetic flux density, t is time, and ∇ is the curl operator denoting the rotational derivative of a vector field. Here, ∂ represents a partial derivative [37].

The Maxwell–Ampère Law is expressed as follows [73]:

$$\nabla \times \vec{H} = \overrightarrow{J_e} + \frac{\partial \vec{D}}{\partial t} \tag{II.42}$$

Where $\vec{H}$ is the magnetic field intensity, $\overrightarrow{J_e}$ is the conduction current density, and $\vec{D}$ is the electric flux density. In practical applications, particularly at industrial frequencies, the displacement current term $\frac{\partial \vec{D}}{\partial t}$ is very small and can be neglected. Thus, Equation (II.62) simplifies to [37] [71]:

$$\nabla \times \vec{H} = \overrightarrow{J_e} \tag{II.43}$$

The relationship between the electric flux density and the free electric charge density ρ_e is given by:

$$\nabla . \vec{D} = \rho_e \tag{II.44}$$

Since the divergence of the curl of any vector field is always zero, applying this property to the Maxwell–Ampère Law leads to the general continuity equation [37] [71]:

$$\nabla.\left(\nabla\times\vec{H}\right) = \nabla.\overrightarrow{J_e} = 0 \quad \text{(II.45)}$$

This equation represents the conservation of electric charge, implying that, in steady-state or low-frequency applications where the displacement current is negligible $\frac{\partial\vec{D}}{\partial t} \approx 0$ and charge accumulation is minimal $\frac{\partial\rho_e}{\partial t} \approx 0$, the net current entering a closed surface is equal to the net current leaving it.

The electromagnetic behavior of materials is governed by Ohm's law in differential form:

$$\overrightarrow{J_e} = \sigma\vec{E} \quad \text{(II.46)}$$

where σ represents the electrical conductivity of the material

The electric flux density can be formulated as [37]:

$$\vec{D} = \varepsilon\vec{E} = \varepsilon_0\varepsilon_r\vec{E} \quad \text{(II.47)}$$

Where,ε_0 is the permittivity of free space, and ε_r is the relative permittivity.
The magnetic flux density can be written as:

$$\vec{B} = \mu\vec{H} = \mu_0\mu_r\vec{H} \quad \text{(II.48)}$$

Where, μ is the permeability, μ_0 is the permeability of free space, and μ_r is the relative permeability.

The modeling procedure begins with the definition of the stator slot geometry, as shown in Fig (II.18) where the slot dimensions and winding layout are carefully specified to reflect the real machine design. The rotor slots were designed with a slight skew angle to reduce cogging torque and mitigate magnetic locking between the stator and rotor teeth [5] [73].

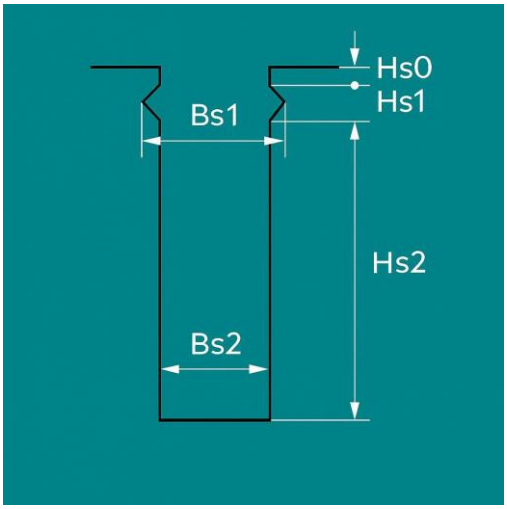

Fig II.18 Stator slot

Next, the rotor slot geometry is constructed, as shown in Fig (II.19) ensuring that the bar placement and end-ring connections are properly represented.

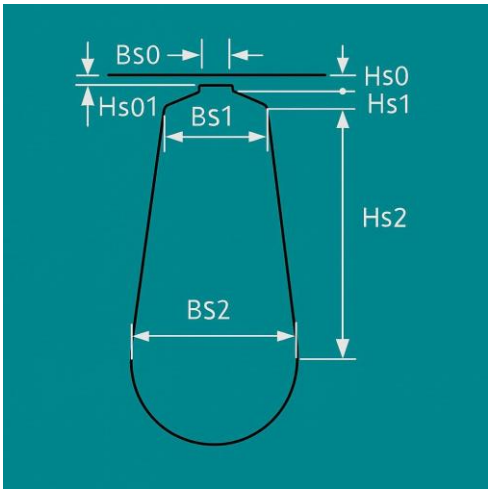

Fig II.19 Rotor slot

In order to establish the magnetic field formulation, a two-dimensional computational domain is defined and subdivided into conductive and non-conductive zones, as shown in Fig (II.20) This domain corresponds to the cross-sectional view of an induction motor with an axial length L_δ. The conductive parts consist of the stator slot windings Ω_s and the rotor barsΩ_b, whereas the non-conductive regions include the ferromagnetic core Ω_{core} and the air-gap region Ω_{air} [37].

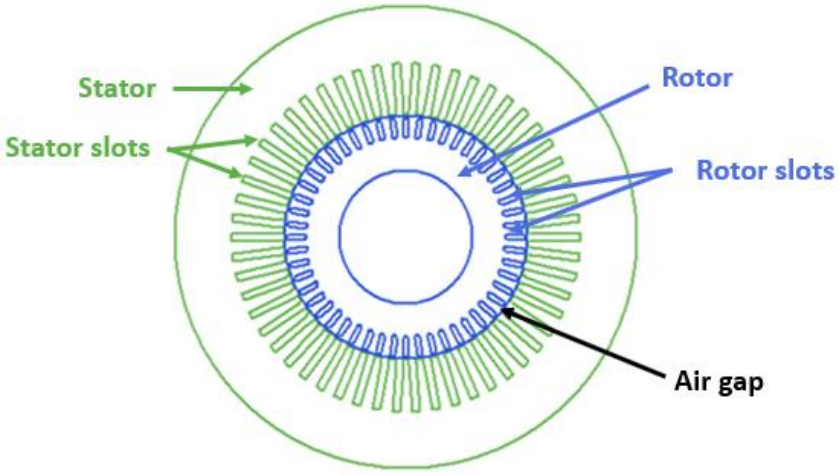

Figure II.20. Geometric structure of the induction machine.

In formulating the mathematical model based on the magnetic vector potential for a three-phase induction machine, it is assumed that the magnetic field is confined within the (x, y) plane [5]. Hence, only the z-direction components of the induced current and magnetic vector potential are taken into account. The magnetic cores of the machine are considered nonlinear materials, and their behavior is represented using Marrocco's nonlinear reluctivity approximation. This approach employs a single-valued nonlinear function of the magnetic flux density B, while disregarding the influence of hysteresis [37].

The equation that describes the spatial and temporal dependence of the magnetic vector potential, represented by $A = (0,0,A_z(x,y,t))$, is expressed as follows [37]:

$$\frac{\partial}{\partial x}\left(v(B^2)\frac{\partial A_z(x,y,t)}{\partial x}\right)+\frac{\partial}{\partial y}\left(v(B^2)\frac{\partial A_z(x,y,t)}{\partial y}\right)=-d\frac{N_{cn}I_n^s}{S_n}+\sigma\left(-\frac{\partial A_z(x,y,t)}{\partial t}\right)+\frac{U_m^r}{L_\delta} \quad \text{(II.49)}$$

The magnetic field in an electric machine arises from coil currents. Modeling the power supply as a voltage source allows simultaneous solution of circuit and magnetic field equations. Stator windings are treated as thin filamentary conductors, while rotor bars are modeled as solid conductors including eddy current effects [37].

For a step-by-step general solution of the magnetic field in rotating electrical machines, the magnetic field equations of the stator and rotor are expressed in their respective coordinate systems. The solutions of both field equations are then coupled within the air gap. At each time step, the rotor is rotated by an angle corresponding to the mechanical angular frequency, which

means that a new finite element mesh must be generated in the air gap. The general form of the air-gap element matrix is given by the following expression [37]:

$$A(a,b,r,\theta)=\sum_{j=1}^{mnt}A_i\left[\frac{1}{2}a_{0j}+\sum_{r=1}^{\infty}[a_{rj}cos(\lambda_r\theta)+b_{rj}sin(\lambda_r\theta)]\right]=\sum_{j=1}^{mnt}(N_j^{AGE}(a,b,r,\theta))A_j^{\Gamma AGE} \tag{II.50}$$

Where (a_{0j}, a_{rj}, b_{rj}, λ_r) are the Fourier series expansion coefficients that depend on the coordinates of the air-gap nodes, and mnt is the total number of air-gap nodes.

The electromagnetic torque is calculated from the Maxwell stress tensor based on the radial and tangential components of the magnetic flux density as follows [37]:

$$C_{em}=\frac{Pr^2l_\delta}{\mu_0}\int_{\theta1}^{\theta2}B_rB_\theta d\theta \tag{II.51}$$

Where r is the outer radius of the rotor and ppp is the number of pole pairs. The magnetic components of the flux density (B_r, B_θ) are calculated within the air-gap boundaries using the analytical derivatives of the magnetic vector potential based on the shape functions (II.52).

In a general case, the magnetic field equations and the electrical circuit equations are coupled with the rotor's mechanical equation through the electromagnetic torque. This highlights the interaction between mechanical and electromagnetic quantities. The mechanical equations governing the differential system of angular speed and angular displacement are given as follows [37]:

$$\frac{d}{dt}\begin{bmatrix}\omega\\ \theta\end{bmatrix}=\begin{bmatrix}-\frac{f}{j_m} & 0\\ 1 & 0\end{bmatrix}\begin{bmatrix}\omega\\ \theta\end{bmatrix}+\begin{bmatrix}\frac{1}{j_m}(C_{em}(t)-C_{load})\\ 0\end{bmatrix} \tag{II.53}$$

At each time step, the computed electromagnetic torque is applied to the mechanical model represented by equation (II.71) using the fourth-order Runge-Kutta method to obtain the rotor's angular displacement and speed.

II.3.3.1 Geometry and Physical Description of the 2D Model

Accurately modeling the machine requires accounting for terminal effects, such as inductances, end-winding resistances, end rings, and bars. This connection is essential as simulations provide insights into the machine's behavior under various load conditions. The induced rotor currents in the no-load state cannot be overlooked, necessitating the inclusion of the cage in the model. Additionally, this approach allows for the direct application of voltage

to the equipment. Figs (II.23) show the equivalent circuits of the stator combined with the FE model [37].

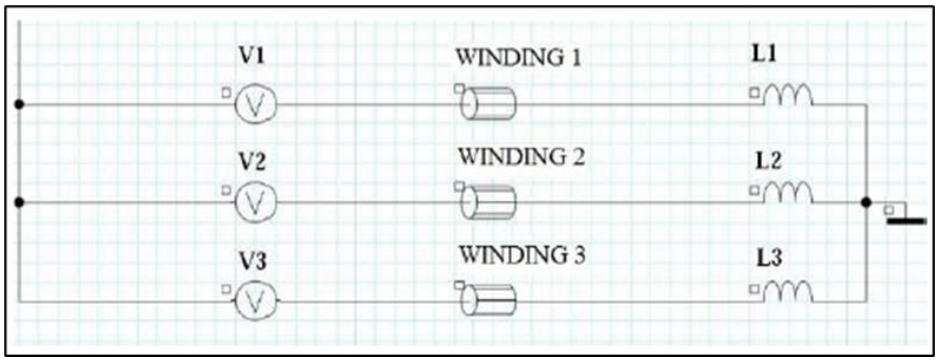

Fig II.21. stator's equivalent circuit combined with the FE model.

At the start, the machine has no inherent magnetization, but the software induces the required magnetic field during the simulation process [71]. The stator terminals are connected to precisely calculated excitation capacitors, while the rotor operates at a speed slightly higher than the synchronous speed by a suitably chosen margin [74].

II.3.3.2 Magnetic Circuit Meshing

During the meshing stage, the induction machine's geometry is discretized into finite elements to enable numerical analysis. The FEM approach consists of subdividing the computational domain into smaller, well-defined shapes typically triangular or quadrilateral elements. As shown in Fig (II.25), the mesh is refined in the air gap region to accurately capture the strong electromagnetic coupling between stator and rotor, while a coarser mesh is used near the shaft and the outer frame to optimize computational efficiency without compromising precision. Since the outer casing is grounded, a Dirichlet boundary condition with zero magnetic vector potential is imposed along the machine's outer boundary [5].

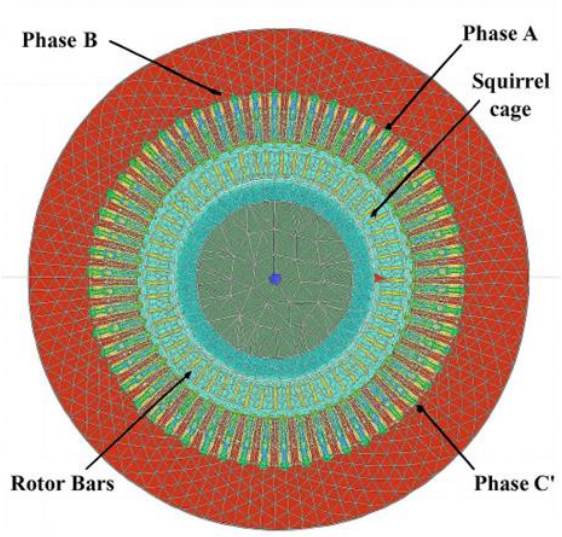

Fig II.22. The mesh.

Among the most widely used FEM software packages for electrical machine analysis are ANSYS Maxwell, JMAG, COMSOL Multiphysics, MATLAB PDE Toolbox, Altair Flux, and Opera. These platforms provide comprehensive environments for modeling complex machine geometries, simulating electromagnetic fields, and evaluating the influence of saturation, load conditions, and excitation capacitors on generator performance [37].

II.4 Conclusion

This chapter presents the theoretical and modeling framework of the WECS based on the SEIG. It begins with an explanation of the operating principle of the SEIG, highlighting the voltage build-up mechanism under different operating conditions, including self-excitation and loaded operation. The chapter also addresses wind turbine modeling, emphasizing the relationship between wind characteristics and extracted power.

Subsequently, the chapter investigates wind turbine control approaches, focusing on MPPT strategies, including both speed-controlled and non-speed-controlled techniques.

In addition, voltage regulation strategies for single-input control systems are examined through a detailed analysis of P, PI, PD, and PID controllers, leading to the identification of the most suitable controller for regulating the output voltage of the SEIG.

Finally, the chapter incorporates FEM based modeling of the SEIG, presenting the geometric and physical description of the two-dimensional model along with the magnetic circuit meshing, in order to achieve an accurate representation of the generator's electromagnetic behavior.

III. Chapter 03: Simulation and analysis of results

III.1 introduction

This chapter presents the simulation procedures and corresponding results obtained for the proposed wind energy conversion system. The study was performed in two main stages to ensure both system-level and detailed electromagnetic validation.

Firstly, a FEM simulation was conducted to evaluate the current and voltage characteristics of the 4.087 MW SEIG under healthy conditions, considering both no-load and load operating modes.

Secondly, a FEM analysis was carried out to evaluate the current and voltage characteristics of the 4.087 MW SEIG under different operating states.

III.2 FEM simulation results

III.2.1 FEM-based simulation of the SEIG model

In this work, a two-dimensional FEM model of a 4.087 MW, two-pole squirrel-cage SEIG, rated at 3000 V RMS, was designed and simulated using Ansys Maxwell 2D. The machine geometry was developed based on actual design specifications, while material properties were defined using nonlinear magnetic characteristics. To mitigate cogging torque and prevent unwanted magnetic attraction between stator and rotor teeth, a slight skew was introduced in the rotor slots. The computational domain was discretized into finite elements, with enhanced mesh resolution applied in sensitive regions such as the air gap and stator slots to improve numerical precision. Appropriate boundary conditions were imposed to accurately represent the magnetic field distribution and to minimize numerical distortions. For the transient state finite element analysis (TSFEM), a rigorous numerical framework was adopted to ensure accuracy and repeatability. The model employed a high-resolution mesh of approximately 85,000 quadratic elements, with additional refinement in critical zones—particularly within the air gap and along the stator and rotor tooth edges—to accurately capture magnetic saturation effects and detailed flux distributions. The transient simulation was performed over a total time

interval of $T_{end} = 5\ s$ in order to fully capture the generator startup behavior. Time integration was carried out using the Backward Euler scheme, selected for its strong numerical stability when dealing with nonlinear transient electromagnetic systems. The General Transient solver with field decomposition was adopted for the analysis. To ensure adequate convergence and numerical reliability, the nonlinear residual tolerance was carefully specified as 10^{-4}. In addition, an adaptive time-stepping strategy was applied, with the time step varying between a minimum value of $H_{min} = 0.001\ s$ and a maximum value of $H_{max} = 1s$.

The proposed model was evaluated under both no-load and loaded operating conditions, with multiple operating points selected to represent realistic working scenarios. During the simulations, essential electromagnetic quantities such as magnetic flux distribution, induced current profiles, and core loss components were continuously observed. Progressive excitation capacitor faults were implemented by gradually altering the capacitance value, allowing the investigation of the system response to different levels of degradation. In comparison with simplified analytical approaches, the FEM-based methodology demonstrated superior accuracy in representing nonlinear phenomena and complex machine geometries, while also offering enhanced flexibility for assessing a wide range of operating conditions and fault cases. The block diagram used in this study is illustrated in Fig (III.1).

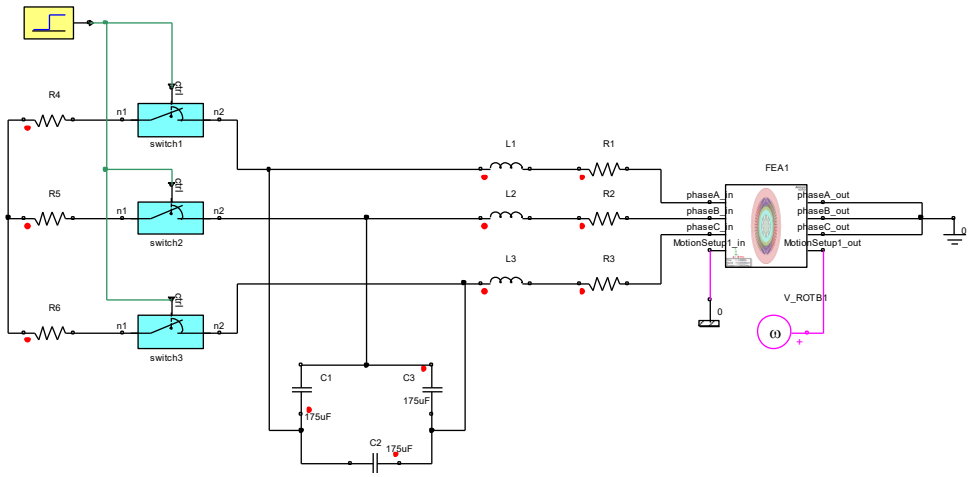

Fig III.1 block diagram

The machine parameters adopted in this work are listed in Table III-1 and were chosen to correspond to those of an actual industrial SEIG, thereby ensuring both the validity of the numerical model and its relevance to practical applications.

Table III-1 SEIG Parameters.

parameter	values	parameter	values
Rated full-load Power	4.087 MW	Power factor PF	0.92563
Rated line voltage (RMS)	3000 V	synchronous speed	3110 rpm
Fundamental frequency	51.83 Hz	Coupling method	Wye
Number of poles	2	Rotor slots	52
Stator slots	54	Operating temperature	75 °C

The two-dimensional Maxwell FEM model, illustrated in Fig (III.2), was developed to analyze the electromagnetic behavior of the machine. The magnetic flux density distribution obtained from the simulation, shown in Fig (III.3), highlights the spatial variation of magnetic flux throughout the machine, thereby confirming the model's capability to accurately capture its dynamic electromagnetic behavior.

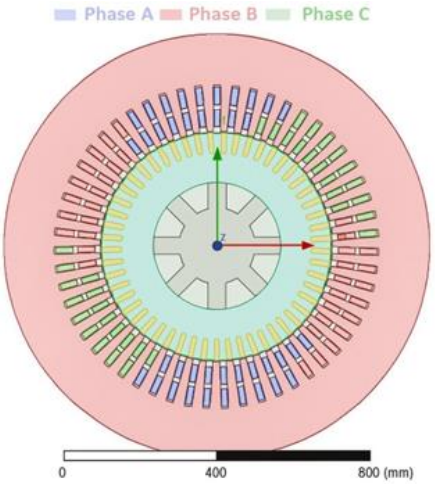

Fig III.2 Two-dimensional Maxwell FEM model

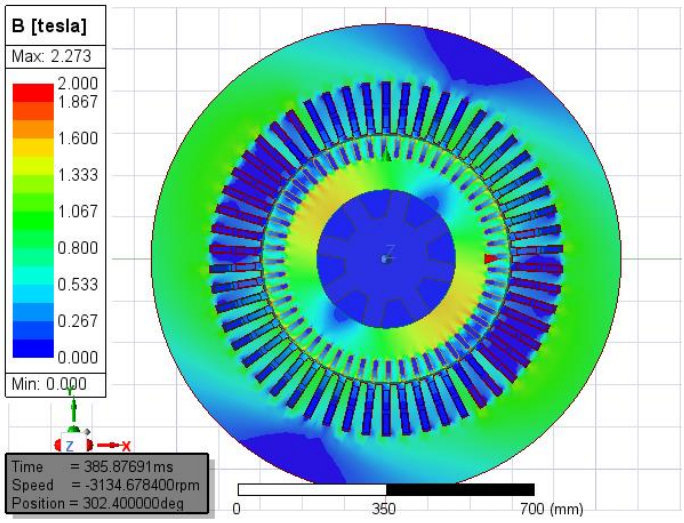

Fig III.3 The corresponding electromagnetic field distribution.

III.2.2 Experimental Arrangement and Fault Scenario Simulation

The minimum excitation capacitance for SEIGs is often determined graphically from the magnetization characteristics, representing the lowest value required for self-excitation under no-load conditions [75]. However, in this study, the operational capacitance was primarily determined experimentally. Capacitance values, ranging from 100 µF to 175 µF per branch delta connection (C_Δ), were tested until the rated voltage was achieved under no-load conditions. In parallel, the capacitance values were estimated based on the generator's reactive power using relationship (III.1). These theoretical values served as an initial reference for comparison with the experimentally obtained operational capacitances, acknowledging that the analytical approach does not fully account for the SEIG's nonlinear magnetic characteristics and losses. This dual approach provides a validation of the experimental findings against theoretical expectations [75] [5].

$$Q = 3V_L^2 \omega C_\Delta \tag{III.1}$$

In a delta connection (Δ), each capacitor is subjected to the line-to-line RMS voltage V_L. Hence, the required capacitance per branch is:

$$C_\Delta = \frac{Q}{3V_L^2 \omega} \tag{III.2}$$

Where $\omega = 2\pi f$

In a star (Y) configuration, each capacitor is connected between a phase and the neutral point, and therefore each one experiences the phase voltage $V_{ph} = \frac{V_L}{\sqrt{3}}$. The corresponding relation becomes:

$$Q = 3V_{ph}^2 \omega C_Y \quad \text{(III.3)}$$

This gives the conversion between the two configurations:

$$C_Y = 3C_\Delta \quad \text{(III.4)}$$

Since the excitation capacitors in this study are delta-connected, each capacitor is subjected to the full V_L . Given the generator data:

$$S = \frac{P}{PF} = \frac{4.087 \times 10^6}{0.92563} = 4.4152746 \times 10^6 \quad \text{(III.5)}$$

$$\Phi = \cos^{-1}(PF) = 0.388 \text{ rad} \quad \text{(III.6)}$$

$$Q = P \tan \Phi = 1.6708714 \times 10^6 \, VAR \quad \text{(III.7)}$$

$$V_L = 3000V, \; f = 51.83 \, Hz.$$

The angular frequency is:

$$\omega = 2\pi f = 2\pi(51.83) = 325.657 \, rad/s \quad \text{(III.8)}$$

Substituting into the delta-connection formula:

$$C_\Delta = \frac{1.6708714 \times 10^6}{3 \times (3000)^2 \times 325.657} = 190.0283 \, \mu F \quad \text{(III.9)}$$

The equivalent per-phase capacitance in a star configuration is:

$$C_Y = 3C_\Delta = 570.0848 \, \mu F \quad \text{(III.10)}$$

The generator was started by rotating the rotor at a speed slightly above the synchronous speed (3135 rpm) without load for a specified period to allow self-excitation. Once the current and voltage reached a steady state, a three-phase balanced load was connected at 7 seconds to establish the healthy operating condition before investigating the imbalanced load fault.

III.2.3 Analysis of TSFEM Results under Healthy and Faulty Conditions

III.2.3.1 Dynamic Response during No-Load Startup

This subsection reports the TSFEM simulation results obtained under healthy operating conditions, corresponding to an excitation capacitance of 175 µF. Figs (III.4-5) depict the transient evolution of the stator voltage and current during the no-load startup process.

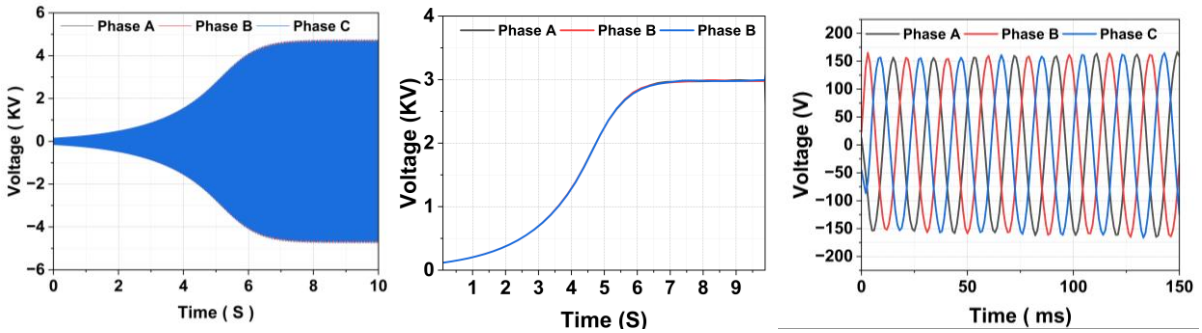

(a) Voltage buildup (b) RMS voltage (c) Zoom on the startup voltage

Fig III.4 Transient Voltage Response during No-Load Operation

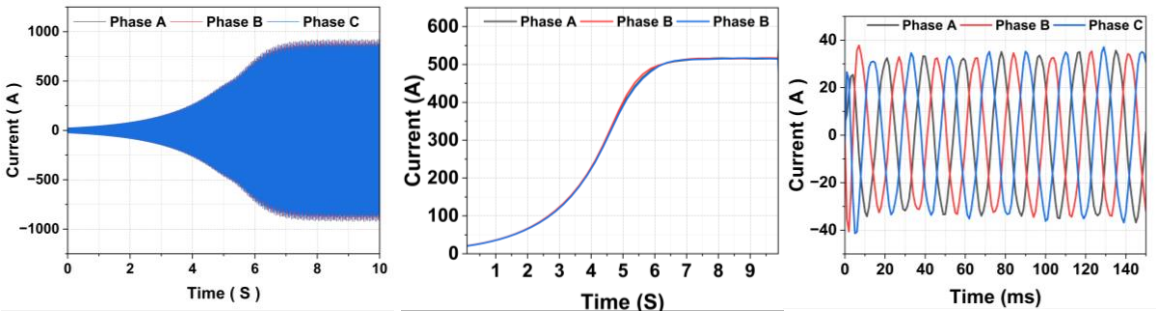

(a) Line current (b) RMS current (c) Zoom on the startup current

Fig III.5 Transient Current Response during No-Load Operation

As illustrated in Fig (III.4-5), the system achieves steady-state operation after approximately 8 seconds, exhibiting balanced three-phase voltage and current waveforms. This confirms the successful self-excitation of the machine and synchronization of the rotor.

III.2.3.2 Transient Dynamic Response under Loaded Operation

Fig (III.6) presents the TSFEM results for the generator connected to a balanced three-phase purely resistive load (R = 20 Ω) with an excitation capacitance of 190 µF. The load was applied at t = 7 s, after which the RMS current stabilized at 581.74 A, while the terminal voltage decreased and reached a steady value of 2889.42 V. This voltage drop is characteristic of SEIG, where voltage generation relies on the interaction between residual magnetism and the excitation capacitance. Upon load connection, the increased current draw reduces the internal magnetic flux, resulting in a corresponding decrease in output voltage behavior that aligns with established observations in standalone induction generator studies.

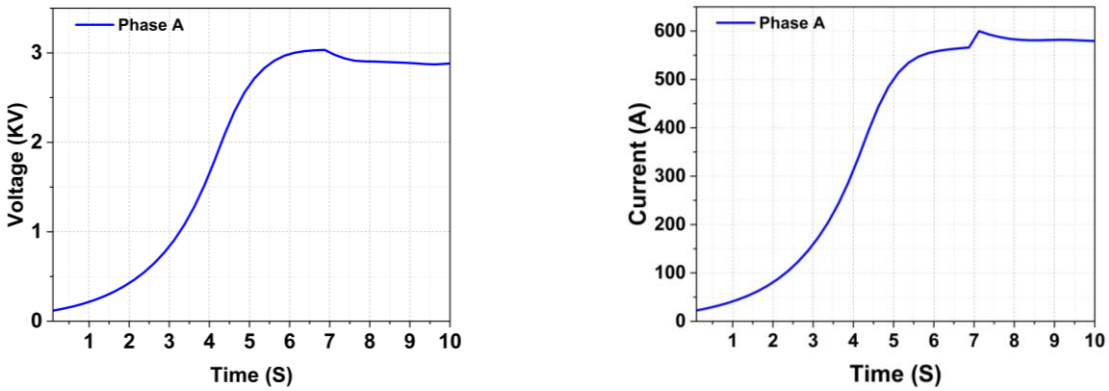

(a) Voltage (b) Current

Fig III.6 Time-Domain RMS Voltage and Current Response under Load Conditions

Fig (III.7) depicts the transient behavior of the generator torque during the transition from no-load to loaded operation. Prior to t = 7 s, the torque remains approximately –5 kNm, increasing to about –8.5 kNm following load application, indicating a rise in electromagnetic torque. This response is typical for SEIGs, where load connection increases the rotor current, thereby reducing the internal magnetic flux and causing a voltage drop. Simultaneously, the electromagnetic torque adjusts to balance the mechanical torque supplied by the turbine. This variation illustrates the generator's natural physical response in maintaining energy equilibrium between mechanical and magnetic power under load conditions.

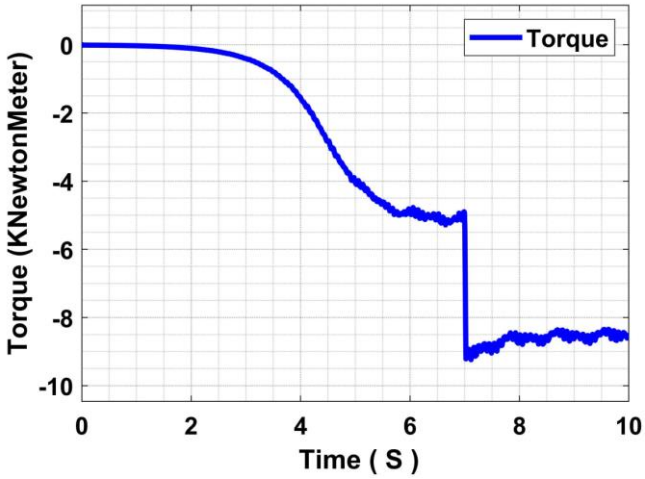

Fig III.7 Dynamic Torque Response under Loaded Operation

Fig (III.8) illustrates the RMS behavior of voltage and current signals for various excitation capacitance values under different load conditions.

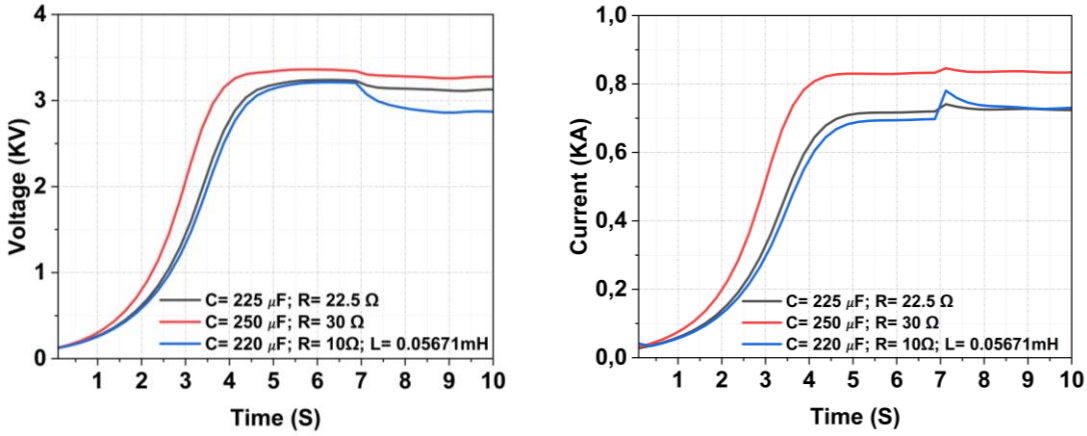

(a) Voltage (b) Current

Fig III.8 Voltage and Current RMS under Varying Capacitor Values and Loads

Table (III-2) provides a comparison of the generator's operating conditions for various excitation capacitance values and load scenarios.

Table III-2 Analysis and Comparison of Operational Conditions

Experience	Per phase capacitor value (C)	Per phase Resistor value (R)	Per phase Inductance value (L)	Voltage (RMS)	Current (RMS)
1	175 μF	0	0	3000 V	550 A
2	190 μF	20 Ω	0	2889.42V	581.74 A
3	225 μF	22.5 Ω	0	3112V	725.7A
4	250 μF	30 Ω	0	3276 V	834 A
5	220 μF	10Ω	0.0567 mH	2874 V	729A

III.2.3.3 Analysis of SEIG Response under an Unbalanced RL Load Fault

In this section, the stator phases A, B, and C are connected to an unbalanced RL load at t = 7 s, after the system has reached steady-state no-load conditions. The load is characterized by the following parameters:

Phase A: $R_A = 10\ \Omega, L_A = 0.057\ mH$.

Phase B: $R_B = 15\ \Omega, L_B = 0.06\ mH$.

Phase C: $R_c = 8\ \Omega, L_C = 0.05\ mH$.

corresponding to a per-phase excitation capacitance of 220 µF.

The dynamic analysis indicates that connecting the generator to an unbalanced RL load at t = 7s, following the initial steady state under balanced no-load voltage conditions of approximately 3195 V, leads to a non-ideal operating scenario. This condition is characterized by a pronounced imbalance in the phase currents and a moderate, yet acceptable, decrease in the steady-state voltage to approximately 2900 V.

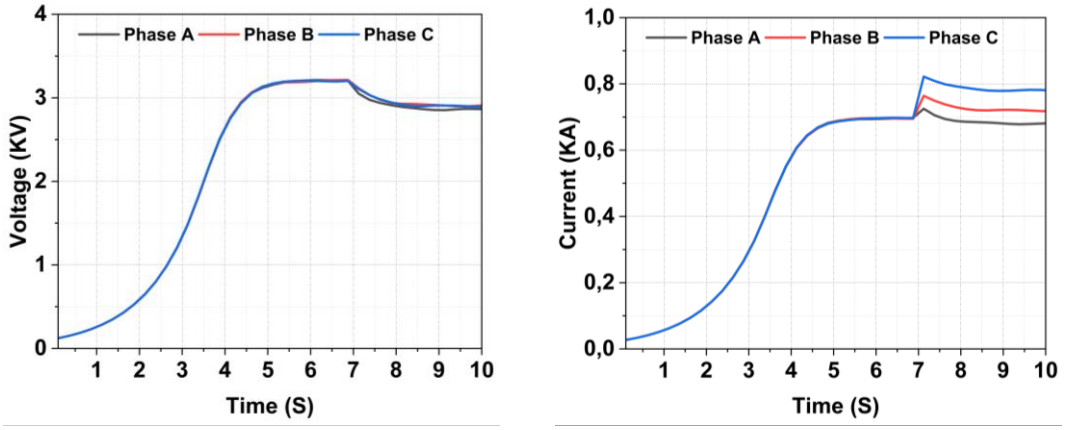

(a) RMS voltage (b) RMS current

Fig III.9 . Three-Phase Voltage and Current RMS under Unbalanced Loading

As shown in Fig (III.9), the uneven distribution of phase currents indicates that Phase C, having the lowest impedance, carries the highest current of approximately 780 A, whereas Phase B, with the highest impedance, carries the lowest current of around 679 A. Eventually, Phase C stabilizes near 721 A. This imbalance directly reflects the presence of negative-sequence current components (I_2) in the stator. These (I_2) components are the primary source of a reverse-rotating magnetic field, which induces a pulsating torque, thereby increasing mechanical stress and vibrations, as illustrated in Fig (III.10).

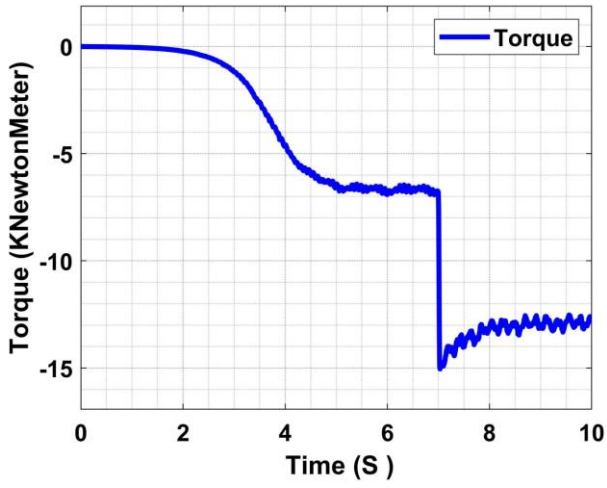

Fig III.10 Torque Dynamics under Unbalanced Loading

Moreover, the presence of negative-sequence currents increases rotor copper losses, potentially compromising the long-term thermal stability and operational efficiency of the generator. FFT analysis of the SEIG current under both balanced and unbalanced load

conditions provides clear insight into the effects of load imbalance on power distribution. As illustrated in Fig III.11(b), connecting the unbalanced load results in a sharp reduction of the fundamental frequency component (51.704 Hz) to approximately 0.51758. This dramatic decrease over 800 times lower than that observed under balanced conditions in Fig III.11(a) demonstrates that the impedance imbalance causes uneven power distribution among the phases, thereby reducing the power transfer efficiency at the fundamental frequency. Additionally, the unbalanced load induces negative-sequence current components. Although the second harmonic of the fundamental frequency (2f, around 252.93 Hz) may not be prominently visible within the displayed frequency range, the substantial reduction in the fundamental amplitude remains the most critical indicator of imbalance and the consequent degradation of the generated power quality.

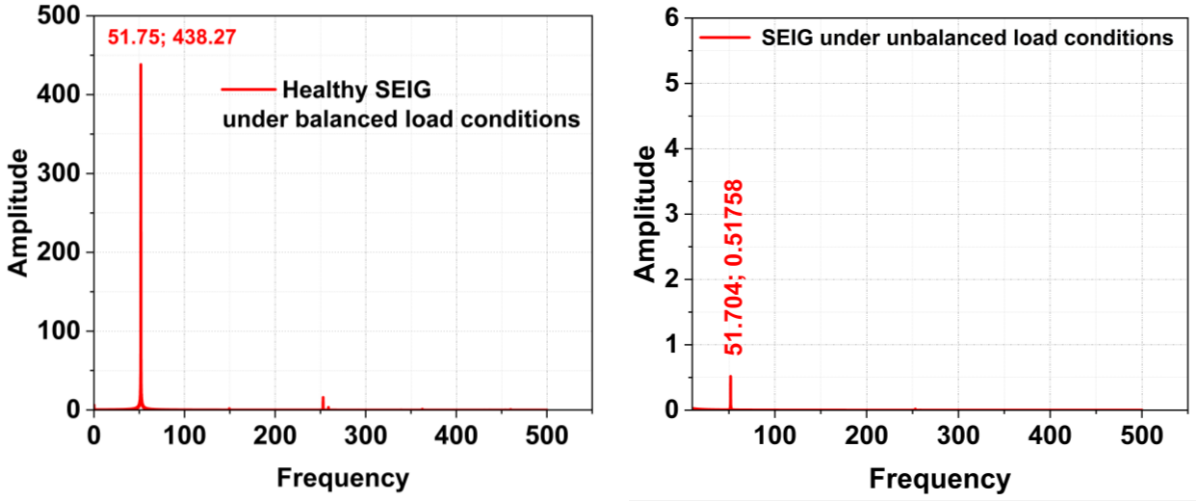

(a) FFT Under balanced load state (b) FFT Under unbalanced load state

Fig III.11 . Single-Sided FFT Amplitude Spectrum of SEIG Current under Unbalanced Load

III.2.3.4 Transient Response under an Open-Phase Fault

Once the generator reaches steady-state voltage, a balanced three-phase load is applied at t = 7 **s**. t = 8 **s**, phase A is abruptly disconnected, triggering a critical transition from balanced three-phase operation to an unbalanced two-phase condition. As depicted in Fig (III.12), the current in phase A drops immediately to zero, while the currents in the healthy phases (B and C) increase substantially to compensate for the power deficit, resulting in electrical overload on these phases and a disturbance in voltage balance. The most significant mechanical effect is observed in the torque response, shown in Figs (III.13), where the fault generates a negative-sequence current component. This component produces a magnetic field that rotates counter to

the machine's direction, inducing sharp, continuous torque pulsations around a new mean value. Consequently, vibration levels and mechanical stresses on the shaft and drive system are significantly increased.

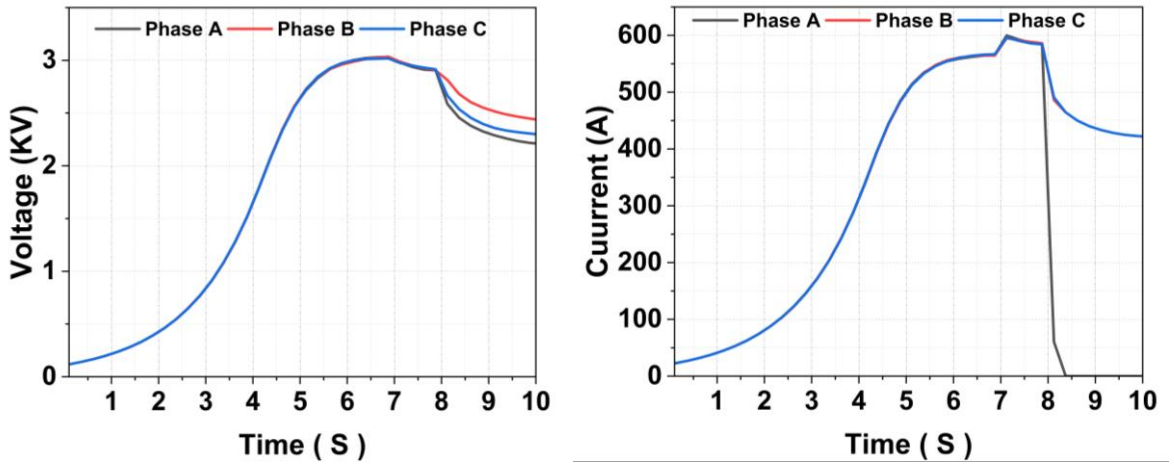

(a) Voltage (b) line current

Fig III.12 RMS Behavior of Generator Voltage and Current under Open-Phase Fault

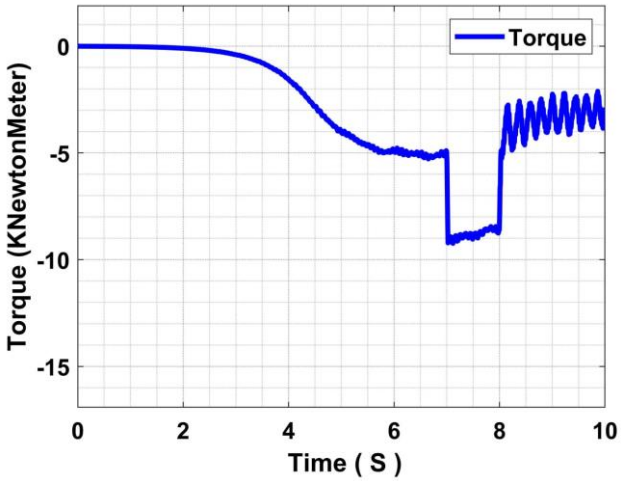

Fig III.13 Transient Torque Behavior of the Generator under Open-Phase Fault

III.2.3.5 Dynamic behavior during progressive capacitor degradation

After determining the appropriate capacitance values both experimentally and analytically, the SEIG achieved healthy operation under no-load and loaded conditions, maintaining terminal voltage close to the rated value. Excitation capacitors used in SEIG systems for

standalone wind energy applications are typically Metallized Polypropylene Film (MPPF) capacitors, available in standard or self-healing designs due to their high reliability, thermal stability, and long operational life. Internally, these capacitors consist of capacitive elements arranged in series and parallel to meet the required voltage and capacitance specifications. The thin metallized dielectric films forming these elements are directly responsible for energy storage and the overall capacitive performance. Fig (III.14) illustrates the excitation capacitor configuration, highlighting the main components and their interconnections [76].

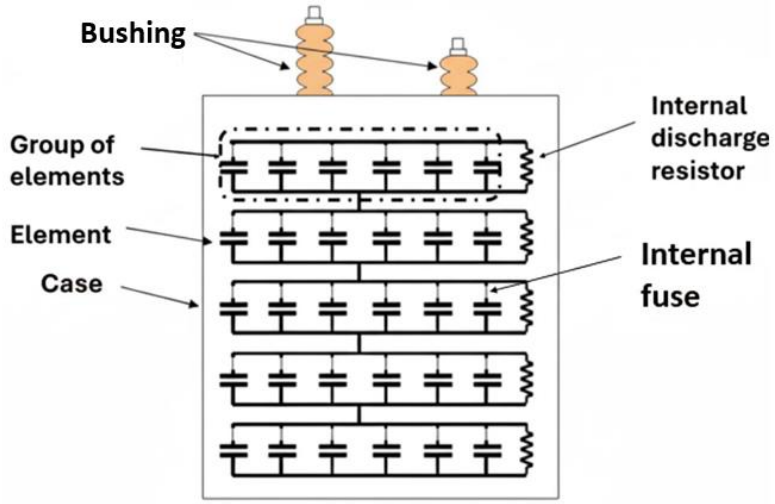

Fig III.14 Schematic Representation of the Excitation Capacitor and Its Internal Components.

This subsection details the excitation capacitor bank configuration used for SEIG self-excitation. The total capacitance was divided into multiple branches to ensure stable operation, with each branch containing four series-connected capacitors sharing 3600 V (nominal voltage × 1.2 safety factor), and twenty-eight branches connected in parallel to provide the required total capacitance. This configuration ensures balanced voltage distribution and safe operation under varying conditions [5].

Progressive degradation was modeled by selectively disconnecting internal elements of a capacitor in phase C, emulating real-world aging caused by thermal cycling, overvoltage, partial discharges, and material deterioration. Six fault conditions were defined, ranging from healthy operation to the staged disconnection of up to five elements, corresponding to ‘soft failures’ from self-healing events. Unlike models based on linear ESR increase, this approach accurately reflects the physical failure mechanism in metallized film capacitors.

The asymmetric reduction in excitation disrupts magnetic field symmetry, producing distortions in the three-phase stator current. TSFEM simulations under identical operating and loading conditions were conducted for each degradation level, with current, voltage, and electromagnetic torque signals recorded to analyze the electrical and electromagnetic impact of these faults [5].

All signal measurements were performed after the system reached a steady-state to ensure accurate and reliable fault diagnosis. Initially, the generator operated under no-load conditions to allow voltage buildup and to eliminate transients associated with startup. After achieving steady-state operation, a balanced resistive load of 10 Ω was applied. The stator current waveforms were then recorded exclusively under these stable operating conditions to prevent the fluctuations that occur during the transient phase, which can significantly affect voltage, current, and torque measurements. Figs (III.15 (a)–(f)) depict the current, voltage, and torque waveforms for both the healthy condition and the scenario with a single failed capacitor, serving as representative examples of the signal patterns. Higher degradation levels, corresponding to two to five failed capacitive elements, were also simulated; however, these results are omitted here for brevity, as they exhibit the same progressive distortion, characterized by increased harmonic content and loss of sinusoidal symmetry.

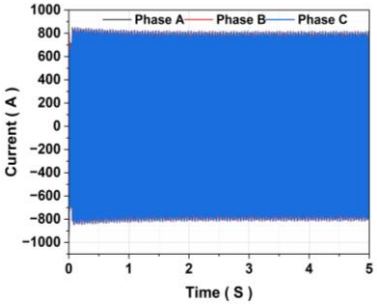

(a) Healthy state

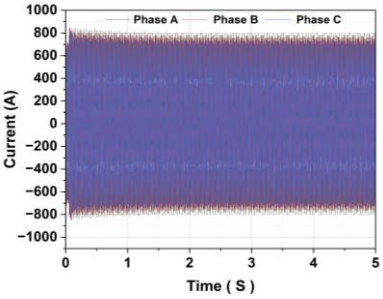

(b) One failed element

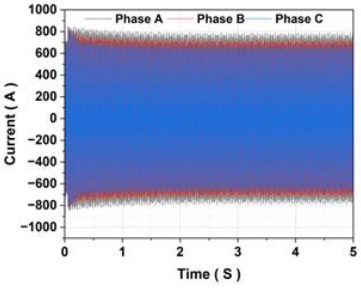

(c) Two elements failed

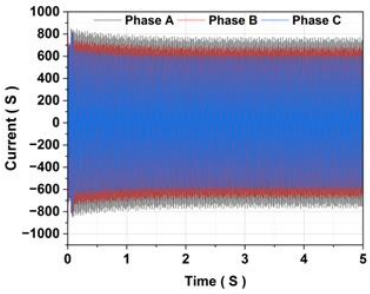

(d) Three elements failed

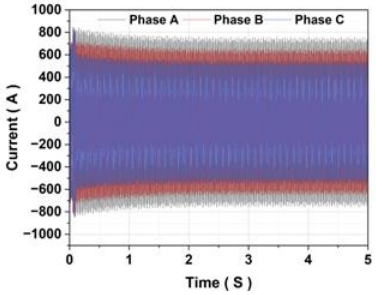

(e) Four elements failed

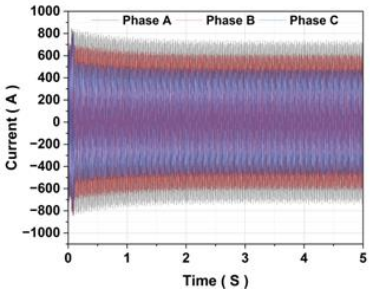

(f) Five elements failed

Fig III.15 Stator current behavior during progressive capacitor element failures

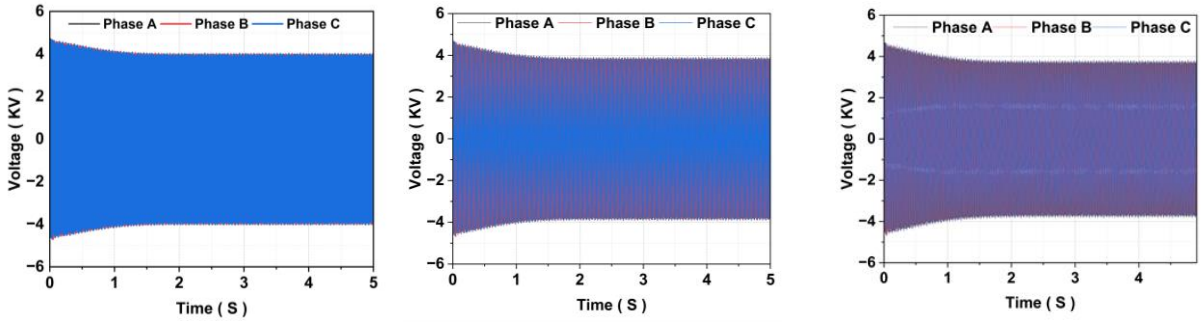

(a) Healthy state (b) One failed element (c) Two elements Failed

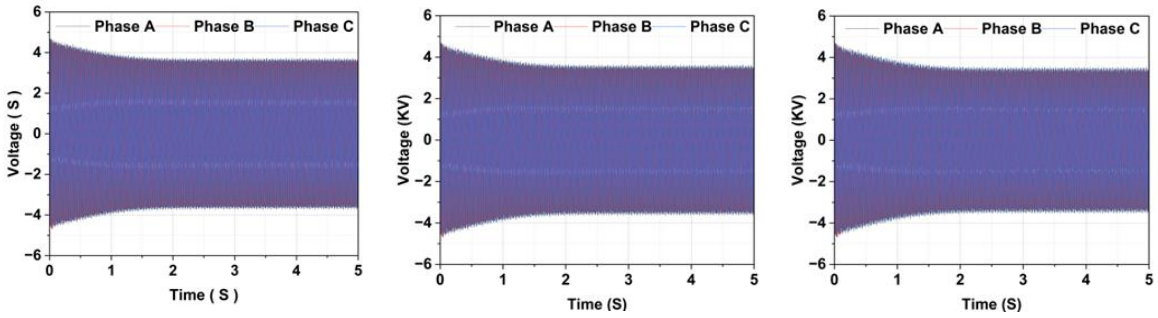

(d) Three elements Failed (e) Four elements failed (f) Five elements failed

Fig III.16 Voltage signal behavior under progressive fault conditions

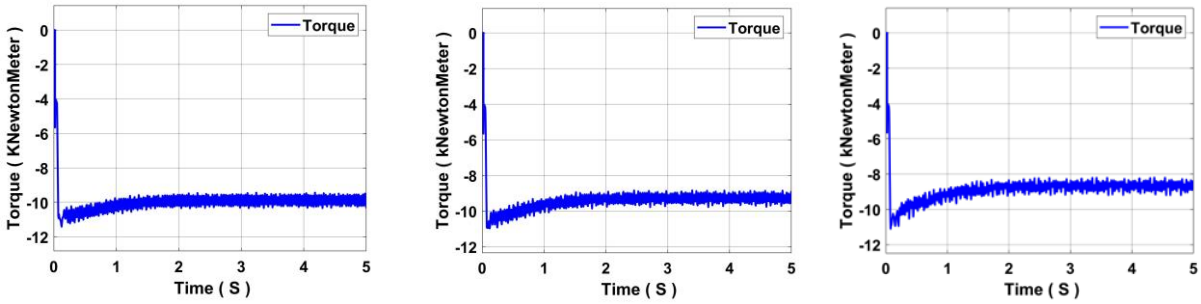

(a) Healthy state (b) One failed element (c) Two elements failed

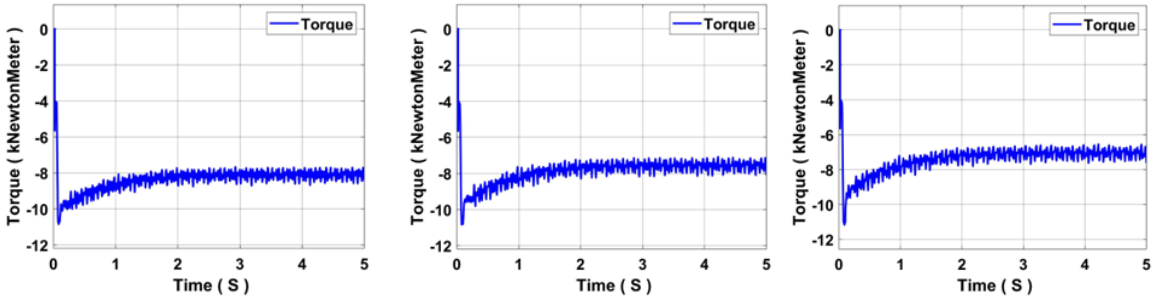

(d) Three elements failed (e) Four elements failed (f) Five elements failed

Fig III.17 Torque behavior under progressive fault conditions

In the current signals illustrated in Figs (III.15 (a)–(f)), minor distortions initially appear in phase C. For the case of a single failed capacitor, these distortions remain largely imperceptible, as the waveform maintains its overall sinusoidal shape. As the fault severity increases, however, the distortions gradually become more evident. The voltage waveforms shown in Figs (III.16(a)–(f)) largely retain a sinusoidal form, but slight variations in peak amplitude and phase balance emerge as degradation progresses. Similarly, the torque profiles depicted in Figs (III.17(a)–(f)) demonstrate gradual deterioration, with torque decreasing from approximately -10 KNM in the healthy generator to around -7 KNM when five capacitive elements fail, indicating a clear decline in dynamic performance. Although some of these deviations are subtle and not easily observed visually, they underscore the necessity of intelligent diagnostic techniques that can identify faults at an early stage.

III.2.3.6 Dynamic behavior during progressive capacitor degradation under variable rotor speed

Given the high sensitivity of SEIG outputs to rotor speed and mechanical excitation, the model was tested under variable operating conditions, with the rotor speed carefully maintained between 3120 rpm and 3150 rpm. This narrow range, slightly above the synchronous speed of 3110 rpm, creates a low-slip environment that adds a rigorous test of the model's performance. The adopted speed profile is shown in Fig III.18.

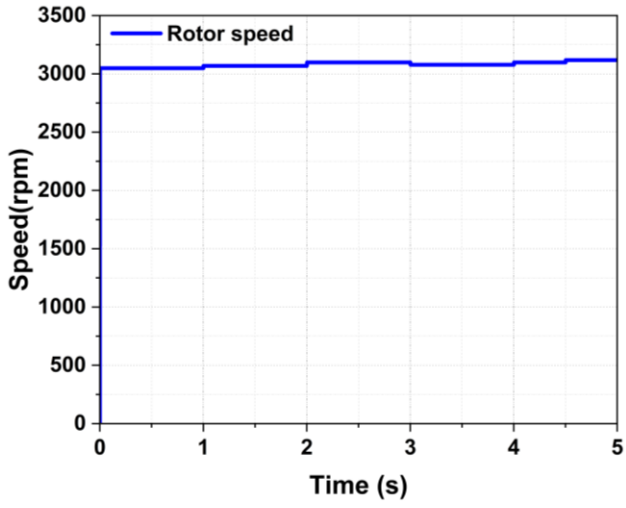

Fig III.18 Rotor speed profile

The current waveform recorded during varying rotor speeds and simultaneous gradual capacitor degradation is illustrated in Fig III.19.

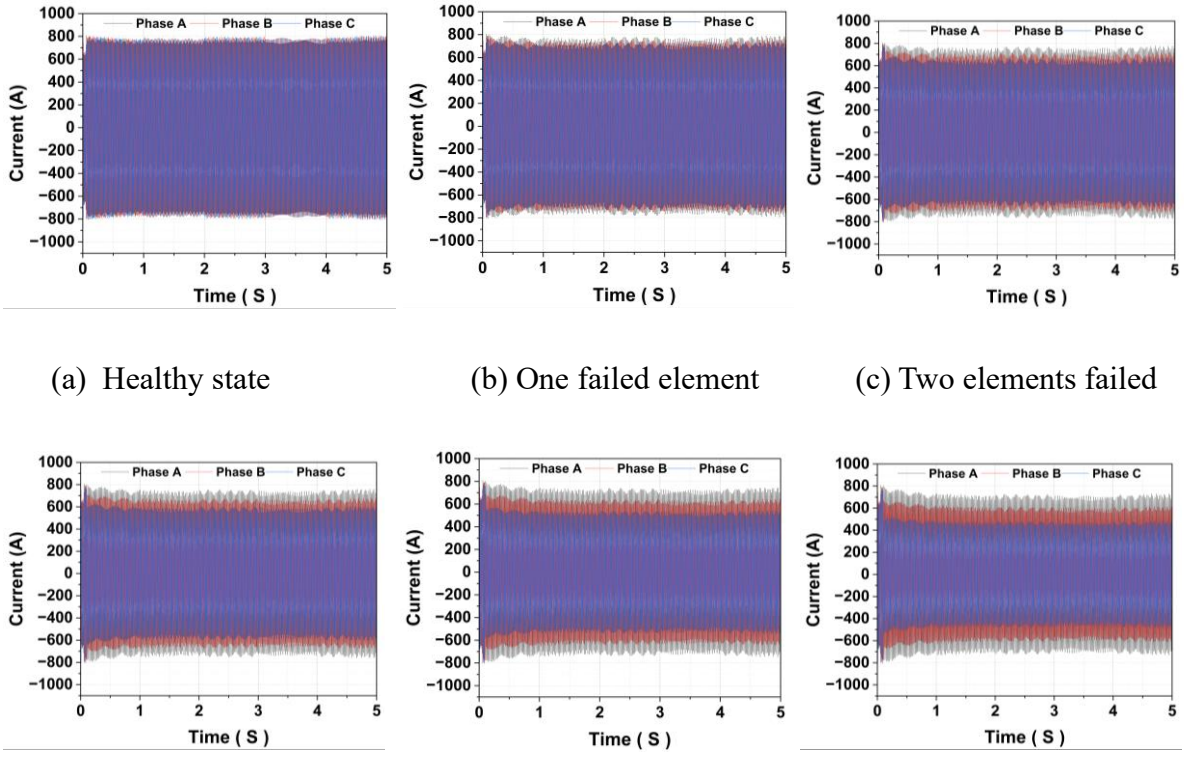

(a) Healthy state (b) One failed element (c) Two elements failed

(d) Three elements failed (e) Four elements failed (f) Five elements failed

Fig III.19 Stator current response to progressive internal capacitor failures under variable rotor speeds.

Fig III.20 illustrates the measured voltage signal under the same variable speed conditions used for testing, alongside the progressive degradation of internal capacitive elements.

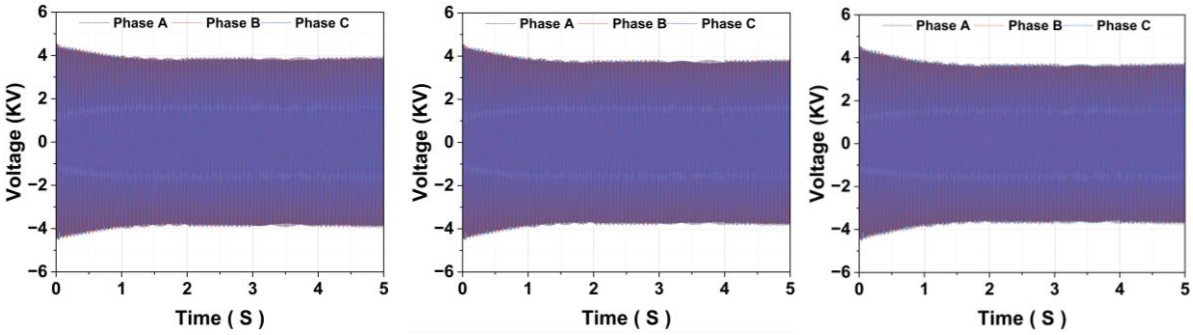

(a) Healthy state (b) One failed element (c) Two elements Failed

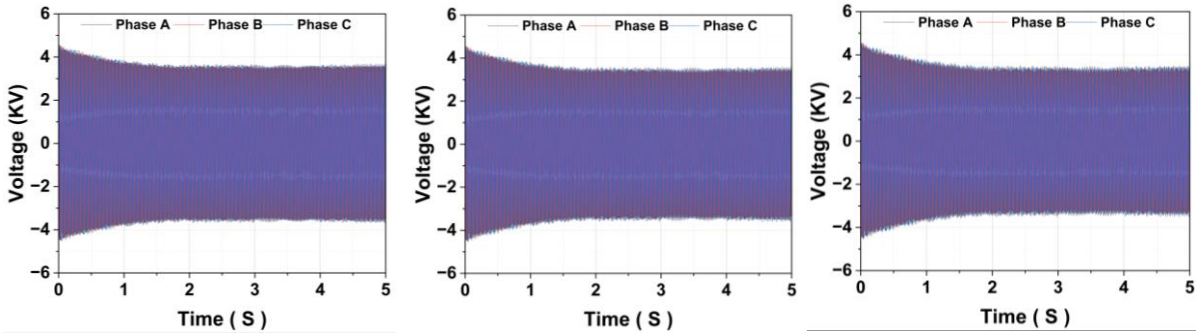

(d) Three elements Failed (e) Four elements failed (f) Five elements failed

Fig III.20 Voltage response to progressive internal capacitor failures under variable rotor speeds

Figure III.21 presents the measured electromagnetic torque under variable rotor speed conditions combined with the progressive degradation of internal capacitive elements.

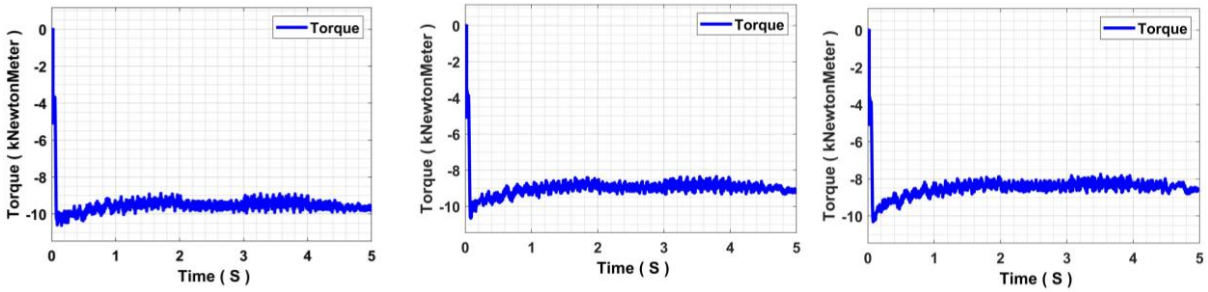

(a) Healthy state (b) One failed element (c) Two elements failed

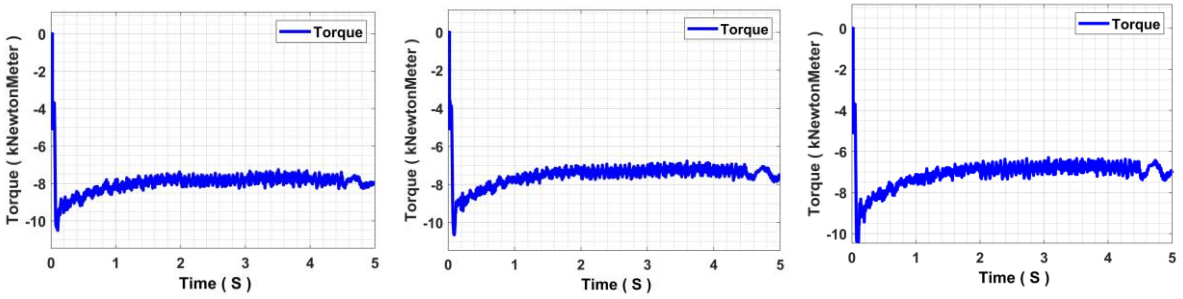

(d) Three elements failed (e) Four elements failed (f) Five elements failed

Fig III.21 Torque under progressive capacitor faults and variable rotor speeds

Analysis of the signals under varying rotor speed conditions revealed a noticeable intensification of faults compared to steady-state operation. Voltage signals showed pronounced distortions, while current waveforms exhibited sharp and distinct fluctuations. The

torque signal was most affected, displaying substantial dynamic degradation, which highlights the high sensitivity of the SEIG to simultaneous variations in capacitive excitation and rotor speed.

III.2.3.7 Dynamic behavior during broken bars fault

In this phase, the diagnosis and detection of broken rotor bar defects in the SEIG under load conditions are investigated by considering different numbers of broken bars. The TSFEM is employed to extract stator current, terminal voltage, and electromagnetic torque signals. The study is conducted through six distinct scenarios. Initially, signals are obtained under healthy operating conditions while accounting for the load. Subsequently, fault conditions are introduced progressively, corresponding to one, two, three, four, and five broken rotor bars. The extracted signals for all cases are presented in Figs (22-24).

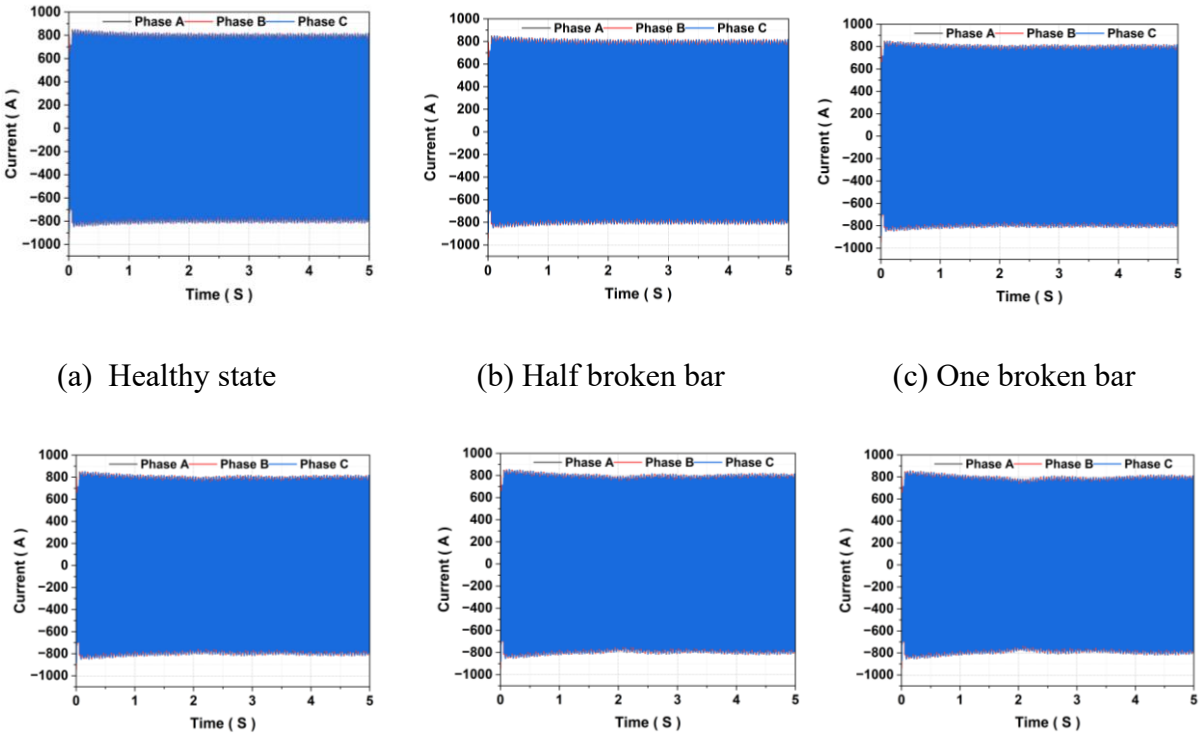

(a) Healthy state (b) Half broken bar (c) One broken bar

(d) Two broken bars (e) Three broken bars (f) For broken bars

Fig III.22 Stator current behavior during broken bars fault conditions

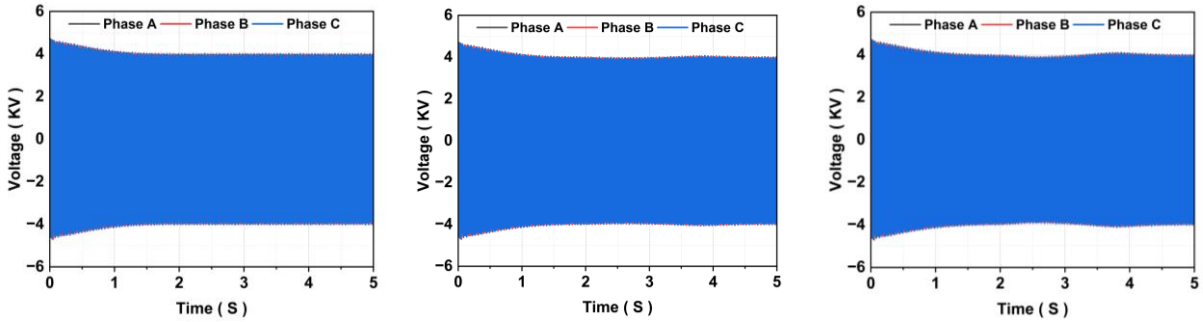

(a) Healthy state (b) Half broken bar (c) One broken bar

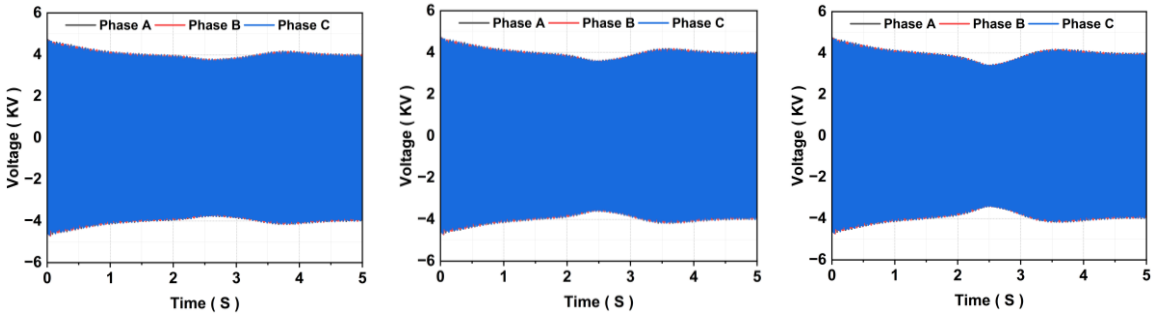

(d) Two broken bars (e) Three broken bars (f) Four broken bars

Fig III.23 Voltage signal behavior under broken bars fault conditions

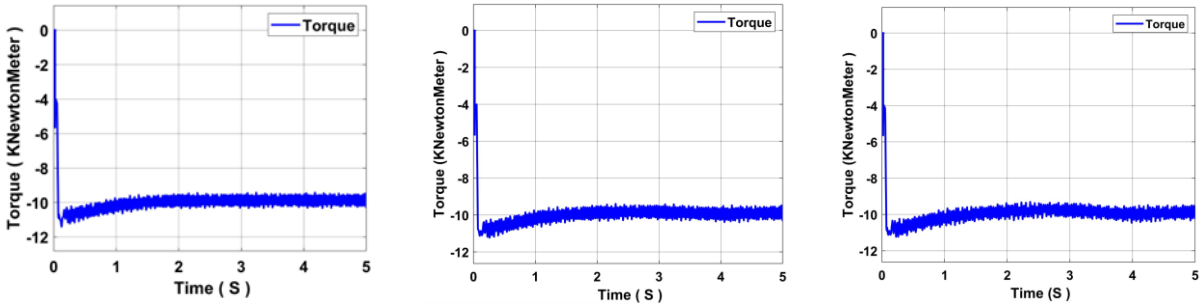

(a) Healthy state (b) Half broken bar (c) One broken bar

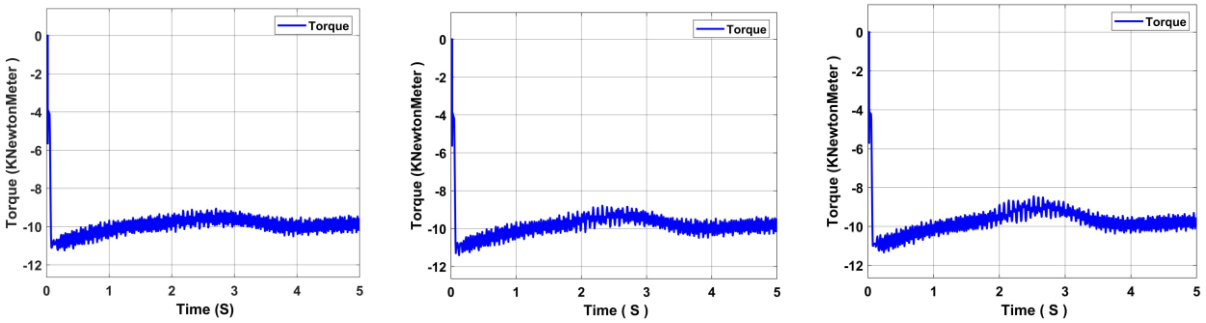

(d) Two broken bars (e) Three broken bars (f) Four broken bars

Fig III.24 Torque behavior under broken bars fault conditions

The current waveforms presented in Figs. III.22(a)–(f) reveal a clear degradation in signal quality as the number of broken rotor bars increases. Under healthy conditions, the current remains nearly sinusoidal; however, the introduction of faults leads to progressively pronounced distortions, indicating increased harmonic content and electromagnetic asymmetry. This behavior is directly associated with rotor imbalance and the appearance of fault-related frequency components.

Similarly, the voltage profiles shown in Figs. III.23(a)–(f) exhibit a noticeable reduction in amplitude with increasing fault severity. Quantitatively, the terminal voltage drops to approximately 2.121 kV (RMS) at higher levels of rotor damage, reflecting a decline in the generator's excitation capability and energy conversion efficiency. This voltage degradation highlights the sensitivity of the SEIG performance to rotor bar integrity under load conditions.

Furthermore, the electromagnetic torque responses illustrated in Figs. III.24(a)–(f) demonstrate increasing instability as the number of broken bars rises. In particular, significant torque oscillations are observed, with a fluctuation of approximately 1.8 kN·m, which is associated with characteristic fault-related frequency components at $(1\pm2s)$ fs under severe fault conditions. These components arise due to rotor asymmetry and are indicative of broken bar faults. The resulting oscillations reflect a loss of steady-state stability and increased mechanical stress, which may accelerate system wear and reduce the operational lifespan of the machine.

III.3 conclusion

Chapter III presents the numerical simulation results of the SEIG system based on the FEM. First, the FEM-based model of the SEIG is introduced, along with the fault simulation procedure and the adopted experimental setup. Subsequently, the simulation results are analyzed, with particular emphasis on fault visualization and system behavior under various operating conditions.

The study investigates the dynamic response of the SEIG during no-load start-up as well as under loaded operating conditions in order to assess the electrical and mechanical performance and stability of the system. Furthermore, the effects of unbalanced RL load faults,

open-phase faults, excitation capacitor degradation, and broken rotor bars are examined, highlighting their impact on currents, voltages, and power characteristics. These analyses provide a comprehensive understanding of the influence of different fault scenarios on the performance of the self-excited induction generator.

Finally, the next chapter focuses on the diagnosis of excitation capacitor degradation and broken rotor bar faults using machine learning and deep learning techniques, aiming to develop an intelligent and reliable fault diagnosis framework for SEIG-based wind energy systems.

IV. Chapter 04: Intelligent Fault Detection

IV.1 Introduction

The increasing complexity of modern wind energy systems and the critical role of excitation capacitors in SEIGs underscore the importance of employing advanced data-driven approaches, such as ML and DL, for reliable fault diagnosis. While traditional signal processing techniques are effective for basic fault detection, they often lack the adaptability and robustness required to identify subtle or aging-related faults under varying operating conditions [5].

This chapter presents a comprehensive methodology for diagnosing excitation capacitor degradation in SEIGs using both classical machine learning algorithms and deep learning models. Specifically, Random Forest (RF), Support Vector Machine (SVM), k-Nearest Neighbors (KNN), and Naïve Bayes (NB) classifiers are applied to extract and learn relevant patterns from processed signal features. Additionally, a 2D Convolutional Neural Network (CNN) is constructed to automatically learn hierarchical representations directly from the signals, enabling enhanced diagnostic accuracy and robustness. The chapter details the feature extraction process, model development, training and validation procedures, performance evaluation, and a comparative analysis of the applied techniques, demonstrating the effectiveness of data-driven approaches in improving fault detection for SEIG excitation systems.

IV.2 Machine Learning Feature Extraction

Each signal phase currents (A, B, C), phase voltages (A, B, C), and shaft torque—was segmented into non-overlapping windows of length N=256. From each channel, 18 features were extracted, yielding a total of 7 channels × 18 features = 126 features per segment.

Time-domain features included Zero-Crossing Rate (ZCR), RMS, Standard Deviation (STD), Mean, Energy, Peak-to-Peak (PTP) amplitude, and Crest Factor, which quantify signal amplitude, variability, and waveform shape. Statistical descriptors such as Kurtosis and Skewness were employed to characterize higher-order moments of the signal distribution. Frequency-domain features were derived via FFT, including spectral centroid, spectral entropy,

spectral flatness, and band power, capturing the signal's frequency content and energy distribution. Temporal complexity was further quantified using Hjorth parameters: activity $A = var(x)$ representing signal power, mobility $M = \frac{\sigma(x')}{\sigma(x)}$ indicating the mean frequency, and complexity $C = \frac{\sigma(x'')}{\sigma(x')} \div M$ reflecting the rate of frequency variation, where x, x', and x'' denote the signal and its first and second derivatives, respectively. Finally, autocorrelation coefficients at lags 1 and 2 were included to capture short-term temporal dependencies. Collectively, these features provide a robust representation of the signal characteristics under different fault conditions [5].

IV.3 ML-Based Fault Classification

In the SVM formulation, α_i represent the learned coefficients of the support vectors, $\mathcal{Y}_i$are the class labels associated with each support vector, X_i denote the support vectors, γ is the RBF kernel parameter controlling the spread, X is the input feature vector, and b is the bias term. In this study, the SVM was configured with a Box Constraint C=10 and an automatically determined Kernel Scale γ, with all input features standardized. This configuration enables robust generalization, particularly when class boundaries are nonlinear or complex [5]. The k-Nearest Neighbors (KNN) classifier assigns the class label of a test instance based on the majority vote of its K=3 nearest neighbors, using Euclidean distance with equal weighting, as expressed in equation (VI.1). The choice of K=3 serves as a standard baseline for multi-class classification, offering a balance between sensitivity to local patterns and resilience to noise [5].

$$\hat{\mathcal{Y}} = mode(\mathcal{Y}(1), \mathcal{Y}(2), \ldots . \mathcal{Y}(k)) \quad \text{(IV.1)}$$

In the KNN framework, $\hat{\mathcal{Y}}$ denotes the class label of the iii-th nearest neighbor to a test sample, and the function *mode (.)* identifies the most frequently occurring label among the *K* neighbors. While KNN is intuitive and straightforward to implement, its classification performance is sensitive to the underlying data distribution and can be computationally demanding for large datasets due to the necessity of calculating distances to all training points [5].

RF is an ensemble learning algorithm that employs Bootstrap Aggregation (Bagging) of decision trees. Each tree is trained on a randomly sampled subset of the training data and a

randomly selected subset of features. In this study, RF was configured with 300 trees and a maximum of 20 splits per tree. The final prediction is obtained by aggregating the outputs of all M individual trees through majority voting, as expressed in the following equation [5]:

$$\hat{\mathcal{Y}} = mode(T_1(X), T_2(X), \ldots, T_M(X)) \quad \text{(IV.2)}$$

In the RF model, $T_M(X)$ denotes the prediction of the *M*-th decision tree for the input feature vector *X*, and the function *mode(.)* selects the most frequently predicted class. This ensemble approach enhances model stability, mitigates overfitting, and improves generalization across all classes [5].

NB is a generative probabilistic classifier that assumes conditional independence among features given the class label. The posterior probability of a class $\mathcal{Y}$ for a feature vector $X = (x_1, x_2, \ldots, x_n)$ is computed using Bayes' theorem, as expressed in the following equation [5]:

$$P(\mathcal{Y}|X) = \frac{P(\mathcal{Y})\Pi_{j=1}^{n} P(x_j|\mathcal{Y})}{P(X)} \quad \text{(IV.3)}$$

In this formulation, $P(\mathcal{Y})$ represents the prior probability of class $\mathcal{Y}$, $P(x_i|\mathcal{Y})$ is the likelihood of observing feature x_i given class $\mathcal{Y}$, and $P(X)$ serves as the evidence or normalization factor. For Gaussian NB, the likelihood $P(x_i|\mathcal{Y})$ is modeled as a Gaussian distribution, parameterized by the class-specific mean and variance of each feature. Despite the strong independence assumption, NB achieved competitive performance while providing extremely fast training and prediction times. The dataset was partitioned using a 70/30 Hold-Out validation scheme, with 70% of the samples allocated for training and 30% for testing.

IV.4 DL-Based Fault Classification of SEIG Using CNN

To enable efficient and accurate fault classification in resource-constrained environments, a CNN was developed and trained on RGB images derived from synchronized current, voltage, and torque signals using the Continuous Wavelet Transform (CWT). The CWT provides a time-frequency representation of the signals, with coefficients computed using the Morlet wavelet, as expressed in the following equation [5]:

$$W_x(a,b) = \frac{1}{\sqrt{a}} \int_{-\infty}^{\infty} x(t)\psi^*\left(\frac{t-b}{a}\right)dt \quad \text{(IV.4)}$$

In this formulation, ψ denotes the Morlet wavelet, while $x(t)$represents the original time-domain signal, such as current, voltage, or torque. The term $W_x(a,b)$ corresponds to the continuous wavelet transform coefficients, where the scale parameter a governs the wavelet dilation and, consequently, the frequency resolution, and the translation parameter b determines the temporal shift of the wavelet to analyze localized signal characteristics. The obtained scalograms were subjected to a logarithmic transformation and subsequently merged into RGB images with a resolution of 128×128×3, which were used as inputs to the convolutional neural network. The developed CNN follows an end-to-end architecture that processes CWT-based representations of raw SEIG signals and performs automatic feature learning for fault classification, eliminating the need for manually engineered features [5].

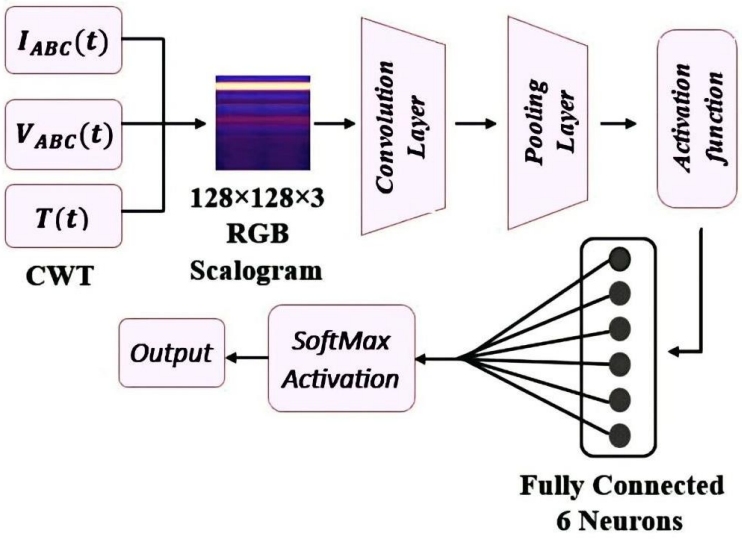

Figure IV.1 CNN structure.

The constructed dataset contains a total of 7,116 images generated from partially overlapping signal windows, each consisting of 256 samples. For every capacitor operating condition—namely the healthy state and five distinct fault scenarios 5,001 signal samples were segmented, yielding 1,186 images per category. This procedure resulted in a balanced six-class classification dataset. The data were divided using a stratified approach, with 70% allocated for training and 30% for testing, corresponding to 4,981 training images (831 per class) and 2,135 testing images (355 per class). The CNN architecture, depicted in Figure 6, is composed of three two-dimensional convolutional layers with progressively increasing numbers of filters (16, 32, and 64). Each convolutional layer employs a kernel size of 3×3 and uses the ReLU activation function. To enhance training stability and convergence, batch normalization is applied after every convolutional operation, followed by 2×2 max-pooling layers to

downsample the spatial dimensions of the feature maps. The output of the l-th convolutional layer is given by [5]:

$$Z(l) = W(l) * X(l) + b(l) \quad \text{(IV.5)}$$

Where $Z(l)$ represents the resulting feature map, $W(l)$ denotes the convolutional filter weights, $X(l)$ is the input feature map, $b(l)$ corresponds to the bias term. The operator * indicates the convolution process [5].

Following the convolution and pooling stages, the extracted feature maps are flattened into a one-dimensional vector and fed into one or more fully connected (FC) layers. These layers capture high-level abstractions through linear transformations expressed as [5]:

$$F(l) = W_f(l).X(l) + b_f(l) \quad \text{(IV.6)}$$

Where $F(l)$ denotes the FC layer output, $W_f(l)$ and $b_f(l)$ are the associated weights and biases, and $X(l)$ is the flattened input vector.

For multi-class discrimination, the final FC layer is followed by a Softmax activation function that converts the network outputs into normalized class probabilities, defined as [5]:

$$\widehat{y_i} = \frac{e^{Z_i}}{\sum_{i=1}^{C} e^{Z_i}} \qquad for\ i = 1, \dots, C \quad \text{(IV.7)}$$

Where $\widehat{y_i}$ represents the predicted probability of class i, and Z_i is the corresponding input score. The class associated with the highest probability is selected as the predicted label.

The network was trained using the Adam optimization algorithm with a mini-batch size of 32 for up to 50 epochs. To mitigate overfitting, early stopping was implemented based on the validation loss. Instead of adopting a highly complex deep learning structure, a compact CNN architecture was intentionally chosen to suit the dataset's moderate size and complexity. This design choice effectively reduced computational requirements and overfitting risk while preserving strong classification performance. The obtained results confirm the adequacy of the lightweight architecture, indicating that additional model complexity is not required at this stage [5].

IV.5 Performance comparison of fault diagnosis classifiers

The performance of the classification models was assessed using multiple quantitative metrics. Overall accuracy served as a global measure of correct predictions, while class-specific precision, recall, and F1-score were computed to provide a more detailed evaluation of each model's performance. Precision is defined as $Precision = \frac{TP}{TP+FP}$, recall as $Recall = \frac{TP}{TP+FN}$, and F1-score as $F1 - score = \frac{2.Precision.Recall}{Precision+Recall}$, where TP, FP, and FN denote the numbers of true positives, false positives, and false negatives, respectively. Normalized confusion matrices were also used to visualize prediction accuracy for each class. Additionally, ROC curves were generated using a one-vs-rest approach, with the area under the curve (AUC) serving as a measure of class separability. Computational efficiency was evaluated by recording both training and prediction times. To ensure the robustness of the results, each model was tested across 10 repeated random hold-out splits using a 70/30 ratio. Figure (IV.2) and Table (IV-1) summarize the classification accuracy, training time, and prediction time, with Table (IV-1) also reporting the mean accuracy and standard deviation over all splits.

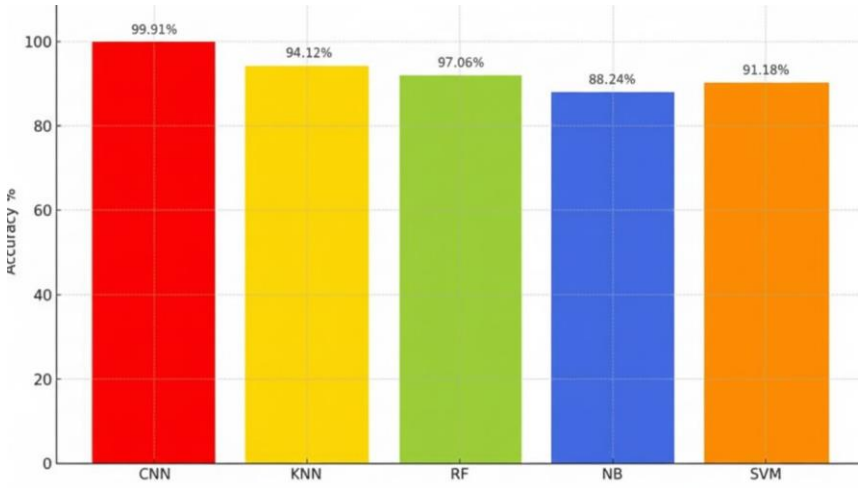

Figure IV.2 Evaluation of classifier accuracy across models

Table IV-1 Class-wise performance of each classifier

Model	Prediction time (s)	Training time (s)	Accuracy (%)	Mean Accuracy (%)	STD (%)
RF	0.71	4.7	97.06	96.80	0.85
KNN	0.11	0.37	94.12	93.90	1.10
SVM	0.05	0.4	91.18	90.95	1.50
CNN	13.38	557.09	99.91	99.80	0.15
NB	0.0830	0.3046	88.24	88	1.90

As shown in Fig (IV.2) and Table IV-1, the lightweight CNN achieved the highest classification accuracy of 99.91%, with a mean accuracy of 99.80% and a low standard deviation of 0.15%, indicating highly consistent performance across repeated hold-out splits. However, this high accuracy came at the cost of the longest training (557.09 s) and prediction (13.38 s) times, reflecting a substantial computational demand. The RF model followed, attaining 97.06% accuracy, a mean accuracy of 96.80%, and a standard deviation of 0.85%, while requiring moderate training (4.7 s) and prediction (0.71 s) times, benefiting from its ensemble learning approach. The KNN algorithm achieved 94.12% accuracy (mean 93.90%, STD 1.10%) with very short training time (0.37 s), although its prediction time was 0.11 s due to its instance-based computation. The SVM reached 91.18% accuracy, with a mean of 90.95% and STD of 1.50%, while maintaining efficient training (0.4 s) and prediction (0.05 s) performance. The NB classifier showed the lowest accuracy (88.24%) with a mean of 88% and STD of 1.90%, but it demonstrated the fastest training (0.3046 s) and prediction (0.0830 s) times.

To evaluate each model's classification capability across different fault types, confusion matrices were generated from experimental results (Figures IV.3 (a)–(e)). These matrices show

the distribution of predictions across the fault classes and provide detailed insight into diagnostic accuracy. In particular, the CNN confusion matrix (Figure IV.7(d)) highlights the model's superior performance across all classes (F0–F5). These findings emphasize the CNN's excellent generalization ability and its capacity to extract highly discriminative features from time-domain signals, even when distinguishing between closely related fault conditions.

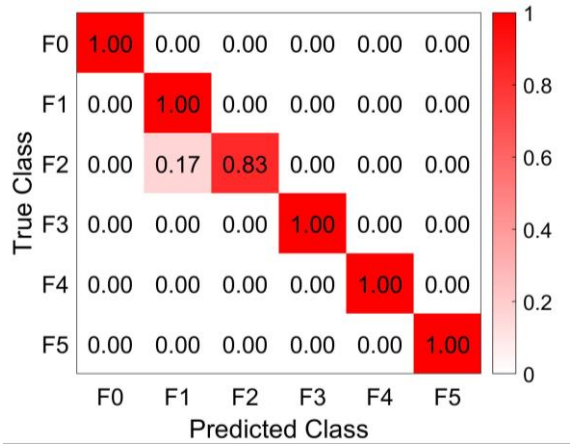

(a) RF Confusion matrices

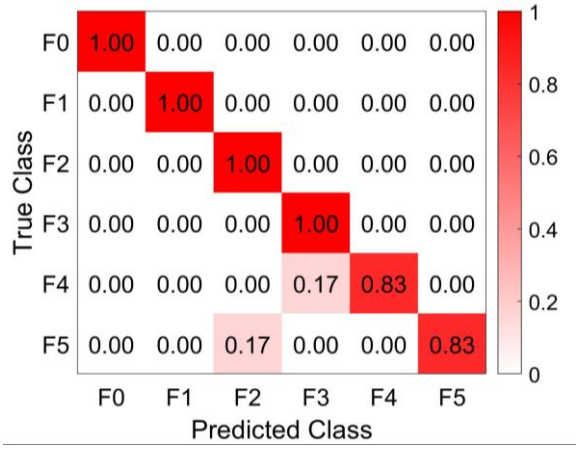

(b) KNN Confusion matrices

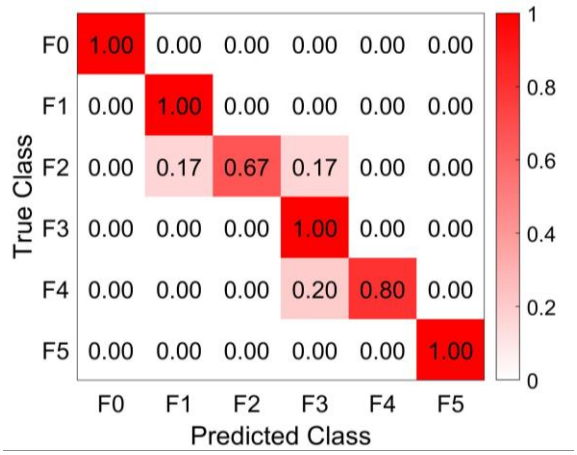

(c) SVM Confusion matrices

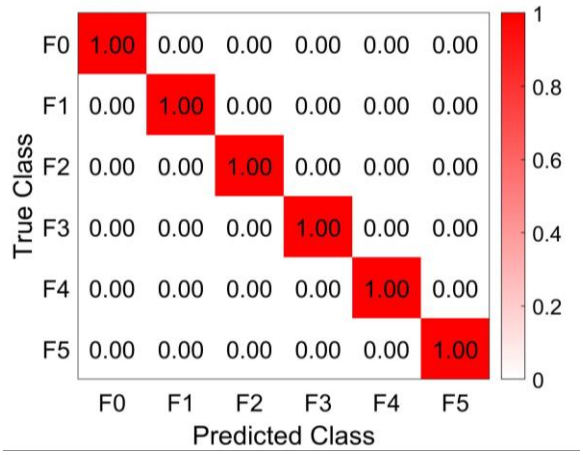

(d) CNN Confusion matrices

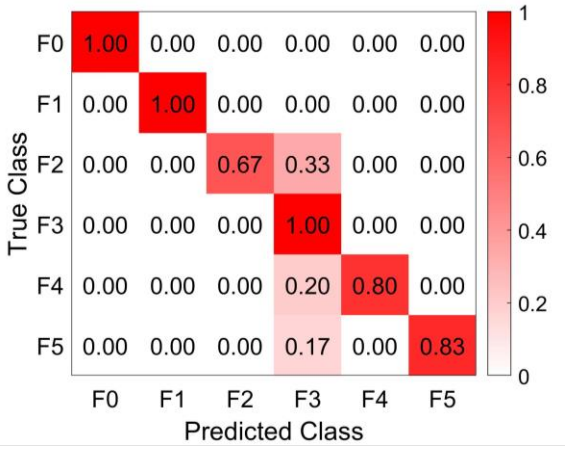

(e) NB Confusion matrices

Fig IV.3 Confusion matrices of the evaluated classifiers

In comparison, the RF model illustrated in Figure IV.3(a) also delivered strong overall performance, achieving 100% accuracy in most fault categories. However, it showed significant confusion between F2 and F1, with 17% of F2 samples incorrectly classified as F1. This misclassification is likely due to the similarity in statistical features extracted from these two classes, which makes it challenging for the model to establish distinct decision boundaries.

The KNN classifier, presented in Figure IV.3(b), generally achieved high accuracy, correctly identifying most classes. Nevertheless, it exhibited confusion between F4 and F3, and a portion of F5 samples were misclassified as F2. These errors indicate overlapping feature distributions within these fault categories.

The SVM model, shown in Figure IV.3(c), displayed moderate performance, correctly classifying only 67% of F2 samples, with the remainder misclassified as F1 and F3. This outcome is attributable to the SVM's reliance on well-separated margins between classes. In this scenario, the extracted features may not be linearly separable in the transformed feature space, limiting the model's ability to construct effective hyperplanes. Consequently, SVM struggles to differentiate closely spaced or overlapping fault patterns such as F1, F2, and F3.

Finally, NB classifier, shown in Figure IV.3(e), correctly classified classes F0, F1, and F3. However, its performance declined for classes F2, F4, and F5, primarily due to the strong assumption of feature independence, which is unlikely to hold in this context where complex signal interactions exist. Consequently, NB is limited in modeling correlated or nonlinear features.

Tables (IV.2–IV.8) provide a detailed evaluation of each model's classification performance using precision, recall, and F1-score metrics across all fault categories. These class-wise metrics offer more granular insight into model behavior beyond overall accuracy. For example, the RF classifier (Table IV.2) achieved consistently strong results, with perfect precision and recall for most classes. Minor confusion between F3 and F4 led to an F1-score of 0.91, suggesting some overlap in the extracted feature space.

The KNN classifier (Table IV.3) also demonstrated high reliability, achieving flawless classification for healthy, F1, and F3 classes. A slight reduction in recall (0.83) was observed for F5, yet all F1-scores remained above 0.90, reflecting robust overall performance. In contrast, the SVM model (Table IV.4) showed lower separability between classes, particularly for F2 and F3. It recorded a reduced recall of 0.67 for F2 and exhibited confusion among overlapping classes, resulting in an F1-score of 0.80.

The CNN (Table IV.5) outperformed all other classifiers, achieving F1-scores above 0.99 for every class, with a micro-average of 0.997. This confirms its superior capability to extract discriminative features and maintain generalization, even under complex and closely related fault conditions. Conversely, the NB classifier (Table IV.6) struggled with overlapping fault categories. While it performed perfectly for healthy and F1 classes, it exhibited substantial drops for F2 and F3, with a precision of only 0.56 for F3, ultimately leading to the lowest overall performance among the evaluated models.

Table IV-2 RF Performance

Class	Precision	Recall	F1_Score
F0	1	1	1
F1	0.85714	1	0.92308
F2	1	0.83333	0.90909
F3	1	1	1

F4	1	1	1
F5	1	1	1
Micro Average	0.976	0.972	0.972

Table IV-3 KNN Performance

Class	**Precision**	**Recall**	**F1_Score**
F0	1	1	1
F1	1	1	1
F2	0.83333	1	0.90909
F3	0.85714	1	0.92308
F4	1	0.83333	0.90909
F5	1	0.83333	0.90909
Micro Average	0.948	0.944	0.942

Table IV-4 SVM Performance

Class	**Precision**	**Recall**	**F1_Score**
F0	1	1	1

F1	0.85714	1	0.92308
F2	1	0.66667	0.8
F3	0.75	1	0.85714
F4	1	0.8	0.88889
F5	1	1	1
Micro Average	0.934	0.911	0.912

Table IV-5 CNN Performance

Class	**Precision**	**Recall**	**F1_Score**
F0	1	1	1
F1	1	0.99719	0.99859
F2	0.9943	1	0.99714
F3	1	0.99719	0.99859
F4	1	1	1
F5	1	1	1
Micro Average	0.999	0.999	0.999

Table IV-6 NB Performance

Class	Precision	Recall	F1_Score
F0	1	1	1
F1	1	1	1
F2	1	0.66667	0.8
F3	0.55556	0.83333	0.71429
F4	1	0.8	0.88889
F5	1	0.83333	0.90909
Micro Average	0.926	0.856	0.885

To further evaluate the models' generalization capability in distinguishing between fault categories, Receiver Operating Characteristic (ROC) curves were generated for each classifier, as illustrated in Figs IV.4(a)–(f). These curves were obtained using a one-vs-all approach on the test dataset, providing a detailed assessment of each model's class-specific discrimination performance. The RF classifier (Figure IV.4(a)) achieved high AUC values across most fault classes, with a minor reduction observed for F2 (AUC = 0.89). Similarly, the KNN model (Figure IV.4(b)) demonstrated strong discriminative ability, although its performance for F5 was slightly lower, with an AUC of 0.91.

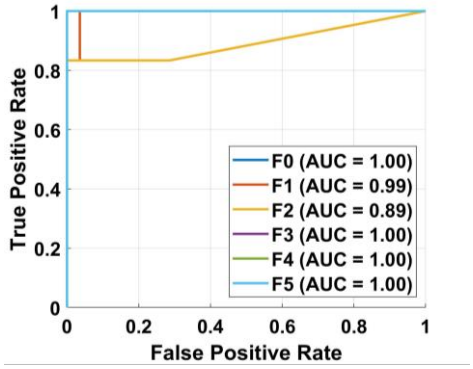

(a) RF

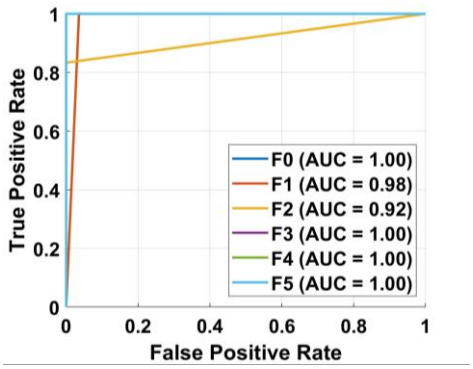

(b) KNN

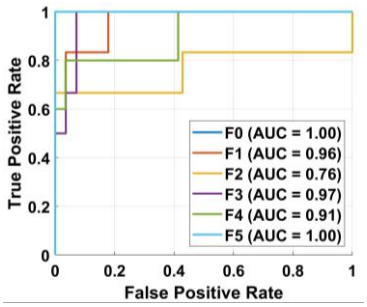

(c) SVM

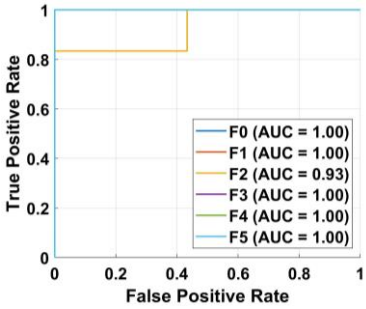

(d) CNN

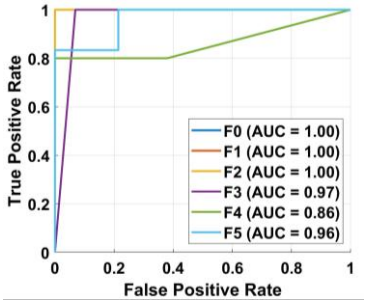

(e) NB

Fig IV.4 Class-wise ROC analysis for each model

As illustrated in Fig IV.4(c), the SVM classifier exhibited inconsistent performance, particularly for class F2 (AUC = 0.76), indicating sensitivity to overlapping feature distributions. In contrast, the CNN model (Fig IV.4(d)) demonstrated exceptional generalization, achieving near-perfect AUC values (≥ 0.94) across all classes. The NB classifier (Fig IV.4(e) delivered reasonable results overall; however, its performance for F4 dropped to 0.86, likely due to its assumption of feature independence. These observations suggest that CNN and RF are the most reliable classifiers for this application, providing high AUC values and robust generalization across fault categories. While CNN offers superior classification accuracy, RF provides a favorable balance between performance and computational efficiency. The KNN model is effective for fault classes that are clearly separable, whereas SVM and NB are more prone to performance degradation when classes overlap or exhibit complex patterns. This emphasizes the importance of selecting a classifier that matches both the characteristics of the data and practical deployment requirements.

IV.5.1 Robustness analysis of the CNN model under variable conditions

This section investigates the robustness and generalization capability of the CNN model on previously unseen datasets, such as signals obtained under capacitor degradation faults at variable speeds. Such a setup enables the CNN to discriminate even subtle speed variations, demonstrating its robustness under highly sensitive dynamic conditions.

The dynamic dataset presents a significant challenge to the CNN model's robustness, as accurate fault diagnosis requires the model to extract essential fault features while filtering out variability induced by changing operating conditions.

Table IV.7 summarizes the CNN model's performance on this dataset with variable rotor speeds. Despite the increased complexity and signal variability, metrics such as accuracy, F1-score, and recall demonstrate that the model maintains a high level of diagnostic reliability under these challenging conditions.

Table IV-7 CNN performance

Class	Precision	Recall	F1_Score
F0	1	0.99719	0.99859
F1	0.98867	1	0.9943
F2	0.9944	0.99719	0.99719
F3	1	0.98876	0.99435
F4	0.99719	0.99719	0.99719
F5	1	1	1
Micro Average	0.9967	0.9967	0.9969

To provide a more comprehensive evaluation, the corresponding confusion matrix offers a detailed view of the model's capability to distinguish between different fault categories and the

healthy state, confirming the effectiveness of its feature extraction under dynamic operating conditions.

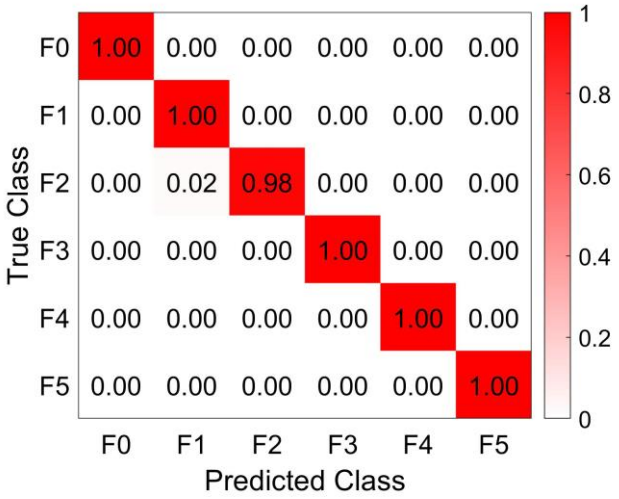

Figure IV.5 Confusion matrices illustrating CNN performance

The CNN model's superior diagnostic reliability is critical for the robust and safe operation of SEIGs in microgrid applications, despite the associated computational overhead (prediction time: 14.58 s versus 0.7 s for RF). While the RF model offers faster inference, its lower mean accuracy (96.80 %) and comparatively higher variability (STD = 0.85 %) make it less suitable for safety-critical applications. In contrast, the CNN achieves near-perfect performance on the training data, with a mean accuracy of 99.80 %, an overall accuracy of 99.91 %, and exceptional stability (STD = 0.15 %). The model's robustness is further validated on the dynamic test dataset including varying rotor speed conditions where it maintained an impressive accuracy of 99.67 %, demonstrating strong generalization and durability under challenging operating scenarios.

For high-voltage SEIG fault diagnosis, this level of robustness justifies the additional computational cost. The corresponding confusion matrix highlights the model's exceptional class discrimination, with the diagonal entries for all fault classes (F0–F5) near unity, and only a minor misclassification in F2 (0.02 %). These results are reinforced by precision, recall, and F1-score metrics, most ranging from 0.9943 to 1.00, confirming the CNN's ability to extract fundamental fault features while decoupling them from variations induced by rotor speed changes. Therefore, the considerable gains in diagnostic accuracy and stability offered by the CNN outweigh its computational demands. Although training required 417.22 s and prediction took 14.58 s, deployment on dedicated edge hardware (e.g., FPGAs or TPUs) could

significantly reduce inference time, providing a practical approach for real-time, reliable fault diagnosis in SEIG systems.

IV.5.2 Robustness Analysis of the CNN for Broken-Bars Fault

The CNN model was trained using a dataset corresponding to broken bar fault conditions. The healthy operating state was labeled as F0, while fault conditions were defined as follows: F1 represents one broken bar, F2 two broken bars, F3 three broken bars, F4 four broken bars, and F5 five broken bars. The model achieved a high classification accuracy of 99.95%, demonstrating its effectiveness in fault detection. The training and prediction times were 84.97 seconds and 1.46 seconds, respectively, indicating a satisfactory computational performance. Further detailed results are presented in Table IV.8.

Table IV-8 CNN performance on broken bar fault data

Class	Precision	Recall	F1_Score
F0	0.99720	1	0.99860
F1	1	0.99719	0.99859
F2	1	1	1
F3	1	1	1
F4	1	1	1
F5	1	1	1
Micro Average	0.99953	0.99953	0.99953

The model demonstrates exceptional classification capability across all classes. For the healthy state (F0), the precision, recall, and F1-score are 0.9972, 1.0, and 0.9986, respectively, indicating that almost all healthy samples were correctly identified with very few false positives. Similarly, for one broken bar (F1), the model achieves near-perfect performance with

a precision of 1.0, recall of 0.99719, and F1-score of 0.99859, showing reliable detection of early-stage faults.

For higher fault levels (F2–F5), all metrics reach 1.0, reflecting perfect classification of multiple broken bars. The micro-average values of 0.99953 for precision, recall, and F1-score further confirm that the model consistently performs at an extremely high level across all classes, demonstrating both high sensitivity and specificity.

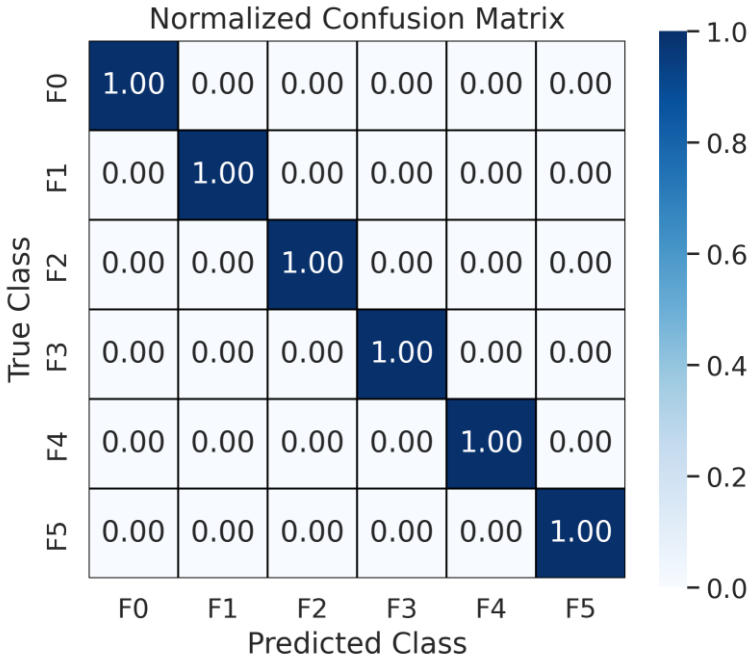

Figure IV.6 Confusion matrices of the CNN

The model achieves a perfect classification rate across all categories, from the healthy state (F0) to the various fault severities (F1–F5). The diagonal elements all reach a normalized value of 1.00, while the off-diagonal elements remain at 0.00, indicating that there are no misclassifications, false positives, or false negatives within the test set. This performance demonstrates the high sensitivity and specificity of the CNN architecture, confirming its ability to accurately distinguish between subtle differences in motor signatures. Ultimately, the results validate that the model has successfully learned the discriminative features necessary for reliable fault diagnosis, ensuring high precision in identifying the exact state of the rotor bars.

IV.6 conclusion

This chapter presents a comprehensive hybrid diagnostic framework that integrates high-resolution finite-element modeling, time–frequency signal analysis, and both ML and DL classifiers to improve the reliability of SEIGs in wind-energy microgrids. Time-stepping FEM effectively captured the electromagnetic dynamics of a 4.087 MW SEIG with unprecedented spatial and temporal resolution. The proposed approach successfully simulated multiple operating conditions, including healthy operation, unbalanced loads, open-phase faults, and progressive capacitor degradation.

By combining time-domain, spectral, and statistical features with ML classifiers, the framework demonstrated strong diagnostic capability. Additionally, a lightweight CNN trained on wavelet scalograms achieved exceptional performance, with an overall accuracy of 99.91 %, F1-scores exceeding 0.99, and AUC values above 0.98, surpassing RF, KNN, SVM, and NB classifiers by 2.85–13.12 %. These findings confirm that integrating physics-based modeling with data-driven intelligence provides a scalable and powerful solution for early fault detection, predictive maintenance, and long-term operational stability in isolated renewable-energy systems.

Building on these promising results, several future research directions are envisioned: (I) a hardware-in-the-loop (HIL) real-time implementation to validate the framework under realistic operating conditions, enabling online monitoring and rapid decision-making; (II) development of a hybrid FEM–ML digital twin that continuously updates the model with real sensor data, enhancing robustness against environmental variations; and (III) extension of the methodology to additional fault types, including bearing defects, rotor bar failures, eccentricity, and converter-related disturbances. Furthermore, lightweight, embedded-AI versions of the CNN will be optimized for edge deployment in wind-turbine controllers or microgrid energy-management systems, facilitating practical implementation of intelligent, predictive, and self-adaptive monitoring solutions for next-generation wind-energy microgrids.

V. General conclusion

This research addresses the growing significance of wind energy as a sustainable and renewable source of electricity, emphasizing the necessity of developing effective and reliable diagnostic strategies to ensure the safe and stable operation of WECS under diverse operating conditions. It also reviews the evolution of wind turbine designs and the technologies employed, highlighting the challenges associated with the reliability of SEIG, particularly the aging-related faults of excitation capacitors and their direct impact on the electrical performance of the system. In this context, the thesis proposes a comprehensive methodology for diagnosing aging faults in the excitation capacitors of SEIGs. The approach integrates precise electromagnetic modeling using the FEM with advanced signal processing techniques to extract discriminative features capable of representing the dynamic behavior of the system under both healthy and faulty operating conditions. These features are then leveraged within ML and DL frameworks to enhance the accuracy, robustness, and reliability of the diagnostic process. The effectiveness of the proposed methodology is validated through extensive numerical simulations using FEM. The results demonstrate a high capability to distinguish between different fault conditions, achieving significant improvements in accuracy, robustness, and reliability compared to conventional approaches. These findings contribute to enhancing the reliability of SEIG-based wind energy systems and support their deployment in isolated applications and decentralized renewable energy networks.

The thesis is structured into four main chapters, addressing the fundamental aspects of the study. Chapter I provides a comprehensive overview of WECS, with particular emphasis on wind turbine designs, employed technologies, and practical applications. Chapter II focuses on modeling the wind energy conversion chain, with special attention to the modeling of SEIGs in the *dq* reference frame, supported by the FEM to ensure detailed and accurate electromagnetic analysis. Chapter III is dedicated to the presentation and discussion of the results, encompassing numerical simulation outcomes under both healthy and faulty operating conditions, employing signal processing techniques such as the FFT for a more detailed analysis of current signal behavior under healthy and faulty conditions. Finally, Chapter IV addresses the diagnosis of aging faults in excitation capacitors and broken rotor bars, employing advanced signal processing techniques as well as machine learning (ML) and deep learning (DL), aiming to enhance diagnostic accuracy, robustness, and reliability.

VI. Annex 1

Machine parameters:

Rated Power	4.087 MW
Rated Voltage	3000 V
Coupling Method	Wye
Number of Poles	2
Rated Speed	3135 (rpm)
Operating Temperature	75(°)
Stator slots	54
Hs0 stator slot	4.5 mm
Hs2 stator slot	115mm
BS2 stator slot	18.2 mm
Rotor slots	52
Bs0 rotor slot	3.5 mm
Bs1 rotor slot	13 mm
Bs2 rotor slot	13 mm
Hs0 rotor slot	4.3 mm
Hs01 rotor slot	2.7 mm
Hs1 rotor slot	4.85 mm
Hs2 rotor slot	40.25mm
Hs1 stator slot	2.4 mm
Bs1 stator slot	21.16mm

Excitation capacitor parameters:

Capacitance	190 μF
Coupling method	Delta
Total voltage	3600 V

CNN parameters:

Number of hidden layers	3
Number of classes	6
Number of signal samples	5,001
Training epochs	50

RF parameters:

Number of trees	300
Number of splits per tree	20
Length N	126
Number of features	18
Hold-Out validation scheme	70/30

SVM parameters:

Kernel Scale γ	automatically determined
Constraint C	10
Number of features	18
Length N	126
Hold-Out validation scheme	70/30

KNN parameters:

Majority vote among K	3
Hold-Out validation scheme	70/30
Number of features	18
Length N	126

NB parameters:

Hold-Out validation scheme	70/30
Number of features	18
Length N	126

References

[1] A. Elkhatat and S. Al-Muhtaseb, "Climate change and energy security: a comparative analysis of the role of energy policies in advancing environmental sustainability," *Energies,* vol. 17, no. 13, p. 3179, 2024.

[2] F. Salboukh, Y. Mousavi, I. B. Kucukdemiral, A. Fekih, and U. Cali, "Reliability assessment and condition monitoring of wind energy conversion systems using Bayesian networks: recent advances and key insights," *IEEE Access,* 2025.

[3] E. Rausell, S. Arnaltes, J. L. Rodríguez, M. Lafoz, and G. Navarro, "Control of wind energy conversion systems with permanent magnet synchronous generator for isolated green hydrogen production," *International Journal of Hydrogen Energy,* vol. 107, pp. 241-251, 2025.

[4] S. Kundu, "Improved dynamic performance of SEIG-based wind energy systems for off-grid applications," *Electric Power Systems Research,* vol. 251, p. 112198, 2026.

[5] A. Dilmi, A. Bouzida, N. Yassa, B. Fares, R. Bouddou, and A. O. Salau, "Enhancing the reliability of self-excited induction generators used in wind energy microgrids through a hybrid FEM–CNN-based fault diagnosis framework," *Journal of Renewable and Sustainable Energy,* vol. 18, no. 1, 2026.

[6] D. Manna, S. K. Goswami, and S. Paul, "Assessment of the Impact of SEIG based DGs on the Stable Operation of Islanded Micro-Grid," *Journal of The Institution of Engineers (India): Series B,* vol. 103, no. 3, pp. 767-777, 2022.

[7] M. M. Ahmed, W. S. Hassanein, and M. A. Enany, "Proposing and evaluation of SC techniques for variable speed high-power operation of SEIG," *IEEE Access,* vol. 8, pp. 20666-20675, 2020.

[8] G. Singh and V. Singh, "SEIG-based transient-and steady-state analysis using dragon fly approach," *Soft Computing-A Fusion of Foundations, Methodologies & Applications,* vol. 27, no. 6, 2023.

[9] S. Dewangan and S. Vadhera, "Performance evaluation of multilevel inverter in variable speed SEIG-based wind energy system," *Arabian Journal for Science and Engineering,* vol. 47, no. 3, pp. 3311-3324, 2022.

[10] A. S. Özer, F. Sevilmiş, H. Karaca, and H. Arabacı, "Enhanced control method for voltage regulation of DSTATCOM based SEIG," *Energy Reports,* vol. 8, pp. 839-847, 2022.

[11] J. Dalei and K. B. Mohanty, "Fault classification in SEIG system using Hilbert-Huang transform and least square support vector machine," *International Journal of Electrical Power & Energy Systems,* vol. 76, pp. 11-22, 2016.

[12] M. Derbal and H. Toubakh, "Early fault diagnosis in exciting capacitors of self-excited induction generator for wind energy applications," in *2018 International conference on communications and electrical engineering (ICCEE)*, 2018: IEEE, pp. 1-5.

[13] M. Demirtas, H. Calgan, T. Amieur, and M. Sedraoui, "Small-signal modeling and robust multi-loop PID and H∞ controllers synthesis for a self-excited induction generator," *ISA transactions,* vol. 117, pp. 234-250, 2021.

[14] T. U. Badrudeen, F. K. Ariyo, and N. Nwulu, "Voltage stability improvement and power losses reduction through multiple grid contingency supports," *Energy Exploration & Exploitation,* vol. 42, no. 4, pp. 1218-1240, 2024.

[15] E. R. M. Shouman, "Global prediction of wind energy market strategy for electricity generation," in *Modeling, Simulation and Optimization of Wind Farms and Hybrid Systems*: Intechopen, 2020.

[16] M. Cristea, C. Cristea, R.-A. Tîrnovan, and F. M. Șerban, "Levelized cost of energy (LCOE) of different photovoltaic technologies," *Applied Sciences,* vol. 15, no. 12, p. 6710, 2025.

[17] A. S. Darwish and R. Al-Dabbagh, "Wind energy state of the art: present and future technology advancements," *Renewable Energy and Environmental Sustainability,* vol. 5, p. 7, 2020.

[18] L. Chang, H. B. Saydaliev, M. S. Meo, and M. Mohsin, "How renewable energy matter for environmental sustainability: Evidence from top-10 wind energy consumer countries of European Union," *Sustainable Energy, Grids and Networks,* vol. 31, p. 100716, 2022.

[19] Z. N. Ashrafi, M. Ghaderi, and A. Sedaghat, "Parametric study on off-design aerodynamic performance of a horizontal axis wind turbine blade and proposed pitch control," *Energy Conversion and Management,* vol. 93, pp. 349-356, 2015.

[20] R. Kumar, K. Raahemifar, and A. S. Fung, "A critical review of vertical axis wind turbines for urban applications," *Renewable and Sustainable Energy Reviews,* vol. 89, pp. 281-291, 2018.

[21] H. Hoghooghi, N. Chokani, and R. S. Abhari, "A novel optimised nacelle to alleviate wind turbine unsteady loads," *Journal of Wind Engineering and Industrial Aerodynamics,* vol. 219, p. 104817, 2021.

[22] E. Tzen, "Small wind turbines for on grid and off grid applications," in *IOP conference series: Earth and environmental science*, 2020, vol. 410, no. 1: IOP Publishing, p. 012047.

[23] L. M. Al-Hadhrami, "Performance evaluation of small wind turbines for off grid applications in Saudi Arabia," *Energy conversion and management,* vol. 81, pp. 19-29, 2014.

[24] K. Calautit, A. Aquino, J. K. Calautit, P. Nejat, F. Jomehzadeh, and B. R. Hughes, "A review of numerical modelling of multi-scale wind turbines and their environment," *Computation,* vol. 6, no. 1, p. 24, 2018.

[25] A. Benitez, C. Wulf, B. Steubing, and J. Geldermann, "Scenario-based LCA for assessing the future environmental impacts of wind offshore energy: An exemplary

analysis for a 9.5-MW wind turbine in Germany," *Energy, Sustainability and Society,* vol. 14, no. 1, p. 49, 2024.

[26] C. Hetyei and R. Nagy, "Review of Wind Turbine Failures, Highlighting Fire Accidents," *Műszaki Katonai Közlöny,* vol. 30, no. 2, pp. 43–56-43–56, 2020.

[27] Y. R. Konda *et al.*, "Thermal analysis and cooling strategies of high-efficiency three-phase squirrel-cage induction motors—A review," *Computation,* vol. 12, no. 1, p. 6, 2024.

[28] R. Choudhary and R. Saket, "A critical review on the self-excitation process and steady state analysis of an SEIG driven by wind turbine," *Renewable and Sustainable Energy Reviews,* vol. 47, pp. 344-353, 2015.

[29] S. Aoun, A. Boukadoum, and L. Yousfi, "Advanced power control of a variable speed wind turbine based on a doubly fed induction generator using field-oriented control with fuzzy and neural controllers," *International Journal of Dynamics and Control,* vol. 12, no. 7, pp. 2398-2411, 2024.

[30] M. Soomro *et al.*, "Performance improvement of grid-integrated doubly fed induction generator under asymmetrical and symmetrical faults," *Energies,* vol. 16, no. 8, p. 3350, 2023.

[31] M. I. Abdelkader, A. K. Abdelsalam, and A. A. Hossameldin, "Indirect vector-controlled brushless doubly-fed twin-stator induction generator for wind energy conversion application," *Energies,* vol. 13, no. 16, p. 4174, 2020.

[32] R. Gao, X. She, I. Husain, and A. Q. Huang, "Solid-state-transformer-interfaced permanent magnet wind turbine distributed generation system with power management functions," *IEEE Transactions on Industry Applications,* vol. 53, no. 4, pp. 3849-3861, 2017.

[33] H. Shi, Z. Zhang, J. Han, and J. Li, "Dynamic performance improvement of wound rotor synchronous starter/generator system based on PWM rectifier," *IEEE Transactions on Transportation Electrification,* vol. 9, no. 3, pp. 4639-4649, 2023.

[34] M. E. Abdallah, O. M. Arafa, A. Shaltot, and G. A. A. Aziz, "Wind turbine emulation using permanent magnet synchronous motor," *Journal of Electrical Systems and Information Technology,* vol. 5, no. 2, pp. 121-134, 2018.

[35] X. Zhao, W. Wang, S. Niu, and W. N. Fu, "Reconstructing saliency effect in 12/10 DC Vernier reluctance machine for position-sensorless drive aerospace starter generator application," *IEEE Transactions on Energy Conversion,* vol. 37, no. 3, pp. 2027-2036, 2022.

[36] H. Liu, Y. Wang, T. Zeng, H. Wang, S. C. Chan, and L. Ran, "Wind turbine generator failure analysis and fault diagnosis: A review," *IET Renewable Power Generation,* vol. 18, no. 15, pp. 3127-3148, 2024.

[37] A. Bouzida, "Diagnostic de défauts des machines asynchrones par la technique du traitement du signal," Alger, Ecole Nationale Polytechnique, 2015.

[38] H. Mao, K. Khorasani, and Y. Guo, "Analysis and Diagnosis of the Stator Turn-to-Turn Short-Circuit Faults in Wound-Rotor Synchronous Generators," *Energies,* vol. 18, no. 9, p. 2395, 2025.

[39] M. Hassanzadeh, J. Faiz, and A. Kiyoumarsi, "A new analytical technique for analysis and detection of air-gap eccentricity fault in surface-mounted permanent-magnet machines," *International Transactions on Electrical Energy Systems,* vol. 29, no. 3, p. e2764, 2019.

[40] Y. L. He *et al.*, "Stator current identification in generator among single and composite faults composed by static air-gap eccentricity and rotor inter-turn short circuit," *IET Electric Power Applications,* vol. 17, no. 2, pp. 268-278, 2023.

[41] I. D. P. Karyatanti, A. Noersena, F. R. Purnomo, R. S. Zulkifli, and A. Wijayanto, "Analysis of Outer Race Bearing Damage by Calculation of Sound Signal Frequency Based on the FFT Method," *International Journal of Engineering & Technology Innovation,* vol. 13, no. 1, 2023.

[42] H. Habibi, H. R. Nohooji, and I. Howard, "Adaptive PID control of wind turbines for power regulation with unknown control direction and actuator faults," *IEEE Access,* vol. 6, pp. 37464-37479, 2018.

[43] L. Varshney, A. S. S. Vardhan, A. S. S. Vardhan, S. Kumar, R. Saket, and P. Sanjeevikumar, "Performance characteristics and reliability assessment of self-excited induction generator for wind power generation," *IET Renewable Power Generation,* vol. 15, no. 9, pp. 1927-1942, 2021.

[44] A. Shaeboub, "The Monitoring of Induction Machines Using Electrical Signals from the Variable Speed Drive," University of Huddersfield, 2018.

[45] C.-C. Lin and C.-R. Chen, "Realization of high-efficiency and high-output characteristics of magnetic power generators using single-phase angle transformation and three-phase six-wire winding," *Microsystem Technologies,* vol. 28, no. 1, pp. 83-93, 2022.

[46] M. I. Mosaad, "Comparative study between the electrical generators used in wind energy conversion systems," *International Journal of Energy,* vol. 14, no. 1, pp. 88-92, 2020.

[47] H. H. Kadhum, A. S. Alkhafaji, and H. H. Emawi, "The influence of iron losses on selecting the minimum excitation capacitance for self-excited induction generator (SEIG) with wind turbine," *Indonesian Journal of Electrical Engineering and Computer Science,* vol. 19, no. 1, pp. 11-22, 2020.

[48] A. Dahbi, A. Reama, M. Hamouda, N. Naït-Saïd, and M.-S. Naït-Saïd, "Control and study of a real wind turbine," *Computers & Electrical Engineering,* vol. 80, p. 106492, 2019.

[49] B. Kelkoul and A. Boumediene, "Stability analysis and study between classical sliding mode control (SMC) and super twisting algorithm (STA) for doubly fed induction generator (DFIG) under wind turbine," *Energy,* vol. 214, p. 118871, 2021.

[50] H. Itouchene, F. Amrane, and Z. Boudries, "Robust control of DFIG wind turbines in sub/super-synchronous operation using integral backstepping controller," *Journal of Renewable Energies,* pp. 23-31, 2023.

[51] A. Mazari, K. Laroussi, A. Maafa, H. Ait Abbas, A. Kouzou, and B. Naceri, "Power Control of Cascaded Doubly Fed Induction Generator Integrated Into Wind Power Generation System Using Sliding Mode Control," in *2023 1st International Conference on Renewable Solutions for Ecosystems: Towards a Sustainable Energy Transition (ICRSEtoSET)*, 2023: IEEE, pp. 1-6.

[52] K. Noussi *et al.*, "Adaptive multi-objective sliding mode control of a wind energy conversion system involving doubly fed induction generator for power capture optimization," *Journal of Control, Automation and Electrical Systems,* vol. 32, no. 6, pp. 1663-1677, 2021.

[53] M. Z. Malik, M. H. Baloch, M. Gul, G. S. Kaloi, S. T. Chauhdary, and A. A. Memon, "A research on conventional and modern algorithms for maximum power extraction from wind energy conversion system: A review," *Environmental Science and Pollution Research,* vol. 28, no. 5, pp. 5020-5035, 2021.

[54] A. Mazari, K. Laroussi, O. Fergani, H. A. Abbas, and H. Rezk, "A Hybrid Whale Optimization—Cuckoo Search Algorithm for Maximum Power Point Tracking in PMSG-Based Wind Turbine Systems," *International Transactions on Electrical Energy Systems,* vol. 2025, no. 1, p. 7411272, 2025.

[55] R. Riyadh, "Contrôle des puissances générées par un système éolien à vitesse variable basé sur une machine asynchrone double alimentée," Université Mustapha Ben Boulaid Batna 2, Département de l'éléctrotechnique, 2017.

[56] M. B. Hemanth Kumar, B. Saravanan, P. Sanjeevikumar, and F. Blaabjerg, "Review on control techniques and methodologies for maximum power extraction from wind energy systems," *IET Renewable power generation,* vol. 12, no. 14, pp. 1609-1622, 2018.

[57] M. Hannachi, O. Elbeji, M. Benhamed, and L. Sbita, "Optimal tuning of proportional–integral controller using particle swarm optimization algorithm for control of permanent magnet synchronous generator based wind turbine with tip speed ratio for maximum power point tracking," *Wind Engineering,* vol. 45, no. 2, pp. 400-412, 2021.

[58] O. Zebraoui and M. Bouzi, "Comparative study of different MPPT methods for wind energy conversion system," in *IOP Conference Series: Earth and Environmental Science*, 2018, vol. 161, no. 1: IOP Publishing, p. 012023.

[59] Y. Baala and S. Bri, "Torque estimator using MPPT method for wind turbines," *International Journal of Electrical and Computer Engineering (IJECE),* vol. 10, no. 2, pp. 1208-1219, 2020.

[60] H. M. Kojabadi, L. Chang, and T. Boutot, "Development of a novel wind turbine simulator for wind energy conversion systems using an inverter-controlled induction motor," *IEEE Transactions on Energy conversion,* vol. 19, no. 3, pp. 547-552, 2004.

[61] Y. Luo and Y. Chen, "Fractional order [proportional derivative] controller for a class of fractional order systems," *Automatica,* vol. 45, no. 10, pp. 2446-2450, 2009.

[62] P. Kumar, J. B. Rawlings, and P. Carrette, "Modeling proportional–integral controllers in tracking and economic model predictive control," *Journal of Process Control,* vol. 122, pp. 1-12, 2023.

[63] F. Alyoussef and I. Kaya, "Proportional–integral and proportional–derivative controller design based on analytically computed centroid point for controlling integrating processes," *Proceedings of the Institution of Mechanical Engineers, Part I: Journal of Systems and Control Engineering,* vol. 237, no. 6, pp. 1045-1065, 2023.

[64] M. Gogoi, "Proportional-integral-derivative (PID) controller design for robust stability of arbitrary order plants with time-delay and additive uncertainty," Wichita State University, College of Engineering, Department of Electrical …, 2010.

[65] Y. V. Sambhavi and R. Vijayapriya, "Modified Field-Oriented Control Scheme for a 5-Level Knight Inverter in PMSM-Based Electric Vehicle Applications," *IEEE Access,* vol. 13, pp. 199846-199863, 2025.

[66] A. Qureshi, A. K. Giri, S. R. Arya, and S. Padmanaban, "Power conditioning using DSTATCOM in a single-phase SEIG-based isolated system," *Electrical Engineering,* vol. 104, no. 1, pp. 111-127, 2022.

[67] Z. Wang, L. Ding, X. Gao, G. Zhu, X. Wang, and V. Terzija, "Improved active current control scheme of wind energy conversion systems with PLL synchronization during grid faults," *IEEE Transactions on Sustainable Energy,* vol. 14, no. 1, pp. 717-729, 2022.

[68] M. R. Oliveira, L. T. Soares, and A. L. Coelho, "Back-to-Back Inverter for Induction Machine Drive with Harmonic Current Compensation and Reactive Power Tolerance to Voltage Sags," *Energies,* vol. 17, no. 16, p. 4110, 2024.

[69] P. Karlsson, *DC distributed power systems-Analysis, design and control for a renewable energy system*. Lund University, 2002.

[70] R. Teodorescu, M. Liserre, and P. Rodriguez, *Grid converters for photovoltaic and wind power systems*. John Wiley & Sons, 2011.

[71] A. Bouzida, R. Abdelli, O. Touhami, and A. Aibeche, "Dynamic eccentricity fault diagnosis in induction motors using finite element method and experimental tests," *International Journal of Industrial Electronics and Drives,* vol. 3, no. 4, pp. 199-209, 2017.

[72] F. Belynda, R. Abdelli, and A. Bouzida, "Stator current signal crossing for fault diagnosis of self-excited induction generators," *Acta Polytechnica,* vol. 63, no. 5, pp. 293-304, 2023.

[73] F. Belynda *et al.*, "A Novel Algorithm for Fault Diagnosis of Induction Generators in Wind Power Systems Utilizing Stator Current Signal Crossing and Finite Element Modeling," *Results in Engineering,* p. 107329, 2025.

[74] D. Ali, B. Ahcene, and N. Yassa, "Modeling of Wind Generation Systems with Self-Excited Induction Generators Using the Finite Element Method," *Algerian Journal of Renewable Energy and Sustainable Development,* vol. 7, no. 1, pp. 37-42, 2025.

[75] A. Dilmi, A. Bouzida, N. Yassa, and F. Belynda, "Assessment of capacitor bank configuration of self-Excitation in induction generators utilizing finite element analysis," *Brazilian Journal of Technology,* vol. 7, no. 4, pp. e76010-e76010, 2024.

[76] J. L. Bermudez and S. Nilsson, "Capacitors for LCC and VSC HVDC Converter Stations," in *High Voltage DC Transmission Systems: HVDC*: Springer, 2025, pp. 1-29.